Solid and Fluid Coupling in Discreet Element method

by

Yifei Cui

A thesis submitted in partial fulfillment of the requirements for the degree of

Doctor of Philosophy

in
Geotechnical Engineering

Department of Civil and Environmental Engineering
University of Alberta

Abstract

The Discrete Element Method (DEM) has been developed and used in modelling dry granular materials with or without cohesive bonding between particles. The incorporation of fluid flow in the DEM analysis is difficult since the DEM is a discrete approach to mechanistic analysis while fluid is a continuum. This research is focused on the development of numerical techniques and procedures that provide the coupling of the DEM with the continuum fluid. This thesis provides two coupling methods for (1) the coupling of solid permeability and fluid flow (SPF), and (2) the coupling between solid deformation and pore pressure (SDP) for undrained and semi drained conditions.

The SPF coupling accounts for the interaction of fluid flow in a porous medium with solid deformation and solid dislodgement by the flow forces imposed by the pressure gradient and drag forces on solid particles. Deformation of the porous medium alters the pore sizes, hence, changes the permeability of the material. Further, the production of the solid grains alters the porosity and the solid boundaries from which the fluid is produced.

The SDP coupling refers to the generation of pore water pressure as a result of solid deformation in the porous medium. The variation of pore sizes results in a temporary increase in pore fluid pressure, which gives rise to the pressure gradient causing pore water diffusion. The dissipation of pore pressure can be analyzed using the SPF approach but the generation of excess pore pressure requires the coupled analysis of the fluid and solid deformation. Any decrease in void space results in excess pore pressure that reduces the effective stresses, hence, changes the amount of deformation. Therefore, the SDP is considered to be a two-way coupling technique.

The motivation of this work arises from the desire to analyze sand production in oil wells during the oil recovery from sandstone formations. Sanding is the production of formation sand driven by

the de-cementation of the formation sand around the borehole and the flow of reservoir fluids during the oil recovery process. Problems associated with sand production include the erosion of pipelines and surface facilities, wellbore intervention costs and complexities, and environmental impacts. Large amounts of sand production in a short period may clog up the well, damage the well equipment, and destabilize the well due to the loss of materials. On the other hand, a controllable amount of sand production may increase the wellbore productivity and reduce the wellbore completion cost. Therefore, understanding the sand production mechanisms and the ability to predict and manage the rate of sand production at the field scale are beneficial.

This thesis presents a model for the investigation of sandstone degradation and sand production mechanisms by using the SPF coupling method. The model was used to investigate the effects of in-situ stresses and flow rate on sand production. A linked DEM-fluid flow model for sanding analysis is developed. The model calculates seepage forces and applies them to solid particles in the DEM model. The model accounts for permeability and porosity changes due to sandstone deformation and sand production. The DEM model is verified against poro-elastoplastic analytical solutions. Subsequently, the model is used for sanding simulation from a block-shaped sample under different far-field stress and pressure conditions. The boundary stresses and fluid pressures are varied to study their influence on sandstone degradation and sand production.

Another important factor in sand production is the generation of excess pore pressure in the reservoir during the drilling as well as during the production due to the deformation of the porous medium. Excess pore pressure can lead to the loss of shear strength and particles contacts resulting in plastic deformations.

The methodology this thesis presents for the incorporation of excess pore pressure in the DEM simulation (SDP) with a new liquid particle element is novel. The liquid particle element has a

specific stiffness that enables the calculation of excess pore pressure build up or the dissipation due to pore space deformation. Analytical solutions of conventional soil mechanics problems, such as isotropic compression and consolidated triaxial undrained test, have been used to verify the proposed algorithm quantitatively under undrained condition. The oedometer test and consolidation theory are then used to quantitatively validate and verify the dissipation model.

The SPF and SDP models are then applied to simulate consolidated-undrained triaxial tests at different levels of porosity and pore pressure. The numerical results show good agreement between the proposed scheme and the laboratory results. The proposed scheme provides an effective method to calculate pore pressure in a porous medium by using the discrete element approach.

Acknowledgement

I would like to express my heartfelt gratitude to my supervisors, Dr. Dave Chan and Dr. Alireza Nouri. Their scientific literacy, constructive criticisms, and continuous encouragement created the ideal environment for me to learn and contribute to the creation of knowledge.

I wish to extend my gratitude to Dr. Derek Martin, Dr. Dave C. Sego, Dr. Ward Wilson, Dr. Rick Chalaturnyk, Dr. Lijun Deng, Dr. Samer Adeeb, Dr. Ben Jar and my other course instructors at the University of Alberta, for sharing their expertise and knowledge and contributed to my development as a researcher.

I also wish to thank Prof. Richard Wan, Department of Civil Engineering, University of Calgary for his constructive comments on my thesis.

I also extend my gratitude to my peers in Dr. Nouri's research group, particularly Ehsan Rahmati, Hossein Rahmati and Morteza Roostaei for sharing their ideas and assisting me with the coding.

Thank you to the graduate students in the geotechnical group and petroleum group in the Department of Civil and Environmental Engineering, University of Alberta, who engaged with me in scientific discussions and provided me with their insights when I was challenged with scientific difficulties during my research.

Finally, I thank my parents and my wife Yamei Li for their steadfast love and support.

Table of Contents

List of Tables

List of Figures

Nomenclature

SPF Coupling nomenclature

C	Cohesion of rock
C_f	Compressibility of Fluid
E_p	Particle Young's modulus
E_{pb}	Parallel bond Yong's modulus
h	Sample Thickness
k	Permeability of rock
k_c	Permeability of the rock in the plastic zone
k_e	Permeability of the rock in the elastic zone
K_n	Normal stiffness of the particle
K_s	Shear stiffness of the particle
$(K_s/K_N)_p$	Particle normal to shear stiffness ratio
$(K_s/K_N)_{pb}$	Parallel bond normal to shear stiffness ratio
m	mass of the particle
P_0	Outer boundary pore pressure
P_i	Inner boundary pore pressure
q	Fluid flow rate
R_i	Radius of inner wellbore
R_0	Radius of whole model
R_c	Radius of plastic zone
R_p	Particle radius

$S_{N\,pb}$	Parallel bond normal strength
$S_{S\,pb}$	Parallel bond shear strength
T	Porosity of the fully sanded block
t	DEM time step
v_r	Fluid velocities in the radial direction
v_θ	Fluid velocities in the tangential direction
v_z	Fluid velocities in the tangential direction
ε_v	Volumetric strain
Λ	Degree of bonding
μ	Fluid Viscosity
μ_p	Partial friction coefficient
ρ_p	Particle density
ϕ	Porosity of rock
$\boldsymbol{\phi}$	Friction angle of sample
ϕ_1	porosity measured from measurement sphere at the end of the iteration
ϕ_{full}	porosity measured from the measurement sphere before the onset of sanding from the block

SDP Coupling nomenclature

B	B value
C_f	Compressibility of pore fluid
C_s	Compressibility of soil skeleton
C_v	Coefficient of consolidation
C_w	Compressibility of water

d	Drainage path
D_i^n	The intersection at a contact in the x, y, and z component
D_{total}^n	Total intersection at a contact
e	Void ratio
E_s	Young's modulus of solid particle
E_w	Virtual Young's modulus of water particle
F_i^{cn}	Normal component of contact force
F_i^{cs}	Shear component of contact force
$F_j^{(c,p)}$	the force acting on that particle (p) at contact (c)
F_{w0}	The force on a contact between two particles calculated from the water particle stiffness before the pore pressure reduction
F_{w1}	The force on a contact between two particles calculated from the water particle stiffness after the pore pressure reduction
g	Gravity
H	Thickness of the drainage layer
k	Permeability in soil
K_T	Combined stiffness include solid and water particle stiffness
K_w	Stiffness of water element
$K_{w(c)}$	The combined normal stiffness of fluid particles in the linear contact model
K_{w0}	Water particle stiffness before the pore pressure reduction
K_{w1}	Water particle stiffness after the pore pressure reduction
K_s	Stiffness of solid element
K_{b-b}	Combined stiffness between particle-particle contact
K_{b-wall}	Combined stiffness between particle-wall contact

m_v	Coefficient of volume compressibility of soil skeleton
n	Porosity of sample
N	Number of particles in the sample (Loose packing case)
N_p	Number of particles in the control volume (Irregular packing case)
$N_c^{(p)}$	Number of contact around each particle (p)
p_0	Pore pressure in the sample before dissipation (loose packing case)
p_1	Pore pressure in the sample after dissipation occurs (loose packing case)
r	Radius of particle
R^A	Radius of ball A at a contact
R^B	Radius of ball B at a contact
R_m	Radius of particle m
T_v	Time factor
u_0	The initial pore pressure of the whole sample
u_1	The pore pressure at the current stage during pore pressure dissipation
$\bar{u}$	Average pore pressure in whole sample
$\overline{u_{(m)}}$	Average pore pressure on particle m
$u_{(m)i}$	Pore pressure on particle m in i direction
$\bar{U}$	Average degree of consolidation
V	Sample's total volume
V_b^T	Volume of total particles in a control volume
V_{b-b}	Volume of total particle-particle intersection
V_{b-w}	Volume of total particle-wall intersection

V_v	Volume of pore space
V_s	Volume of solid
$V^{(p)}$	Volume of particle (p)
$x_i^{(c)}$	The location of the contact around the particle (p)
$x_i^{(p)}$	The location of the particle centroid
Z	Distance to open drainage
α	Pore pressure reduction factor of whole sample
β_m	Pore pressure dissipation factor of particle m
γ	Adjusting parameter for different contact type
γ_w	Unit weight of water
Δ_0	particle – particle intersection before the pore pressure reduction
Δ_1	particle – particle intersection after the pore pressure reduction
ΔH_f	Final 1D consolidation settlement of the whole soil layer
ΔS_{b-b}	Intersection between two particles
ΔS_{b-w}	Intersection between a particle and a wall
ΔU	Excess pore pressure build up
μ	Particle Friction Coefficient
$\bar{\sigma}_{ij}$	average stress in a volume V
$\bar{\sigma}_{ij}^{(p)}$	average stresses in particle (p)
$\overline{\sigma'_{ii}}$	Average effective stress of sample in ii direction
$\sigma'_{(m)ii}$	Effective stress on particle m in ii direction
σ'_{dev}	Effective deviatoric stress of sample in triaxial undrained test
σ'_r	Effective confining stress of sample in triaxial undrained test

Abbreviations

1D	One Dimensional
2D	Two Dimensional
3D	Three Dimensional
CFD	Computational Fluid Dynamics
DEM	Discrete Element Method
FEM	Finite Element Method
HC	Hollow Cylinder
LBM	Lattice Boltzmann Method
LBM-DEM	Lattice-Boltzmann Discrete Element Method
LBT	Large Block Test
PFC	Particle Flow Code
PSD	Particle Size Distribution
PT	Phase Transformation
SDP	Solid Deformation Pore Pressure
SEM	Scanning Electron Microscope
SPF	Solid Permeability Flow
UCS	Uniaxial Compressive Strength

Chapter 1. Introduction

1.1. Introduction and Background

The interaction between the fluid and solid phase occurs in a wide range of engineering problems relevant to granular media (Zhao and Shan, 2013), which include petroleum, geotechnical, mechanical, and chemical engineering (Tipthavonnukul, 2002).

Conventional approaches based on continuum theories of porous media have considered the interaction between pore fluids and solid particles in a phenomenological manner. However, such approach cannot provide a quantitative understanding of microscale phenomena related to the behavior of particles (Zhu et al., 2008). Without this information, it is difficult to establish a general method for reliable design and control of particulate processes of different types. The Discrete Element Method (DEM), which was introduced by Cundall (1971), became a successful model in analyzing the microscopic interaction of particles. DEM is a Lagrangian approach, and solid particle behavior is computed based on the Newton's Second Law of Motion. The contact force acting on a solid particle is calculated using a spring-dashpot system (Sakai, 2016).

In order to obtain a better understanding of the disaggregation of particles from the soil and rock mass and its transport under the effect of fluid flow, modelling fluid phase and fluid and solid particle interaction is necessary. A conventional fluid flow DEM coupling method solves Darcy's law or the Navier-Stokes equation for fluid flow using Computational Fluid Dynamics (CFD) (O'Sullivan, 2011). One difficulty with above approaches is that the solutions of the mass balance and the three momentum equations for fluid flow are computationally demanding. Besides, there is a few research works focused on the excess pore water pressure buildup using DEM coupled with the fluid flow since it is difficult to determine pore space connectivity and pore space

deformation in a discontinuum. The pore pressure changes due to solid deformation is a fluid-solid deformation problem which is more complex than the solid-fluid flow problem.

The incorporation of fluid in DEM analysis is difficult since DEM is a discrete approach to mechanistic analysis and fluid is a continuum. This research is focused on the development of a numerical technique that provides the coupling of DEM with continuum fluid and the application in sand production.

1.2. Problem Statement

The motivation of this work arises from the desire to analyze sand production in oil wells during the oil recovery from sandstone formations. Sand production is the erosion of formation sand due to the flow of reservoir fluid during oil recovery from oil sandstone reservoirs (Fjær, 2008). After drilling a wellbore, sandstone is often left unsupported next to the borehole opening. These are the locations where sand grains can be dislodged and entered into the oil recovery system. The weakened sandstone may then be eroded away by the flowing fluid. This leads to negative effects on well productivity and damage to the equipment installed in the oil wells with significant cost implications (Cheung, 2010). On the other hand, a controllable amount of sand production may increase the wellbore productivity due to increasing the permeability of the rock and reduce the oil production cost (Nouri et al., 2006). Therefore, understanding the sand production mechanisms and the ability to calculate and manage the rate of sand production at the field scale are beneficial.

While both experimental and analytical models of the sand production problem play an important role in finding a solution for the sand production problem, numerical modeling is essential for realistic predictions and understanding of the sanding mechanism (Rahmati, 2013). This can be done by incorporating the physics of fluid and solid interactions at the micro scale to obtain a better

understanding of the disaggregation of particles from the rock mass and its transport under the effect of fluid flow.

Another important factor in sand production is the generation of excess pore pressure in the reservoir during drilling as well as during oil production due to the deformation of the porous medium. Excess pore pressure can lead to the loss of shear strength and particles contacts resulting in plastic deformations.

The thesis is focused on the development of the methodology of DEM coupled with fluid flow and the application of fluid flow-solid coupling analysis on sand production problem. Two coupling methods have been developed in this thesis: solid permeability fluid coupling (SPF) and solid deformation pore pressure coupling (SDP).

SPF coupling refers to the interaction of fluid flow in a porous media on solid particle movement and deformation. The flow of fluid in a porous medium imposes pressure gradient and drag forces on solid particles. Particle movement and deformation of the porous medium changes the pore sizes which changes the permeability of the material. This has an effect of fluid flow. Therefore, it is a two-way coupling of solid-fluid interaction.

SDP coupling refers to the generation of pore water pressure as a result of solid deformation of a porous medium. The decrease, or increase, in pore sizes, results in a temporary increase in pore water pressure which gives rise to pressure gradient causing pore water diffusion. The dissipation of pore pressure can be analyzed using the SPF approach, but the generation or pore water pressure requires coupling analysis of the solid and fluid deformation. Decrease in void space results in an increase in pore water pressure that reduces effective stresses between solid grains, which in turn changes the amount of deformation. Therefore, SDP is a two-way coupling process.

1.3. Objective and Scope of work

The objectives of the research can be summarized as follows:

(1) Develop DEM-fluid flow model using SPF coupling method, by considering rock permeability and porosity change due to breakout and sand production.

(2) Apply SPF coupling method in sand production; obtain the erosion shape and calculate the rate of sand production, estimate the produced sand amount in relation to a fluid flow condition, reservoir pressure depletion, and different far field stress.

(3) Introduce a DEM SDP coupling method that is able to calculate pore pressure increase under the undrained condition and pore pressure dissipation due to rock deformation.

(4) Develop the DEM SDP coupling model with pore pressure calculation to estimate deformation of rock sample under pore fluid pressure dissipation condition.

(5) Application of SDP and SPF in consolidated-undrained triaxial tests at different levels of porosity and pore pressure.

1.4. Outline of Thesis

This thesis is subdivided into six chapters. A short description of the contents of each chapter is given as below.

Chapter 1 introduces the background of DEM coupled with fluid flow, sand production, research objectives and outlines of the thesis.

Chapter 2 gives a literature review of DEM fluid – solid coupling techniques, and discussion on the advantage and disadvantage of each model.

Chapter 3 provides the detailed development of solid permeability flow coupling, which includes developing the change in permeability as a result of solid deformation related to the change in porosity and development of fractures. Then, the numerical implementation of SPF with verification examples are conducted.

Chapter 4 describes the solid deformation coupling method, which includes the analytical development of water element and calculation of pore pressure from DEM phase in pore pressure build-up phase, and the water particle stiffness calculation in dissipation process. The numerical method is then verified with basic soil mechanics examples.

Chapter 5 describes of SDP and SPF integration process and the application in laboratory consolidated triaxial undrained test.

Chapter 6 presents the conclusion from the conducted research and recommendations for future research on the method of solid-fluid coupling.

Chapter 2. Literature review

This chapter provides a review of the current literature on fluid flow and DEM coupling to identify the gap in the existing knowledge in this respect. The review is then used in defining the objectives and designing the methodologies in this research.

2.1. Categories of solid-fluid coupling analysis

Several research works have been reflected in the literature in the coupling of the Discrete Element Method with other aspects of mechanics, such as solid, fluid, thermal and structural mechanics. Several coupling approaches in previous research efforts are reviewed here.

Tsuji et al. (1993) developed a solid-fluid coupling scheme to simulate fluidized beds. The drag force caused by the fluid is solved by the continuity equation for the fluid. The drag force is then calculated in each cell and applied to each discrete particle. The position and velocity of the particles are then calculated by DEM calculation for next step of the iteration.

Chan (1993) described the method of coupling fluid flow computation in discrete element model and applied in wet granular deformation simulation. The drag and buoyancy force were considered in the simulation of fluid – particle interactions. The permeability was updated and applied during the calculation process to present the particle effect on the fluid flow calculation. The same DEM fluid flow coupling method is also conducted by Sun and Vinogradov (1998) to study the flow jam of solid particles transported by fluid in planar channels.

Thallak et al. (1990) simulated the hydraulic fracture problem in a granular assemblage. A geometrically-coupled channel network was created by assigning nodes to pores and flow channels to the pore throats. The steady-state flow rate in channels was assumed to be linearly related to the pressure gradient based on the Hagen-Poiseuille equation. The buildup of pressure in pores is

calculated and applied to each particle. The proposed method was used in the simulation of hydraulic fracture in granular assembly with reasonable success.

It should be noted that the coupling mechanism is the major differences among various methodologies. Cundall (1999) classified the coupling mechanics based on fluid-particle interactions. In this thesis, a new category of coupling mechanics – solid deformation and fluid coupling is proposed by extending Cundall's classification. The categories, shown in Figure 2.1, are based on solid density and interacting effects between solid and fluid and described below:

- *Hydrostatic pressure and fluid buoyance*

When a particle is simply submerged in a non-flowing fluid under gravity, the only force that the fluid effects on the particle is due to the hydrostatic pressure difference between the top and bottom of the particle, which is also known as buoyant force. The buoyancy on a particle is simply equal to the weight of the fluid displaced by that particle.

- *Low concentration of particle in a flowing fluid*

If the particles move independently of each other, and they only occupy a small fraction of the fluid volume, viscous forces, which are a function of the relative speed of fluid and particle, are applied on each particle due to the flowing fluid. There are few particle-to-particle contacts; hence, the interaction among them is usually ignored. With a low concentration of solids, the effect of the solid on the flowing fluid is neglected.

- *High solid concentration in flowing fluid*

At high solid concentration, not only the flowing fluid will exert a drag force on the particles, the particles have an effect on the flow impedance. The effect of the fluid flow on the solid can be calculated using the Navier-Stokes equations for the solid-fluid mixture. If solid movement is

relatively small and the fluid flow is laminar, Darcy's Law is valid. In this case, there is a small fluid pressure gradient between the upstream and downstream of a particle and continuum flow calculation based on porosities and permeability can be used. Drag forces on the particles can be calculated from pressure gradient. Particle-to-particle interactions are calculated using the discrete element approach. In the implementation of particle-fluid interaction, permeability can be calculated from the discrete element code, and it will be used in fluid flow calculation using the continuum approach. This coupled approach is able to capture sand production mechanisms such as surface erosion and internal fines migration.

- *Solid deformations and fluid coupling*

When soil or rock is fully saturated with a fluid, if we assume the compressibility of water is much higher than the soil skeleton, not the soil solids, isotropic compression or sudden increase of axial pressure will cause void space to decrease resulting in an increase in the excess pore pressure. An example is the consolidation problem in soils with pore water diffusion. Another example is the liquefaction problem in sands during earthquakes which result in large displacements in soil. In this case, the increase in excess pore pressure will cause displacement and deformation of the soil resulting in changes in void space that are occupied by the fluid. This leads to solid-fluid deformation and causes fluid flow.
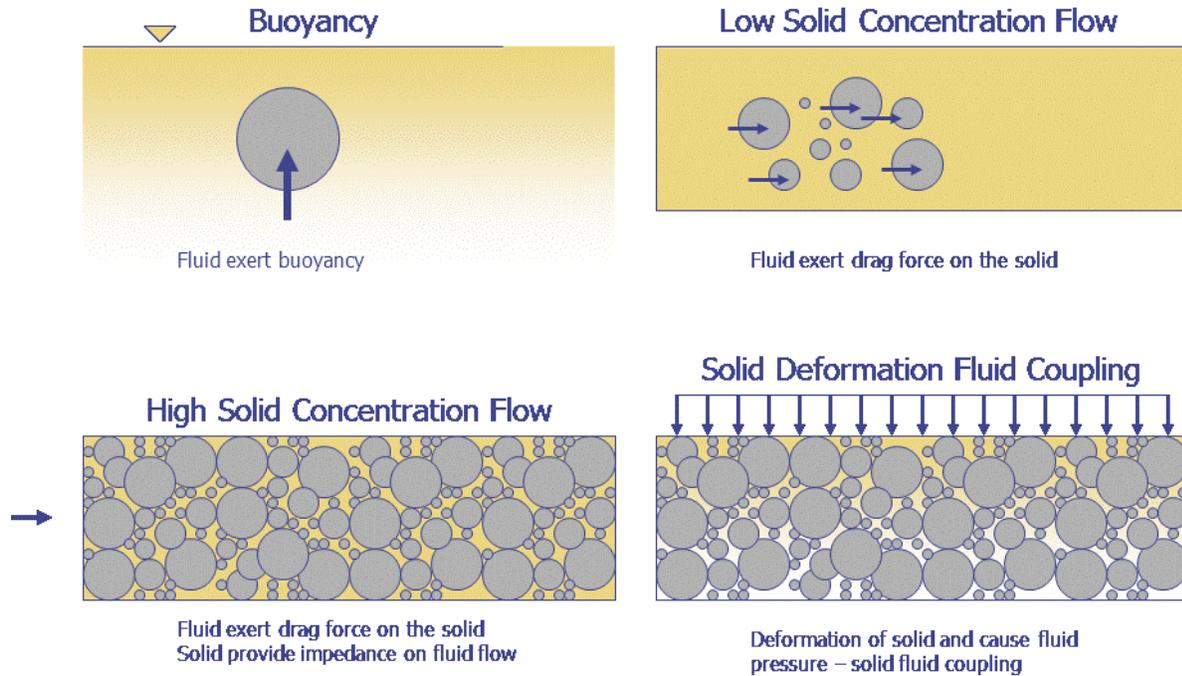
Figure 2.1: Categories of solid-fluid coupling analysis

2.2. Fluid-Solid Interactions

The coupling mechanisms explained here is in terms of fluid-particle interactions, which can be separated into the effect of fluid on the granular particle and the effect of the particle on the fluid. While a particle is submerged in a flowing fluid, drag, lift, and buoyant force are the basic effects that fluid has on the granular particles. At the same time, the presence of the particles will affect the fluid flow. The particle reduces the flow domain and imposes impedance to the flowing fluid (Tipthavonnukul, 2002).

2.2.1 Effects of fluid on the granular particles

2.2.1.1 Buoyancy

When a particle is submerged in a fluid, it experiences fluid pressure all around. The horizontal components of the fluid pressure cancel each other on both sides. However, there are two vertical components of the fluid pressure acting on the submerged particle: one is a downward component

9

of the total pressure on the upper surface of the object; the other is the upward component acting on the lower surface of the object. The bottom pressure is larger than the top one because of hydraulic gradient. The difference of the pressures results in an upward force acting on the object. Such force is independent of the depth of submergence and is defined as buoyant force B_i with respect to a submerged particle n (Tipthavonnukul, 2002):

$$B_n = (\rho_f - \rho_n)gV_n \qquad [2.1]$$

where ρ_f and ρ_n are the density of fluid and solid particle n respectively, g is the gravitational constant, and V_n is the volume occupied by solid n submerged totally in a fluid.

2.2.1.2 Drag Force and Seepage Force

When there is relative movement between fluid and particle, the drag force caused by the fluid on the particle will be acting on the surface of the particle in the direction of the relative movement. Suppose the submerged particle is moving in the same direction as the fluid. When the speed of the fluid is higher than particle, the drag force will push particle forward; when the speed of fluid is equal to that of the particle, the particle is not moving relative to the fluid; when the speed of fluid is smaller than the particle, the drag force will drag the particle backward. The total drag force is divided into two components: the skin-friction induced drag and pressure induced drag. The skin friction induced drag results from the shear stress of fluid layers adjacent to the particle surface perpendicular to the movement direction. The pressure induced drag is due to the pressure difference between the lower pressure at the rear of the particle and higher pressure at the front due to the disturbance of the flow stream along the movement direction. Drag force D_i of a specific granular particle n is evaluated by the following equation (Evett and Liu, 1987):

$$D_n = C_D \rho_f \frac{v_n - u}{2} A \qquad\qquad [2.2]$$

where C_D is the drag coefficient, v_n is the velocity of the granular particle n, and u is the velocity of fluid, and A is the projected area of the granular particle on a plane perpendicular to the flow direction. The drag coefficient is dependent on the particle's shape and Reynold's number.

For a fluid flow through a saturated assembly consisting of bounded particles, the velocity of each particle is considered to be zero. The seepage force F_{seep} is dominated only by the pressure difference between front and rear of particle and is calculated by:

$$F_{seep} = (P_f - P_b)A\alpha \qquad\qquad [2.3]$$

where P_f and P_b is the fluid pressure at front and rear of particle along fluid flow direction, A is the cross-sectional area of particle projected to the plane which is perpendicular to velocity of fluid flow, and α is a correction parameter related to size and shape of particles between 2 dimensional and 3 dimensional problems.

2.2.1.3 Pore Pressure Induced Force

When a saturated assembly consisting of loosely connected particles experience isotropic compression, the increase of pore pressure will have an effect on particles. It is difficult to determine the direction of the forces and the magnitude of the force on each particle because the particles are completely surrounded by the fluid. At the laboratory scale, it can be simply referred to as a consolidated-undrained or partially drained test.

Goodarzi et al. (2014) proposed a numerical scheme for fluid-particle coupled discrete element method based on poroelasticity by consideration of pore pressure generation. In the proposition of

Darcian regime, the fluid is assumed as a continuum phase on a Eulerian mesh. The pore pressure change ΔP is calculated from volumetric strain ε_v:

$$\Delta P = \varepsilon_v \frac{K_{eff}}{n}$$

$$K_{eff} = \frac{K_f}{n}$$

[2.4]

Where K_{eff} is the effective bulk modulus of the mixture, K_f is the bulk modulus of fluid, n is the porosity. The continuity equation of the fluid mesh for a compressible fluid is then solved using the finite difference method. By knowing the pore pressure on the node, the hydrodynamic force is the applied on each of the particle in fluid cell by using Equation 2.2.

Instead of using fluid grid, Liu et al. (2015) use measurement sphere, contains several particles, to calculate pore pressure buildup, the pore pressure induced force F_{Am} is calculated as:

$$F_{Am} = \Delta P(\pi r_i^2) n_{Am}$$

$$\Delta P = \varepsilon_v E_w$$

[2.5]

where ΔP is the increment of pore pressure, ε_v is the volumetric strain in measurement sphere A, E_w is the bulk modulus of fluid, r_m is the radius of particle m, and n_{Am} is a normal unit vector from center of measurement sphere A to center of particle m.

2.2.2 Effects of Granular Particle on the Fluid

The locations of particles can be calculated in discrete element modeling. The presence of the particles in the flow domain is considered as occupying the flow space that would have been otherwise available for fluid flow.

In the case of large pressure gradient and large deformation of the solid phase, the reduction in the flow channel leads to changes in flow velocity and fluid pressure. At the location of the granular particles, the fluid flow velocity will be less than that if the particles were not present. A reduction factor was applied to the calculation of Navier-Stokes equations in fluid flow recalculation (Tipthavonnukul, 2002). For the case of a fluid flow through a porous medium saturated with fluid, the reduction in flow channel leads to changes in the porosity and permeability of the particle assembly leading to a further change in fluid pressure.

For a saturated assembly of particles experiencing isotropic compression case, a decrease of pore space causes an increase in pore pressure, generating a reaction fluid force on the solid particles. The change in positions of the solid will change the pore space volume thus changing the pore pressure again.

2.3 Experimental observations of borehole breakouts and solid-fluid interaction

Rock failure is often observed to form localized failure zones of certain shapes around boreholes and perforation cavities. In general, fractures and breakouts form at the damaged perimeter of boreholes, and they are classically aligned with the direction of the local minimum principal stress. Borehole breakout has been used to predict the direction and magnitude of in situ stresses. There are three common types of breakouts that have been observed in hollow cylinder experiments in sandstone: (a) uniform failure; (b) dog-ear (V-shaped) breakouts; and (c) slit-like breakouts.

13

Similarly, four distinct failure patterns have been observed in perforation tests, which are (a) symmetric breakouts; (b) triple breakouts; (c) slit-like breakouts; and (d) high porosity wormholes.

The wellbore failure zone may be in the form of shear or tensile fractures (splitting and spalling). The failure mode and the extent of plastic damage around the cavity before localized failure depend on stress state, pore fluid properties and rock properties such as stiffness, yield strength, and porosity, among others. The propagation of this plastic zone governs the failure shape and growth. The initiation, growth, and stabilization of these morphologies and the parameters that affect the growth are of crucial importance in the analysis of wellbore stability and sand production.

Fluid flow has also been observed to influence the size and mode of failure in wellbore breakout and sand production. Fluid flow can remove disaggregated materials and, therefore, lead to the growth of the disaggregated zone.

2.3.1 Breakout studies

Over the years, a large number of physical model studies have been conducted to study breakouts. These are normally large block tests (LBT) or hollow cylinder (HC) tests with a central hole that simulates the wellbore. Other tests have simulated a single perforation in a full-scale physical model test. LBT and HC tests have been conducted on vertical holes (Behrmann et al. 1997). With some of these, the borehole was cased and perforated by a true downhole perforating gun (Behrmann et al. 1997), while with others, it was an open hole with or without a screen liner (Tronvoll et al. 1997). The single-perforation tests were conducted on unconsolidated sand samples (Bianco and Halleck 2001) and poorly consolidated sandstones (Tronvoll and Fjær 1994; Tronvoll et al. 1997).

The very first attempt to study breakout formations in scaled borehole tests using physical model testing was by Haimson and Song (1993), and several attempts have followed since (Lee and Haimson 1993, 1995; Haimson and Lee 2004; Haimson, 2007). In these works, they used cubic granite or sandstone specimens under different far-field stress conditions and established a linear correlation between the length and angular opening of the breakout with the far-field stresses. Their experiments showed different breakout shapes in different types of rocks. However, they observed consistent failure patterns at different loading stages for the same rock type. In their experiments, they loaded the sample to a specific loading level and then drilled the borehole into the sample under far-field stress states. They elevated the far-field state of stress for other tests on the same rock type to study the effect of far-field stress on breakout geometry. They observed that the length and span of the breakout were related to the far-field state of stress. Figure 2.2 illustrates the outcome of similar work by Lee (2005). The figure shows the breakout geometry observed in different sandstones from laboratory test. The only factor that was affecting the growth of the breakout was the increment in the far-field state of stress.
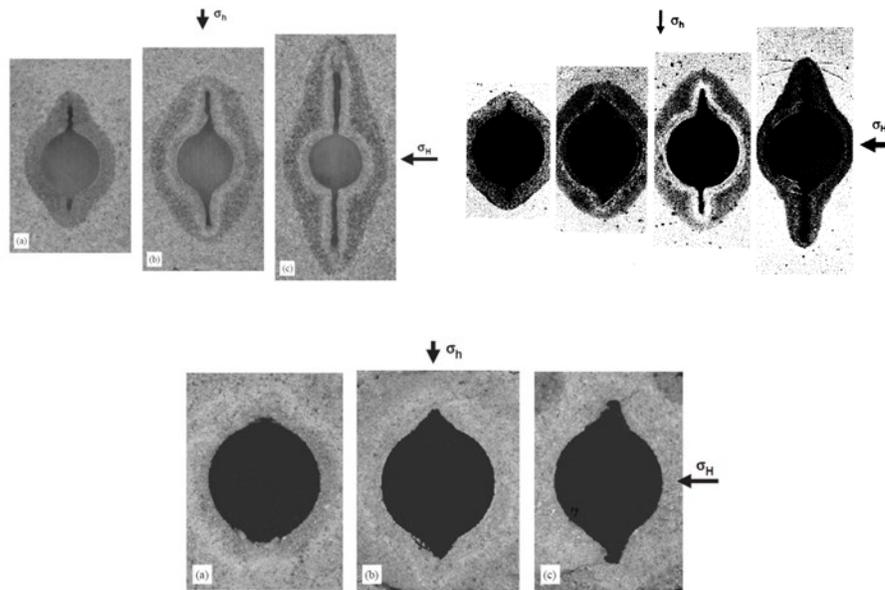
Figure 2.2: Breakout around different outcrop sandstone (After Lee 2005)

2.3.2 Rock disaggregation mechanisms

In the geomechanical context, rock failure mechanisms are listed as tensile failure, shear failure and compactive failure, also known as pore collapse. Tensile failure around a borehole occurs when one of the effective stresses is equal to the tensile strength of the formation rock. This mechanism is sometimes related to seepage forces which are proportional to pressure gradients (Bratli and Risnes 1981).

Shear failure may occur when some planes in the vicinity of the wellbore are subjected to higher shear stress than they can sustain (Figure 2.3). This mechanism is dominant in cemented sands and may lead to buckling when combined with tensile cracks (Coates and Denoo 1981; Edwards et al. 1983).
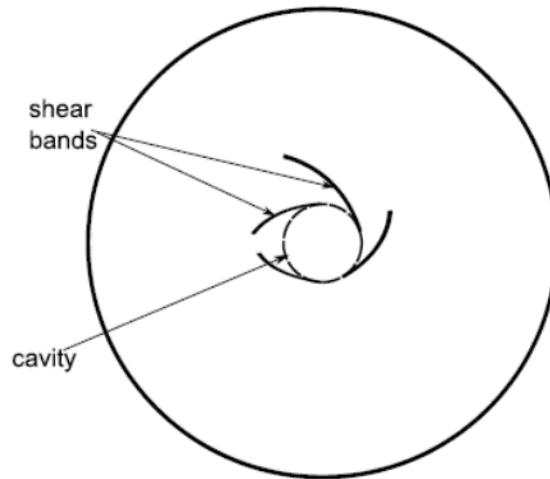
Figure 2.3: Shear bands around a hole

With the depletion of the reservoir pressure, effective stresses acting on the formation rock increase. At a certain stress level, pore collapse may occur in narrow zones called compaction bands and form a borehole breakout. As a result, it is necessary to consider the compressive mode of failure by using a cap in the constitutive law. Detournay (2008) showed that using a constitutive model enhanced with a yield cap enables the qualitative reproduction of breakouts that result from pore collapse. This is called a fracture-like or slit-type breakout, which has been observed in laboratory tests and has been related to compactive failure. The failure mechanism can be a combination of shear, tensile and compactive modes resulting in different failure morphologies around the borehole or perforation (Crook et al. 2003).

2.3.4 Failure morphology in hollow sample experiments

The specific shape of borehole breakouts beyond failure initiation in the laboratory is influenced by four factors as suggested by Lee (2005): (1) the pore fluid pressure; (2) the magnitudes of the principal stresses; (3) the size of the sample; and (4) the rock mechanical properties. Several explanations have been provided for the various breakout geometries and the mechanism of their

17

initiation and growth (Lee 2005; Haimson and Cheng 2005; Haimson 2006 and 2007). The failure mechanism suggested for uniform breakouts and V-shaped breakouts in unconsolidated sandstone in weakly consolidated sandstone suggested by various researchers using a series of HC tests are presented in detail herein.

2.3.4.1 Failure mechanism for V-shaped breakouts

Haimson and Klaestsch (2002) concluded that borehole instabilities were related to the localized shear failure, dictated either by the far-field stress conditions or by the stresses acting especially on pre-existing planes of low or no cohesion. This failure mechanism causes the so-called V-shaped breakouts that are oriented along the least horizontal far-field stress direction. Breakout dimensions (angular span and length) are linearly proportional to far-field stress magnitudes.

Based on optic microscopy, Haimson and Chang (2005) suggested that the failure mechanism leading to V-shaped breakouts in sandstones is the formation of extensile microcracks behind the borehole wall. The microcracks form around the σ_h springline and are oriented sub-parallel to the direction of σ_H. Away from the σ_h springline, microcracks turn toward the borehole wall. Microcracks coalesce to create macro fractures, which in turn form rock flakes. Breakouts form in sequence by a detachment of rock flakes. As the breakout grows deeper, it narrows due to the removal of progressively shorter flakes, eventually creating a stable V-shaped configuration. The failure mechanism leading to V-shaped breakouts in different sandstones is similar, but there might be distinct differences in the grain-scale damage patterns. The microcracking mechanism could be predominantly inter-granular or intra-granular depending on the type of contact between the grains and the strength of the cementing material.

Cuss et al. (2003) suggested that, during the early stages of loading, porosity is reduced within 50-200 mm of the cavity wall in response to stress concentration. Short, discontinuous inter-granular

18

and trans-granular extensional fractures are formed parallel to the cavity wall between grain contacts. Fracture initiation occurs first by hydrostatic grain crushing of weaker grains (e.g. altered feldspar), or of those with pre-existing damage (Stage A, Figure 2.4a), and is developed mainly in areas where other weak mineral such as red oxide staining exists. Inter-granular fractures may also develop because, in some sandstone, cement strength is less than grain strength. Despite the loading path, two diametrically opposed symmetric regions could be formed (Stage B, Figure 2.4b). These are oriented breakouts, which at non-isotropic stress conditions develop in the direction of minimum horizontal stress. Stage C, as shown in Figure 2.4c, was observed to develop as fracturing intensified in the breakout region and comminuted grains began to spall. Removal of rock flake locally altered the stress field, resulting in the formation of new fractures. This resulted in the migration of the breakout feature into the wall rock in a similar way to that hypothesized by Mastin (1984). By Stage D (Figure 2.4d), the cavity was observed to elongate in diametrically opposite directions, creating a narrow but deep breakout feature. Within the intact region, the cavity wall was preserved. Newly formed tensile fractures may form parallel to the breakout sides, causing the spalling of substantial rock flake. Such detachment created a cleaner elliptical shape as shown in Stage E (Figure 2.4e). Distortion of the cavity to an elliptical shape should result in stress intensification at the breakout tip that may lead to the progressive growth of the breakout. The side of the damaged zone shortly terminated with no transition zone.
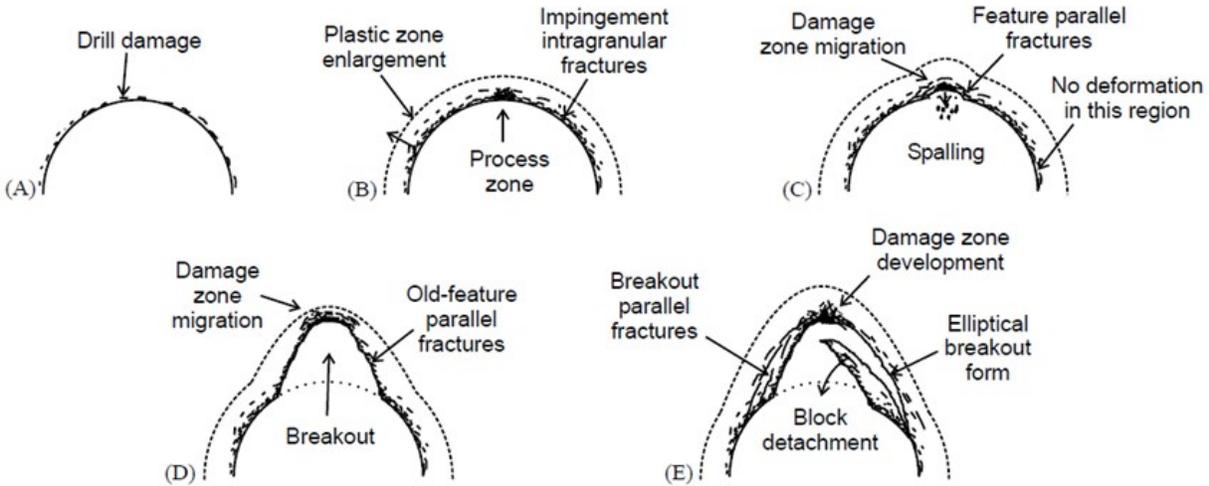
Figure 2.4: Schematic showing the process of a V-shaped breakout formation in the experimental work of Cuss et al. (2003).

2.3.4.2 Failure mechanism for uniform breakouts

Cuss et al. (2003) through their HC experiment in high-porosity sandstone observed wide breakouts that in some cases were accompanied by fractures parallel to the breakout wall. Post-mortem analysis showed different stages in failure growth. In the early stage of loading (Stage A, Figure 2.5a), they observed some porosity reduction due to the high porosity of these sandstones leading to parallel intra- and trans-granular tensile fracturing at grain point contacts. Damage was heterogeneously distributed around the borehole with fractures forming at several points around the entire periphery.

Stage B (Figure 2.5b) of the failure development was observed at the onset of breakout formation when spalling began in a preferential direction. Long thin shells spalled through shear movements where conjugate trans-granular fractures connected to the borehole parallel fractures. The low angle between conjugate fractures and bore wall resulted in a broad and shallow clean elliptical breakout form. By Stage C (Figure 2.5c), the initial bore had elongated, and breakout-parallel fractures had begun forming, which was described as splitting parallel to a free surface.

20
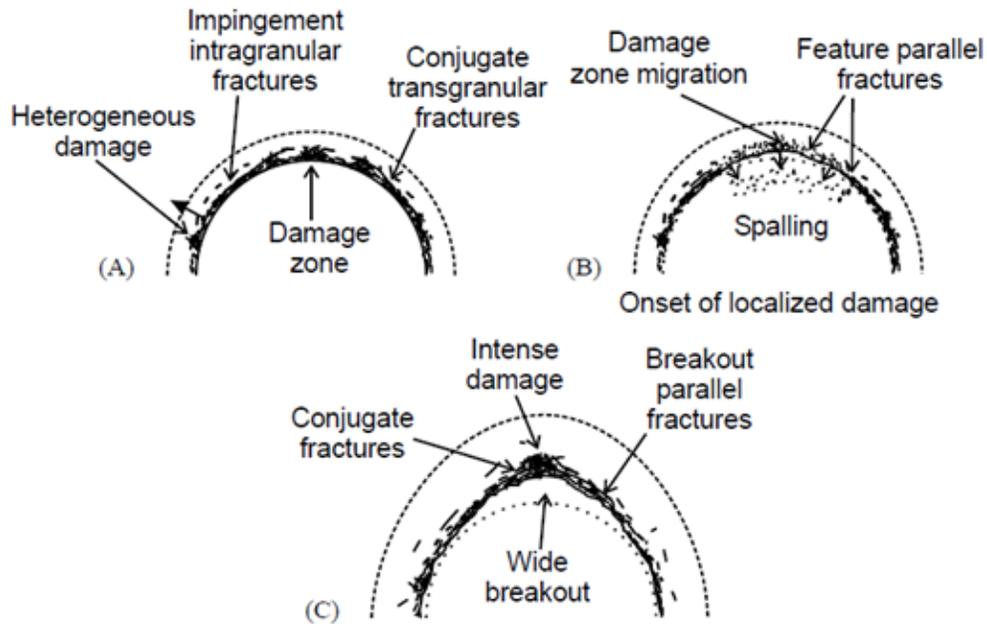
Figure 2.5: Progression of breakout development by combined extension and shear-mode cracking (After Cuss et al. 2003a)

2.3.5 Disaggregation level

Rock disaggregation due to stress concentration around the well occurs in the borehole breakout zone. In this process, the constituent particles may lose their bonding to the rest of the rock.

The granulometry of the produced sand depends mainly on the failure mechanism. As an example, Tronvoll and Fjær (1994) reported slabs of intact rock are created where distinct shear and/or tensile failure planes intersect. In the case of spalling failure, they reported production of thin flakes and grains. The grain size has also been attributed to the failure zone geometry. The solids produced during their experiments were weighed and characterized with respect to shape and size of the rock pieces as fine particles, grains, fragments, assembly of grains, flakes, and slabs. They observed that the onset of limited sand production is generally associated with initial failure of the cavity wall, and the stress at initial failure of the cavity wall appears not to be significantly affected by the fluid flow. In some cases, fine particles, single grains and smaller rock fragments associated

21

with tensile failure were observed before the initial cavity failure point. After the initial failure of the cavity, larger slabs/flakes of rock material, possibly created by shear failure, were observed. For the weaker rocks, a considerable amount of failed material remained in the cavity as flakes and slabs or relatively intact rock adhering the intact rock structure.

Uniform failure around a hole is attributed to the ductile failure of relatively weak sandstone material with low tensile strength. It has been reported to produce sand in the form of single grains, small grain assemblies and small flakes (Papamichos and Malmanger 2001). In the case of higher strength and more brittle rocks, the formation of dog-ear breakouts is reported as the predominant form of failure geometry. This breakout is formed by a combination of axial splitting (tensile failure) in the form of sub-parallel slabs and shear failure at the boundary of the slabs forming the dog-ear shape (Crook et al. 2003). The result is rock degradation in the form of slabs rather than grains.

In the case of tensile spalling, based on laboratory studies, Shen et al. (2002) observed that a series of sub-parallel cracks are formed, and the coalescence of these tensile cracks results in thin rock flakes, which may fall off the borehole wall. The spalling of the first flake opens the way for the next flake to follow suit, and the buckling and the spalling process continues sequentially. As the breakout deepens, the spalled flakes become shorter and shorter, causing the breakout span to narrow continuously (Shen et al., 2002). In the case of shear bands, Shen et al. (2002) observed in laboratory tests that the rock fragments between conjugate shear bands spall off on opposite sides of the borehole, creating visible breakouts.

Another factor is the grain-size distribution of the original rock (Tronvoll et al., 1997). Tronvoll and Fjaer (1994) conducted sand production tests on fine- and coarse-grained ultra-weak sandstones (UCS of 1-2 MPa). They concluded that the produced sand from the fine-grained

sample contained larger material elements, while only single grains were produced from the coarser sand. For instance, Tronvoll and Fjær (1994) reported that sanding tests with brine produced smaller grains of sand. The sand produced from the oil flowing test on the same material resulted in assemblies of loosely connected grains or slabs of intact rock.

2.3.6 The effect of fluid flow

For a particle to be mobilized by fluid flow, it must be completely detached from the rest of the material. Otherwise, the weak drag forces of seepage in typical operational conditions will be insufficient to remove the attached particles from the bulk body of the rock. In addition, the finer the disaggregated particles, the easier it is for the hydrodynamical forces to mobilize them.

Tronvol and Fjaer (1994) examined the effect of fluid flow on the evolution of the failure zone around a perforation cavity in the Red Wildmoor sandstone. The test samples were cylindrically shaped with a coaxial cylindrical cavity. The samples were loaded isotropically at the outer surface with fluid inflow only through the non-perforated end surface.

From the failure shape observation shown in Figure 2.6, the outer boundary of the failure zone seems to tend a spherical shape combined with axial elongation (Figure 2.6a) or plastified region at the wall (Figure 2.6b).
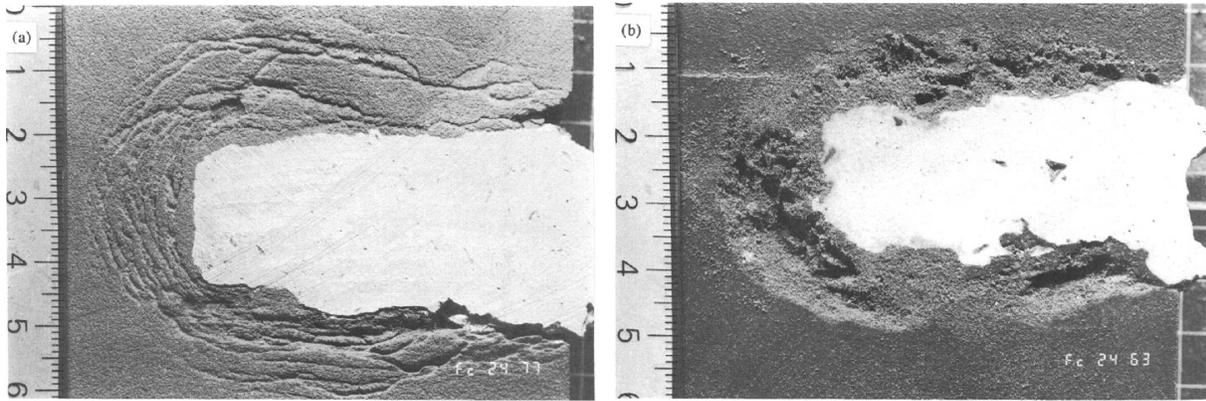
(a)   (b)

Figure 2.6: The failure shape observed in Red Wildmoor Sandstone in tests with fluid flow (a) distinct failure planes approaching a spherical shape of the failed region; (b) a continuous zone of plastified rock (from Tronvol and Fjaer, 1994).

Cross-sectional and length-sectional scans in two perpendicular directions of a specimen after a fluid flow test are shown in Figure 2.7. The cavity is enlarged laterally towards a spherical geometry. The flow channel also tends to orient itself perpendicular to the lamination. Sand produced during this stage of the experiments consisted mainly of single grains and smaller rock fragments.
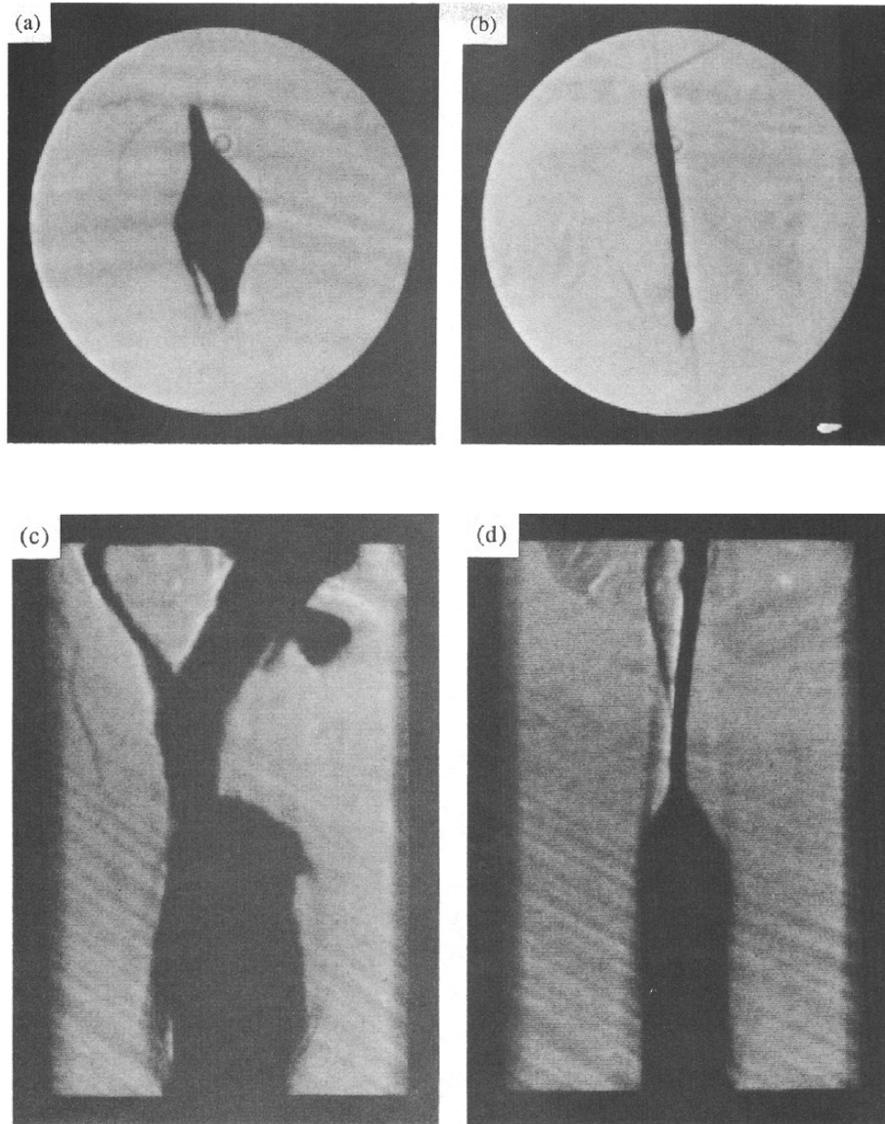
Figure 2.7: X-ray CT scans of cross-section and length-sections of Red Wildmoor Sandstone applied in a cavity failure experiment with fluid flow (from Tronvol and Fjaer, 1994).

Figure 2.8 shows corresponding X-ray CT length-sections and cross-sections of one specimen after a test with fluid flow. It was observed that a failure zone propagating in the axial direction, oriented perpendicular to the rock lamination. The sand produced was typically slabs of rock or assemblies of loosely connected grains with oil as the flowing fluid. In tests with the flow of brine, smaller grains of sand were produced together with a few slabs.

25
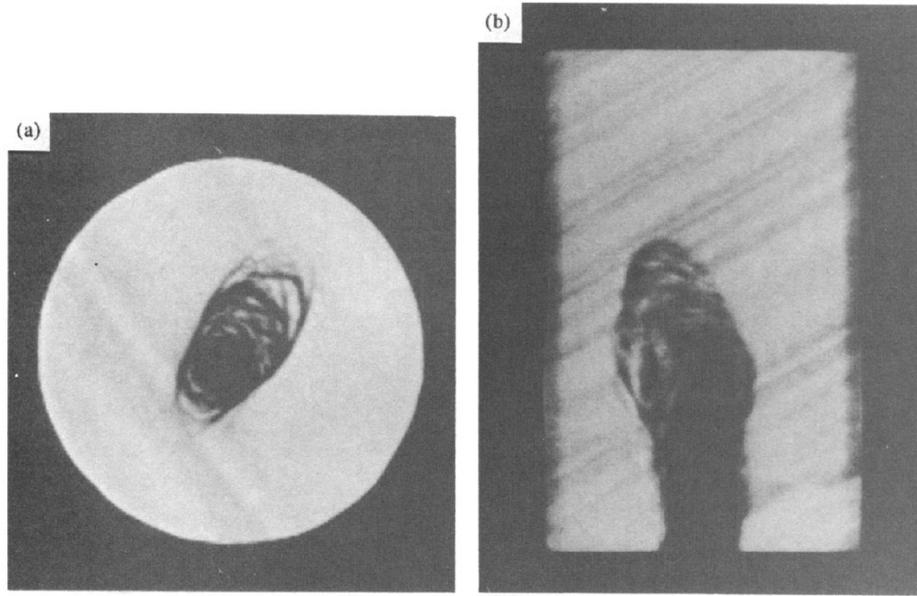
Figure 2.8: X-ray CT scans of cross-sections and length-sections of a specimen (core material No.1) in cavity failure experiment with fluid flow (from Tronvol and Fjaer, 1994).

The relatively extended damaged zone indicated that a different failure model and sand production mechanism may be present in the case of water flow. In some tests, Tronvol and Fjaer (1994) also observed that a continuous failure zone of changing porosity was extended a few millimeters into the surrounding rock from the cavity surface. Also, a failure zone propagating from the cavity bottom in the axial direction of the rock specimen was also observed. The fluid flow thus appears to influence, to a large degree, the direction of failure propagation.

Hayatdavoudi (1999) found that sand liquefaction due to water hammer pressure pulses is a likely mechanism for massive sand production in water injection wells. Liquefaction is defined as the spontaneous loss of shearing resistance due to a collapse of soil or rock structure in a fully saturated granular material. Water hammer is, in a general term, the generation, propagation, and damping of pressure waves in pipes due to the sudden arrest or sudden change in velocity of a flowing fluid. It occurs due to sudden velocity changes such as quick shutting of the well. In numerical modelling,

a sudden change in pressure in each fluid grid will lead to pore water pressure increase, thus leading to liquefaction and sand production.

2.4 Review of DEM fluid –solid coupling techniques

Several researchers have been working on the development of solid-fluid coupling techniques in DEM in the past two decades. An overview of these approaches is presented here.

2.4.1 DEM coupled with computational fluid dynamics (CFD)

Tsuji et al. (1993) developed a solid-fluid coupling scheme for fluidized beds. They discretized the fluid phase with fluid cells which are larger than the particle size but relatively small compared to the size of the whole domain. The mean values of fluid pressure and velocity are calculated within each fluid cell. Fluid force is calculated in each cell and applied to each discrete particle.

Kafui et al. (2002) developed a fluidized bed model for chemical engineering applications. The model was DEM-based with gas flow coupling. The gas flow was treated as a continuum by solving the Navier-Stokes equations. The model was used in simulating fluidisation of a pseudo-2D particle bed. The results were consistent with observations and empirical correlations.

Latham et al. (2008) used discrete element and combined finite-discrete element methods (FEM-DEM) to model the granular solid skeleton of randomly packed units coupled to a CFD code which resolves the wave dynamics through an interface tracking technique. The coupling work used a dual mesh approach. One mesh is used across the whole solution domain in which the fluids equations are solved and the second mesh contains a finite element representation of the solid structures.

Chan and Tipthavonnukul (2008) developed a coupled method for hydro-transport of solid particles in pipelines or open channels. They used the finite volume scheme with a pressure

correction algorithm for the flow simulation. The flow field is divided into a finite number of sub-regions. The continuity equation and the Navier-Stokes equations are both applied. One difficulty with above approaches is that the solutions of the mass balance and three momentum equations for fluid flow are computationally demanding.

Viré et al. (2012) performed modeling of fluid-solid interactions using an adaptive mesh fluid model coupled with a combined finite-discrete element model. They solved the Navier-Stoke equations with an unstructured numerical mesh, similar to the method used by Pain et al. (2001a 2005b). The method was verified using a model that allows the flow of fluid past a falling sphere at small and moderate Reynolds numbers.

Climent et al. (2014) developed a 3D DEM-fluid flow model by coupling DEM and Computational Fluid Dynamics (CFD). The simulation is focused on the effect of different far field boundary stress and outer boundary pore pressure conditions. The results are consistent with the analytical solution by Risnes et al. (1982). However, their simulations are limited to certain boundary stress and pore pressure conditions. Furthermore, they did not consider permeability change due to sand production near the wellbore.

Most of the solid-fluid coupling techniques developed recently follow the fluid flow and fluid-solid interaction calculation method proposed by Cheung (2010), who developed a 3D DEM coupled with fluid flow in sand production simulation. The fluid phase is the same as Tsuji, and the governing equations of such type of fluid calculation system are the continuity and Navier-Stoke equations:

$$\frac{\partial n}{\partial t} = -(\nabla n u) \qquad\qquad [2.6]$$

$$\frac{\partial(nu)}{\partial t} + (\nabla nuu) = -\frac{n}{\rho_f}\nabla p - \frac{n}{\rho_f}\nabla\tau + ng + \frac{f_{interaction}}{\rho_f} \qquad [2.7]$$

where n is the porosity, u is the average velocity of the fluid, ρ_f is the density of the fluid, t is

time, τ is the fluid viscous stress tensor, g is the gravitational acceleration, and $f_{interaction}$ is the

fluid-particle interaction term in units of force per unit volume, which is given by:

$$f_{interaction} = \beta(v - u) \qquad [2.8]$$

where v is the average velocity of the particle, and β is a parameter that depends on rock's porosity:

$$\beta = \frac{1-n}{d_p^2 n^2}\left(150(1-n)\mu_f + 1.75\rho_f d_p|v-u|\right), when\ n < 0.8 \qquad [2.9]$$

$$\beta = \frac{3}{4}C_D\frac{|v-u|\rho_f(1-n)}{d_p}n^{-1.7}, when\ n > 0.8 \qquad [2.10]$$

where μ_f is the viscosity of the fluid, d_p is the average diameter of sand particles, and C_D is the

drag coefficient in relation to Reynolds number R_e:

$$C_D = \begin{cases} \frac{24}{R_e}(1 + -0.15R_e^{0.687}), R_e \leq 1000 \\ 0.44, R_e \geq 1000 \end{cases} \qquad [2.11]$$

$$R_e = \frac{n|v-u|\rho_f d_p}{\mu_f} \qquad [2.12]$$

The fluid-solid interaction force is then calculated and applied to the solid particle in DEM model.

The applied force on each solid particle i with diameter d in direction j are calculated as:

$$f_{i,j} = -\frac{1}{6}\pi d^3 \frac{\beta_j(v_j - u_j)}{1 - n}$$

[2.13]

The total fluid forces on a particle consist of drag force, buoyancy force and forces caused by the pressure gradient. The fluid flow calculates the fluid velocity from which a force is added to the particle equilibrium equation. On the other hand, DEM calculates particle velocities and porosity.

The large majority of past studies (e.g. Cook et al., 2004; Li et al., 2006; Quadros et al., 2010; Boutt et al., 2011) involve 2D discrete models. Two-dimensional models offer a good qualitative insight. However, they are not suitable for applications in general 3D reality. Further, solid particles in 2D models use are bar-shaped, and the loading conditions in the direction normal to the model plane are not realistic. Grof et al. (2009) developed a 3D DEM-fluid flow model. Their study was focused on a small-scale phenomenon involving only a few particles. Cheung (2010) developed a 3D DEM coupled with the 1D fluid flow for the simulation of sand production. However, they neglected the gradual change in the wellbore geometry and the concomitant variation of the fluid flow directions near the evolving cavity face. The circumferential and vertical flows were not taken into consideration as they might be significant. Besides, the effects of the anisotropic boundary stress on sand production are also considered to be important, which required further research.

2.4.2 DEM coupled with lattice Boltzmann method (LBM)

The Lattice Boltzmann Method (LBM), originally developed from McNamara and Zanetti (1988), has been used for a wide range of applications including particulate suspensions (Ladd and Verbery, 2011), hydraulic fracturing (Boutt et al., 2007), and turbulent flows (Hou et al., 1996.)

Cook (2001) developed a coupled numerical method for the direct simulation of particle-fluid systems. The fluid flow was solved using the LBM method, which can accurately reproduce Navier-Stokes equations. Cook et al. (2003) validated the developed method through the comparison of simulation results with the analytical solutions for cylindrical Couette flow. The results show accurate computation of fluid flow and particle forces. They also performed the erosion simulation of sanding near the wellbore. Results indicated physically realistic behavior.

Feng et al. (2007) coupled the LBM with the DEM solutions and incorporated of large eddy for the simulation of particle transport in turbulent fluid flows with high Reynolds number. They applied the model in a 2D particle transport problem comprising 70 large particles in fluid flow with high Reynolds number with reasonable results. Feng et al. (2010) extended their model to 3D and simulated a simplified laboratory model of vacuum dredging system for mineral recovery. The numerical results showed a good correspondence to laboratory observations.

Han (2012) used the LBM-DEM coupling to simulate the sand arch test. The collapse and re-forming of sand arches in the perforation cavity under increasing fluid pressure gradient was observed in numerical simulation, as observed in the physical experiments.

Lomine et al. (2013) used the LBM-DEM coupling method to illustrate on a laboratory hole erosion test in 2D. Both detachment and transport of particle were modeled. The erosion law deduced from the simulations agreed with the law verified and used experimentally.

The LBM is based on microscopic kinetic models (Cui, 2012). In LBM, the fluid domain is divided into a regular lattice. The fluid is represented as packets of mass that move on a regular lattice, so that configuration of fluid particles varies in every calculation cycle, leading to a changing flow field. Collision and redistribution of fluid packets occur at the lattice nodes according to relationships that conserve mass and momentum. Han et al. (2007) pointed out that LBM avoids

solving the Navier-Stokes equations but involves only simple local operations, which is less computational demanding compared with the CFD.

In LBM, the fluid domain is divided into a square lattice with unity spacing, and the velocity field is discretized into nine prescribed vectors, as shown in Figure 2.9. Fluid particles are allowed either to remain at their current locations or to move to the adjacent nodes with velocities e_i.
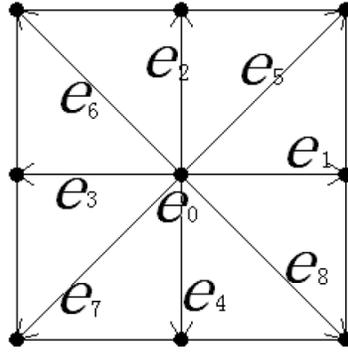
Figure 2.9: Nine prescribed velocities in a D2Q9 model (Feng et al., 2007)

Cui (2012) derived the governing equations for the density distribution function f_i along with the prescribed velocities e_i based on the basic formulation of Cook (2001):

$$f_i(x + e_i \Delta t, t + \Delta t) = f_i(x, t) - \frac{1}{\tau}\left(f_i(x, t) - f_i^{eq}(x, t)\right) \qquad [2.14]$$

where f_i represents the probable quantity of micro-particles at a lattice node moving along the ith direction with velocity e_i at a particular time, τ is a dimensionless relaxation time, and f_i^{eq} are a set of distribution functions at which the systems are defined as the equilibrium:

$$f_i^{eq} = t_i \rho_f \left[1 + 3(e_i \cdot u) + \frac{9}{2}(e_i \cdot u)^2 - \frac{3}{2}u \cdot u\right] \qquad [2.15]$$

where ρ_f is the fluid density, and u is the flow velocity.

32

An Eulerian flow field is defined by the configurations of micro-particles. Within each LBM time step, two phases of computations take place. Firstly, the micro-particles encounter one another at node x, and change their original direction and velocities by collision, known as "collision phase". The post–collision distribution is then calculated from the right hand side of Equation 2.14. The updated distribution at node x is transferred to the adjacent nodes, giving an updated description of the flow field, known as "streaming phase" (Cui, 2012). The macroscopic fluid variables can also be solved from the summation of adjacent node information:

$$\rho = \sum_{i=0}^{i=8} f_i$$

$$\Delta P = \frac{C^2}{3} \Delta \rho \qquad [2.16]$$

$$u = \frac{\sum_{i=0}^{8} f_i e_i}{\rho}$$

where C is lattice speed, ΔP and $\Delta \rho$ are the changes in pressure and density values, respectively.

The interactions between fluid and solid particles in the context of LBM require mapping of solid particles onto the LBM Eulerian lattice, as shown in Figure 2.10.
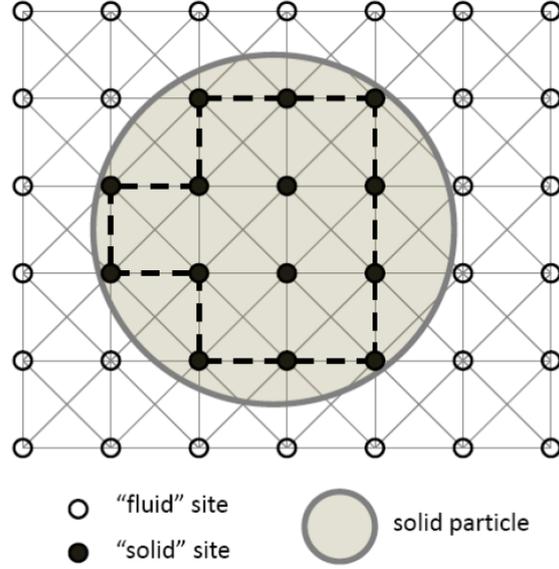
Figure 2.10: Stepwise lattice representation of a circular solid particle (from Han, 2012).

Nobel and Torczynski (1998) introduced the Immersed Moving Boundary (IMB) scheme in which a node cell is introduced for each lattice node, with its size identical to a lattice square, and located at the center of the cell. The standard LBM equation is then modified as:

$$f_i(x + e_i \Delta t, t + \Delta t) = f_i(x,t) - \frac{1}{\tau}(1 - B)\left(f_i(x,t) - f_i^{eq}(x,t)\right) + B\Omega_i^S$$

[2.17]

$$\Omega_i^S = f_{-i}(x,t) - f_i(x,t) + f_i^{eq}(\rho, u_s) - f_{-i}^{eq}(\rho, u)$$

where u_s is the velocity of the solid particle at time t, and $-i$ is used to denote the distribution component having the opposite direction to i, B is a weighting function that depends on the cell solid fraction or solid ration, ε, defined here as the fraction of the lattice cell area covered by a solid, and the dimensionless relaxation time τ as:

$$B(\varepsilon, \tau) = \frac{\varepsilon(\tau - 0.5)}{(1 - \varepsilon) + (\tau - 0.5)}$$

[2.18]

34

Here ε is the volumetric fraction overlapped by the solid at a site. If ε equals to 1, the site is fully covered by solid; if ε equals to 0, the site is completely filled with fluid (In this case, B equals to 0, the collision rule reduces to the original collision operation).

So the force and torque imposed by fluid on the solid are:

$$F_f = C\Delta h \left(\sum_n B_n \sum_i \Omega_i^s e_i \right) \tag{2.19}$$

$$T_h = C\Delta h \sum_n (x_n - x_s) \times \left(B_n \sum_i \Omega_i^s e_i \right) \tag{2.20}$$

where the summations are performed over all the boundary nodes, Δh is the unity lattice space, x_n is the location of lattice node, x_s denotes the centroid of the solid particle at time t. Fluid-particle coupling is realized at each time step by first computing the fluid solution, and then updating the particle positions.

However, although the core LB operation is effective, the total computational cost could be substantial since a sufficiently fine lattice is necessary and small time steps are required. Compared with the CFD, the effect of fluid flow to solid particles is still accomplished by introducing an additional force on the particle.

2.4.3 DEM coupled with solid deformation pore pressure (SDP)

One particular issue in the fluid flow-DEM calculation is the permeability and porosity change in each fluid cell between the cycles of calculation. Besides all existing DEM models do not take into consideration the development of excess pore water pressure, which is the focus of this study.

Hakuno and Tarumi (1988) developed a method to model liquefaction based on detecting all the pores among particles and connecting them by pipes. Pore water pressure was calculated by assuming water had constant volume elasticity and water pressure was proportional to the pore volume. Fluid flow between each pore space and its adjacent pores was calculated based on Darcy's law. This method resulted in a complicated calculation procedure and required subsequent manipulation.

Nakase et al. (1999) improved Hakuno and Tarum's method by implementing square-cell element each containing 15 particles. The pore pressure generation in each cell corresponded to particle movement in the neighboring cells and was proportional to the decrease of pore volume. The fluid force applied on the particle depended on the pore pressure gradient between neighboring cells.

Mori et al. (2001) studied the liquefaction analysis of River Dike using a two-dimensional discrete element model. In their study, excess pore water pressure was calculated in estimating the large permanent displacement due to liquefaction at the microscope level. The accumulative excess pore water pressure was induced by a combination of shear force and effective normal force. The excess pore water pressure caused by the shear force was related to the dissipative energy and stored elastic energy in the model.

Bonilla (2004) performed a DEM undrained simulation with fluid coupling by using two-dimensional assemblies of elliptical particles. The pore volume was identified by constructing a polygon around the specified pore surrounded by particles, as shown in Figure 2.11.
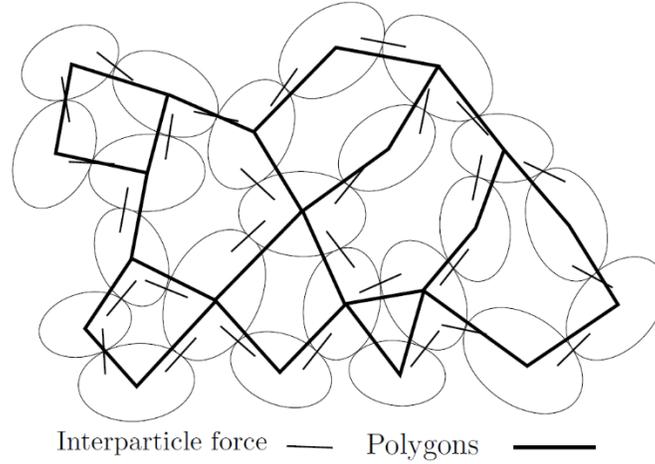
Figure 2.11: Calculation of polygons enclosing the assembly's void (Bonilla, 2004)

The volumetric pore changes experienced due to particle rearrangement under external forces is then calculated from volume change of the polygon. The pore pressure change Δu_n in any pore space n surrounded by particles is then calculated from pore volume change ΔV_n:

$$\Delta u_n = B_f \frac{\Delta V_n}{V_n} \qquad [2.21]$$

where V_n is the original volume of pore n and B_f is the bulk modulus of the fluid.

The fluid flow path was constructed by the flow network by joining the centers of adjacent polygons (Figure 2.12).

Fluid network ········ Polygons ──────
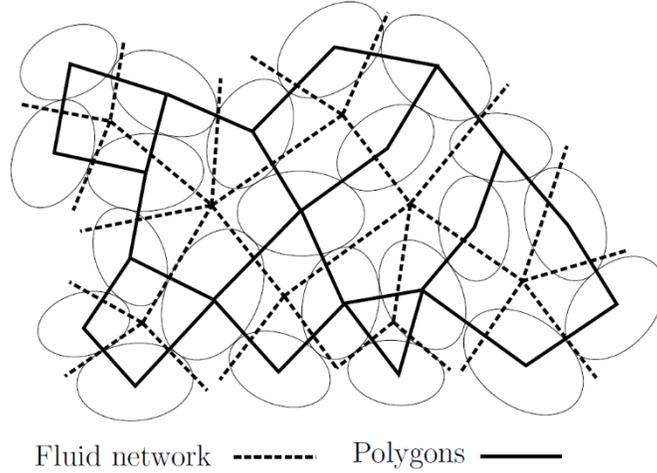
Figure 2.12: Flow network construction for a set of polygons (Bonilla, 2004)

The pore pressure forces on the particles are applied by the integration of pore pressure difference on adjacent centers of the polygons. Consider a section of an ellipse bounded by the contact vectors l_a^c and l_b^c (start from the center of the ellipse and end at the contact point) depicted in Figure 2.13 below, the horizontal and vertical components of the pore pressure induced force F_1^n and F_2^n resulting from pore pressure u_n in pore n are given by:

$$F_1^n = -u_n(a_2 - b_2)\,\Delta$$

$$F_2^n = u_n(a_1 - b_1)\,\Delta$$

[2.22]

where Δ is the thickness of the particle. a_1, a_2 and b_1, b_2 are the horizontal (subscript as 1) and vertical (subscript as 2) component of the contact vector l_a^c and l_b^c.

In calculating the pore pressure of a pore n, a closed polygon is established by connecting the centers of the elliptical elements surrounding the pores (shown in Figure 2.12). Considering travelling from one center of an element to the center of the adjacent element in a clockwise manner, the vectors a and b in equation 2.22 are assigned by the surface of the element bounded

within the polygon connecting the centers as shown in Figure 2.13(a). If the calculation is performed in a counter-clockwise manner, the assignment of the vectors a and b is given by Figure 2.13(b).

For both cases, the contact vectors are computed and the vector first encountered along the path is identified as l_b^c, the second contact vector is l_a^c.

a)   b)
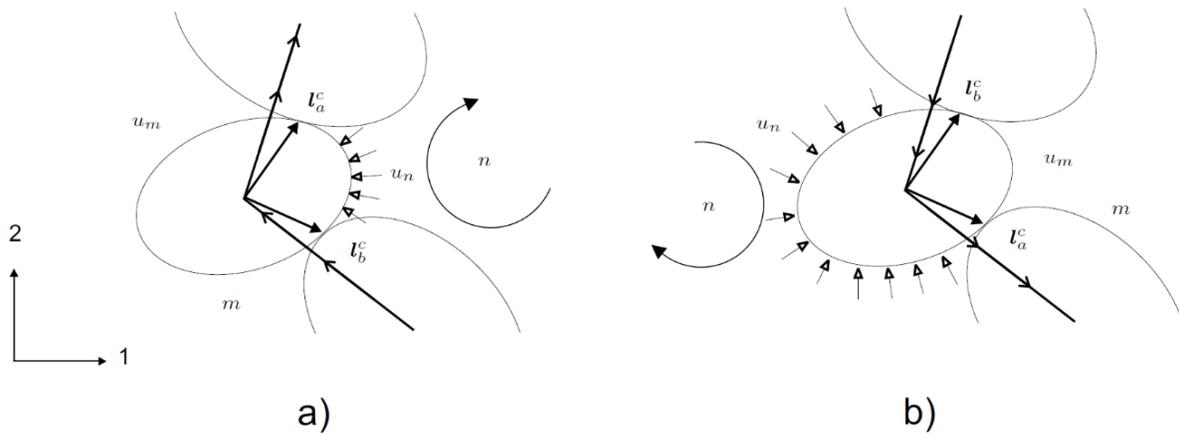
Figure 2.13: The pore pressure force computation from contact vectors (Bonilla, 2004)

Bonilla observed the temporary liquefaction in DEM simulations. From Bonilla's recommendations, the computational efficiency of this method needs to be improved.

It is not easy to calculate excess pore water pressure using DEM since it is difficult to determine pore space connectivity and pore space deformation in a discontinuum. In this research, a new idea is proposed to incorporate excess pore water pressure calculation in DEM simulation by introducing a new water particle element which has a specific stiffness that enables the calculation of excess pore pressure due to pore space deformation. The new approach can be used to simulate wet granular deformation using DEM.

39

Chapter 3. Liquid-solid interaction for flow-driven perturbation of boundary conditions[1]

3.1. Introduction and background

As described in Chapter 2, problems such as sand production involve the interaction between solid particles and flowing fluid, which must be accounted for by coupling the mechanical and fluid flow calculations. To simulate the interaction at the soil particle scale, the solid DEM model must be coupled with a fluid model (Zhu et al., 2007). Application of solid and fluid coupled flow is an important issue in engineering problems. Some examples are: hydro-transport in pipelines or open channels (Chan and Tipthavonnukul, 2008), landslides induced debris flow (Zhao, 2014), and sand production in sandstone reservoir (Climent et al., 2014). This chapter focuses on the sand production problem and the effect of fluid flow on the sanding process.

Sanding is the production of formation sand driven by de-cementation of the formation sand around the borehole and the flow of reservoir fluid during the oil recovery process. Problems associated with sand production include erosion of pipelines and surface facilities, wellbore intervention costs, and environmental impacts. Large amounts of sand production in a short period of time may clog up wells, damage well equipment, and destabilize wellbores due to loss of materials (Climent et al., 2014). On the other hand, controllable sand production may increase wellbore productivity and reduce wellbore completion costs (Saucier, 1974). Therefore,

---

understanding sand production mechanisms and the ability to predict and manage the rate of sand production are important.

While both experimental and analytical models of sand production are necessary to understand the phenomenon, numerical models are essential for realistic predictions (Rahmati et al., 2013a). Sand production in oil wells is often analyzed using continuum models. Papamichos and Vardoulakis (2005), Nouri et al. (2006), obtained some good results by using continuum based analysis on sand production problems. Azadbakht et al. (2012) linked finite difference code with a finite element method for volumetric prediction of sand production in injector wells. The model was validated using physical model tests carried out under various stresses and fluid flow conditions. However, the process of sandstone de-cementation involving the development of cracks and micro-cracks in the inter-granular bonding material and grain detachments due to seepage forces are intrinsically problems of a discontinuum and are not compatible with the assumptions of continuum mechanics. An alternative approach that overcomes some of these limitations is adopting the DEM for this problem. In order to apply the DEM in the sanding problem, it is necessary to calculate fluid flow and pore water pressure in the discontinuum. Coupling the DEM model with continuum fluid computation allows the simulation of solid-fluid interactions.

The application of DEM coupled with solid-fluid interactions on sand production has been attempted in a few research studies in the past. 2D discrete models were used in the majority of previous studies (e.g. Preece et al., 1999; Cook et al., 2004; Li et al., 2006; Quadros et al., 2010; Boutt et al., 2011). Two-dimensional models offer a good qualitative insight. However, they are not suitable for application in general 3D reality. Further, solid particles in 2D models are bar-shaped, and the loading conditions in the direction normal to the model plane are not realistic. It cannot model plane stress or plane strain conditions.

Grof et al. (2009) developed a 3D DEM-fluid flow model. Their study was focused on a small-scale phenomenon involving only a few particles. Cheung (2010) developed a 3D DEM coupled with 1D fluid flow for the simulation of sand production. However, they neglected the gradual change in the wellbore geometry and the concomitant variation of fluid flow directions near the continuously changing cavity face. Han (2013) performed numerical simulation on sand production by using the lattice Boltzmann method (LBM) implemented PFC coupled with fluid flow. The coupling system was able to reproduce the collapse and reconstruction of a sand arch. Climent et al. (2014) developed a 3D DEM-fluid flow model by coupling DEM and Computational Fluid Dynamics (CFD). The simulation is focused on the effect of different far field boundary stress and outer boundary pore pressure conditions. The results were consistent with analytical solution by Risnes et al. (1982). However, their simulations were limited to a certain boundary stress and pore pressure conditions. Furthermore, they did not consider permeability change due to sand production near the wellbore.

Van Den Hoek et al. (2000) developed an analytical solution to calculate the failure of the initial cavity in a hollow cylinder sample and compared with experimental results. They studied the influence of the far field stress and pressure drawdown on the failure of the initial cavity. By calculating the maximum allowable fluid flow rate, they concluded that the primary role of fluid flow in sand production is the transport of loose sand resulting from compression failure rather than the failure of the intact sandstone itself. The tensile failure can only take place around small cavities in weak sandstones or in the case of very highly localized pore pressure gradient.

In this Chapter, a new SPF approach to simulate sand production by using 3D DEM-fluid flow model is proposed. A new method to update the variations of permeability and porosity for each grid block in response to both solid deformation and sand production is conducted. The verification

of the model against analytical solutions is carried out. The verified model is then applied to the simulation of sanding for a synthetic laboratory-scale problem. The effects of boundary stresses and fluid flow on sandstone degradation and sand production is then investigated.

3.2. Proposed methodology

3.2.1 Discrete Element Method

The Discrete Element Method (DEM) was originally proposed by Cundall and Strack (1979) which consists of discrete interacting particles. The advantages of DEM are that it provides micromechanical quantities and parameters that cannot be easily obtained from laboratory tests, and it can capture particle-scale interactions underlying the observed macro-scale behaviour of soil and rock. In sand production analysis, different shapes of breakout near a wellbore can be captured using DEM.

DEM analysis involves modeling a granular material using particles that usually have simple geometries such as spheres in 3D or disks in 2D. These ideal particles are usually assumed to be rigid but small overlaps are allowed at the contact points, referred as soft contacts. Soft-contact refers to rigid particles are allowed to overlap one another at the contact points. The magnitude of the overlap is related to the contact force via the force-displacement law, and all overlaps are small in relation to particle sizes. The particles are rigid meaning the size of the particles is unchanged. Deformation only occurs at the particle contact points therefore the contacts are referred to as soft contact. At any inter-particle contact, a contact stiffness model is used to relate the contact force to the overlapping of elements. The finite displacements and rotations of discrete bodies including complete detachment are allowed among particles.

In this study, the parallel-bond model in the Particle Flow Code (PFC) is used. The parallel bond model which is implemented in PFC^{3D} (Itasca, 2008) is considered to be an appropriate bonding model for DEM models of cemented sands (Potyondy and Cundall, 2004). It includes a set of springs with constant normal and shear stiffnesses, acting in parallel with the linear contact springs. The parallel-bonds are supposed to represent a finite amount of cementing material deposited between particles which are able to transfer both forces and moments. The parameters required to define a parallel-bond are the normal and shear stiffness, the normal and shear strength, and the degree of bonding. When the forces acting on the parallel bond reach either its normal or shear strength limits, the parallel bond is erased and being treated as bound failure. The linear contact model is used after the failure of the parallel bonds. The load-displacement relationship between two contacting bodies is represented by linear springs inserted at particle contact. The three input parameters are the particle normal and shear stiffness, and the inter-particle friction coefficient.

The calculations performed in the DEM alternate between the application of Newton's second law to the particles and a force-displacement law at the contacts. Newton's second law is used to determine the translational and rotational motions of each particle arising from the contact forces, applied forces and body forces acting on it, while the force-displacement law is used to update the contact forces arising from the relative motion at each contact. The calculation cycle is illustrated in Figure 3.1.
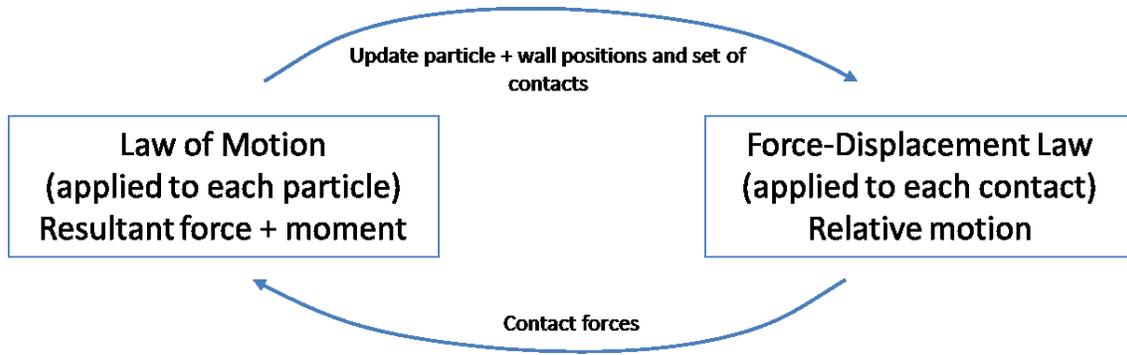
Figure 3.1: DEM calculation flow chart (Itasca, 2008)

The force-displacement law relates the relative displacement between two entities at a contact to the contact force acting on the entities. For both ball-ball and ball-wall contacts, this contact force arises from contact occurring at a point. For ball-ball contact, an additional force and moment arising from the deformation of the cementations material represented by a parallel bond can also act on each particle. The contact force vector F_i is calculated by:

$$F_i = F_i^n + F_i^s \qquad \text{[3.1.]}$$

where F_i^n and F_i^s denoted the normal and shear force vectors respectively. The normal and shear forces are calculated by:

$$F_i^n = K^n U^n \qquad \text{[3.2.]}$$

$$F_i^s = K^s U^s \qquad \text{[3.3.]}$$

where U^n and U^s are the contact displacements in normal and shear direction.

The motion of a single rigid particle is determined from the resultant force and moment vectors acting on it, and can be described in terms of the translational motion of a point in the particle and

the rotational motion of the particle. The equations of motion can be expressed relates the resultant force to the translational motion and the resultant moment to the rotational motion:

$$F_i = m\ddot{x}_i \text{ (Translational motion)} \qquad [3.4.]$$

$$M_i = \dot{H}_i \text{ (Rotational motion)} \qquad [3.5.]$$

where F_i is the resultant force, m is the total mass of the particle, $\ddot{x}_i$ is the acceleration of the specified particle, M_i is resultant moment acting on the particle, and $\dot{H}_i$ is the angular momentum of the particle.

By integration, the incremental velocity and displacement of each particle are calculated for the current time increment. The locations of all the particles are updated for the next calculation cycle.

In order to account for the interaction with fluid, the equations of motion are modified with an additional forcing term, F_{ifluid} which is fluid force applied on the particle:

$$F_i + F_{i\,fluid} = m\ddot{x}_i \qquad [3.6.]$$

3.2.2 DEM and fluid flow coupling scheme

The commercial software Particle Flow Code (PFC^{3D}) is used as a tool for the implementation of the numerical scheme in DEM phase. New code is developed for new DEM elements. The commercial software MATLAB is used as a tool for the implementation of the numerical scheme in the fluid phase.

It is essential to perform fluid flow calculations along with solid deformation analysis in the sanding model. The seepage force due to fluid flow affects grain detachment and mobility and

could mobilize disaggregated particles. On the other hand, grain motions can affect fluid flow since it changes the porosity and permeability of the material. Therefore, fluid flow and grain motions are a coupled phenomenon and should be analyzed in a coupled manner.

The formulation used in fluid flow calculation is presented here in the cylindrical coordinate system since wellbore in some cases can be simplified into a 2D axisymmetrical problem. The continuity equation for fluid flow in a differential element is expressed as the difference between the entering and exiting mass being equal to accumulated mass:

$$-\frac{1}{r}\frac{\partial}{\partial r}(rv_r\rho) - \frac{1}{r}\frac{\partial}{\partial \theta}(v_\theta\rho) - \frac{\partial}{\partial z}(v_z\rho) = \frac{d}{dt}(\phi\rho) \qquad [3.7.]$$

where v_r, v_θ, v_z are the fluid velocities in the radial, tangential and vertical directions, ϕ is the porosity of rock, ρ is the density of fluid, and t is time.

From Darcy's equation (Dake, 1998), the velocity of fluid in the radial, tangential and vertical directions can be expressed as:

$$v_r = -\frac{k}{\mu}\frac{\partial P}{\partial r}; \ v_\theta = -\frac{1}{r}\frac{k}{\mu}\frac{\partial P}{\partial \theta}; \ v_z = -\frac{k}{\mu}\frac{\partial P}{\partial z} \qquad [3.8.]$$

where k is the rock permeability, μ is the fluid viscosity, $\partial P/\partial r$, $\partial P/\partial \theta$, $\partial P/\partial z$ are the fluid pressure gradients in the radial, tangential, and vertical directions.

The compressibility of the fluid is expressed as:

$$C_f = \frac{1}{\rho}\frac{\partial \rho}{\partial p} \qquad [3.9.]$$

Combine Equations 3.7. to 3.9.:

$$\frac{1}{r}\frac{\partial}{\partial r}\left(r\frac{k}{\mu}\frac{\partial P}{\partial r}\rho\right) + \frac{1}{r}\frac{\partial}{\partial \theta}\left(\frac{1}{r}\frac{k}{\mu}\frac{\partial P}{\partial \theta}\rho\right) + \frac{\partial}{\partial z}\left(\frac{k}{\mu}\frac{\partial P}{\partial z}\rho\right) = \rho\frac{\partial \phi}{\partial t} + \phi\frac{\partial \rho}{\partial t}$$

[3.10.]

$$= \rho\frac{\partial \phi}{\partial t} + \phi C_f\rho\frac{\partial P}{\partial t}$$

In Equation 3.10., the term $\partial \phi / \partial t$ is obtained from DEM calculations. Fluid compressibility is assumed to be constant. The solution of the fluid flow equation by using finite difference approximation is shown in Appendix A: The Finite Difference Approximation to Fluid flow Equations.

The fluid force calculation method adopted here is based on the assumption of a continuum where the size of the grid block for flow calculation is relatively large compared to the average particle diameter in the grid block. A shape function is used to interpolate pore pressures at any point inside the grid block from the calculated nodal pressures in the cylindrical coordinate system as shown in Figure 3.2. Pore pressure inside a grid block can be calculated from:

$$P(r,\ \theta) = N_i(r,\ \theta)d_e$$

[3.11.]

$$N_i = [N_1 \quad N_2 \quad N_3 \quad \cdots \quad N_8];\ d_e = \begin{Bmatrix} P_1 \\ P_2 \\ \cdots \cdots \\ P_8 \end{Bmatrix}$$

[3.12.]

where d_e is the nodal pressure array for the grid block, and N_i is the shape function given by Equation 3.13.

$$N_1 = \left(1 - \frac{r - r_1}{r_2 - r_1}\right)\left(1 - \frac{\theta - \theta_1}{\theta_2 - \theta_1}\right)\left(1 - \frac{z - z_1}{z_2 - z_1}\right)$$

$$N_2 = \left(\frac{r - r_1}{r_2 - r_1}\right)\left(1 - \frac{\theta - \theta_1}{\theta_2 - \theta_1}\right)\left(1 - \frac{z - z_1}{z_2 - z_1}\right)$$

$$N_3 = \left(\frac{r - r_1}{r_2 - r_1}\right)\left(\frac{\theta - \theta_1}{\theta_2 - \theta_1}\right)\left(1 - \frac{z - z_1}{z_2 - z_1}\right)$$

$$N_4 = \left(1 - \frac{r - r_1}{r_2 - r_1}\right)\left(\frac{\theta - \theta_1}{\theta_2 - \theta_1}\right)\left(1 - \frac{z - z_1}{z_2 - z_1}\right)$$

[3.13.]

$$N_5 = \left(1 - \frac{r - r_1}{r_2 - r_1}\right)\left(1 - \frac{\theta - \theta_1}{\theta_2 - \theta_1}\right)\left(\frac{z - z_1}{z_2 - z_1}\right)$$

$$N_6 = \left(\frac{r - r_1}{r_2 - r_1}\right)\left(1 - \frac{\theta - \theta_1}{\theta_2 - \theta_1}\right)\left(\frac{z - z_1}{z_2 - z_1}\right)$$

$$N_7 = \left(\frac{r - r_1}{r_2 - r_1}\right)\left(\frac{\theta - \theta_1}{\theta_2 - \theta_1}\right)\left(\frac{z - z_1}{z_2 - z_1}\right)$$

$$N_8 = \left(1 - \frac{r - r_1}{r_2 - r_1}\right)\left(\frac{\theta - \theta_1}{\theta_2 - \theta_1}\right)\left(1 - \frac{z - z_1}{z_2 - z_1}\right)$$
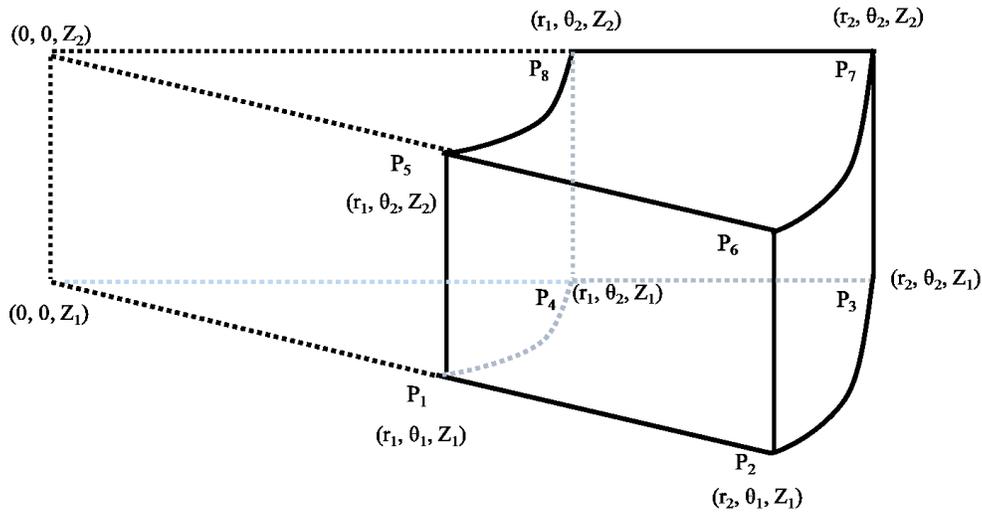
Figure 3.2: A grid block for flow calculations and nodal pressures in cylindrical coordinate system

Fluid forces on the particles in the grid block are calculated by integrating the pressure over the particle surface (Figure 3.3). Consider the upper half hemisphere with known nodal pressures

(P_1, P_2, P_3, P_4) as shown in Figure 3.3a. The pressure at any point on the surface of the sphere with coordinate (x, y, z) can be linearly related to the four known pressures:

$$P = ax + by + cz + d = \frac{P_3 - P_4}{2r}x + \frac{P_1 - \frac{P_3 + P_4}{2}}{r}y + \frac{P_2 - \frac{P_3 + P_4}{2}}{r}z + \frac{P_3 + P_4}{2}$$

[3.14.]

$$x = r\sin\phi\cos\theta, y = r\sin\phi\sin\theta, and\ z = r\cos\phi$$

Equation 3.14. can be written in the spherical coordinate system as:

$$\mathrm{P} = \frac{1}{2}[(P_3 - P_4)\sin\phi\cos\theta + (2P_1 - P_3 - P_4)\sin\phi\sin\theta + (2P_2 - P_3 - P_4)r\cos\phi + (P_3 + P_4)]$$

[3.15.]

The total fluid force F_y on the half hemisphere in the y direction is:

$$F_y = \int PdA\sin\phi\sin\theta = \int_0^\pi \int_0^{\frac{\pi}{2}} Pr^2(\sin\phi)^2\sin\theta d\phi d\theta$$

$$= r^2\left[\frac{\pi}{3}P_1 + \frac{2}{3}P_2 + \left(\frac{\pi}{12} - \frac{1}{3}\right)(P_3 + P_4)\right]$$

[3.16.]

Consider both the upper and lower hemispheres shown in Figure 3.3b; the total fluid force on a ball in the y direction is given by:

$$F_y = r^2\left\{\left[\frac{\pi}{3}P_1 + \frac{2}{3}P_2 + \left(\frac{\pi}{12} - \frac{1}{3}\right)(P_3 + P_4)\right] + \left[\frac{\pi}{3}P_1 + \frac{2}{3}P_6 + \left(\frac{\pi}{12} - \frac{1}{3}\right)(P_3 + P_4)\right]\right.$$

$$\left. - \left[\frac{\pi}{3}P_5 + \frac{2}{3}P_2 + \left(\frac{\pi}{12} - \frac{1}{3}\right)(P_3 + P_4)\right] - \left[\frac{\pi}{3}P_5 + \frac{2}{3}P_6 + \left(\frac{\pi}{12} - \frac{1}{3}\right)(P_3 + P_4)\right]\right\}$$

[3.17.]

After rearranging Equation 3.17., we obtain:

$$F_y = \frac{2}{3}\pi r^2(P_1 - P_5)$$

[3.18.]

The seepage force in the x and z directions are calculated following the same procedure used in obtaining Equation 3.18..

(a) Upper half hemisphere   (b) Whole sphere
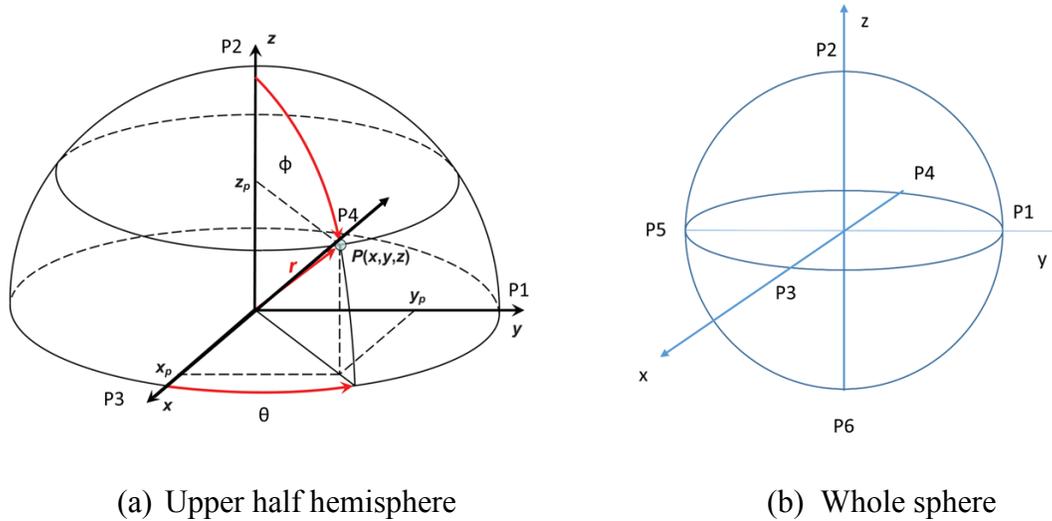
Figure 3.3: Fluid pressure calculation on a single particle in spherical coordinate system

3.2.3 Scheme for Updating Permeability

A methodology was developed to assess the variations of permeability and porosity due to deformation and sand production. The stress, strain, porosity and number of particles in each grid block are determined by inserting a "measurement sphere" at the center of the grid block. The measurement sphere is a built-in tool in PFC^{3D} to help the user to calculate quantities such as porosity, stress and strain rate in a specific measurement volume (Itasca, 2008).

To update permeability, the number of particles with centroids that lie in the specific measurement sphere is determined at the beginning and end of each time step to track particle movements. If the number of particles at the beginning is found to be equal to or smaller than the number of particles at the end of the time step, no sanding is assumed to have taken place from that volume. In this case, the permeability is updated based on volumetric strain using the modified version of the Kozeny-Carman's equation (Tortike, 1991):

51

$$k_1 = k_0 \frac{\left(1 + \frac{\varepsilon_v}{\phi_0}\right)^3}{1 + \varepsilon_v} \qquad \text{[3.19.]}$$

where k_0 is the initial permeability in the grid block, ϕ_0 is the initial porosity, ε_v is the volumetric strain calculated from the volumetric strain rate in the measurement sphere:

$$\varepsilon_v = \sum \dot{\varepsilon}_v \Delta t \qquad \text{[3.20.]}$$

where $\dot{\varepsilon}_v$ is the instantaneous strain rate determined from the velocities of all particles within the measurement sphere at the end of each DEM time step, and Δt is the DEM time step (Itasca, 2008):

$$\Delta t = \sqrt{\frac{m}{K}} \qquad \text{[3.21.]}$$

where m is the mass of the particle and K is the stiffness of the particle. The calculated DEM time step in our analysis ranged from 1×10^{-7} to 1×10^{-6} seconds.

If the number of particles in the beginning is calculated to be larger than the number of particles at the end of the time step, denoted here as N, the element permeability is updated based on the updated porosity of the element. If the porosity measured in this block is smaller than a certain threshold, denoted here as ϕ, the permeability is updated by interpolating between the original permeability and an upper-bound permeability. The upper-bound permeability was chosen to be 100 Darcies after a sensitivity work which will be presented in Section 3.4.2. Sensitivity Analysis for Model Optimization.

$$k_{update} = k_0 + (100 - k_0)\frac{\phi_1 - \phi_{full}}{T - \phi_{full}} \qquad \text{[3.22.]}$$

$$n_{update} = n_0 + (0.95 - n_0)\frac{\phi_1 - \phi_{full}}{T - \phi_{full}} \qquad [3.23.]$$

where ϕ_{full} is the porosity measured from the measurement sphere before the onset of sanding from the block, ϕ_1 is the porosity measured from measurement sphere at the end of the iteration, k_0 is the permeability at the beginning of the iterations. In this work, the porosity of the fully sanded block T was assumed to be 0.85.

If the porosity exceeds 0.85, the grid block is assumed to have completed sand production. In this case, the permeability is assigned a high value (in this study, 100 Darcy). The procedure used for updating the porosity and permeability is presented in Figure 3.4.
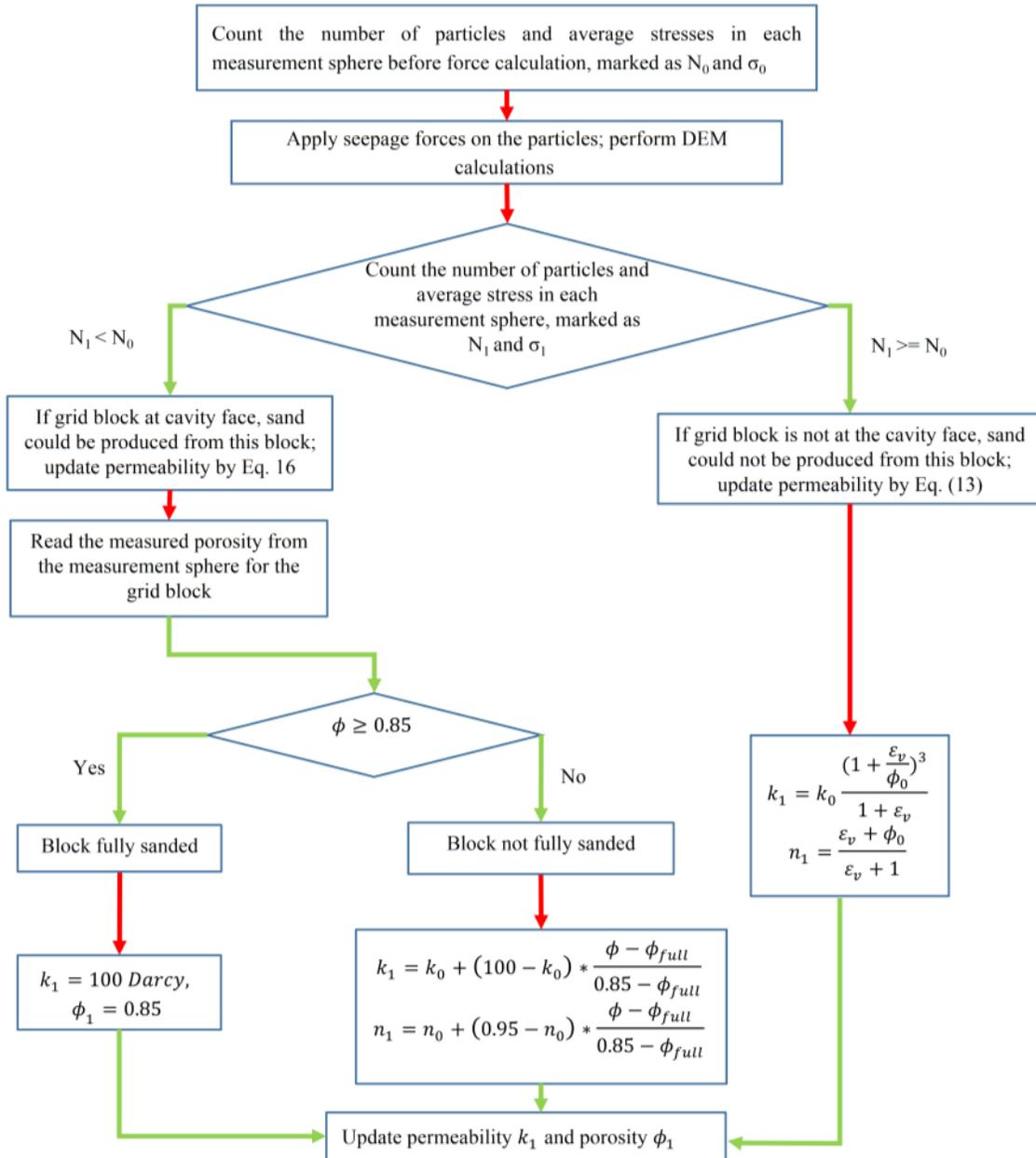
Figure 3.4: The scheme for updating permeability and porosity

3.3. Model Verification

The coupled DEM-flow model described here was verified against the results of analytical solutions proposed by Risnes et al. (1982). Details of the verification process are discussed below.

3.3.1. Analytical Solution

Risnes et al. (1982) derived analytical expressions for stress distribution around a borehole assuming axial symmetry and plane strain conditions using the Mohr-Coulomb failure criterion. Figure 3.5 shows the model geometry used by Risnes et al. (1982).
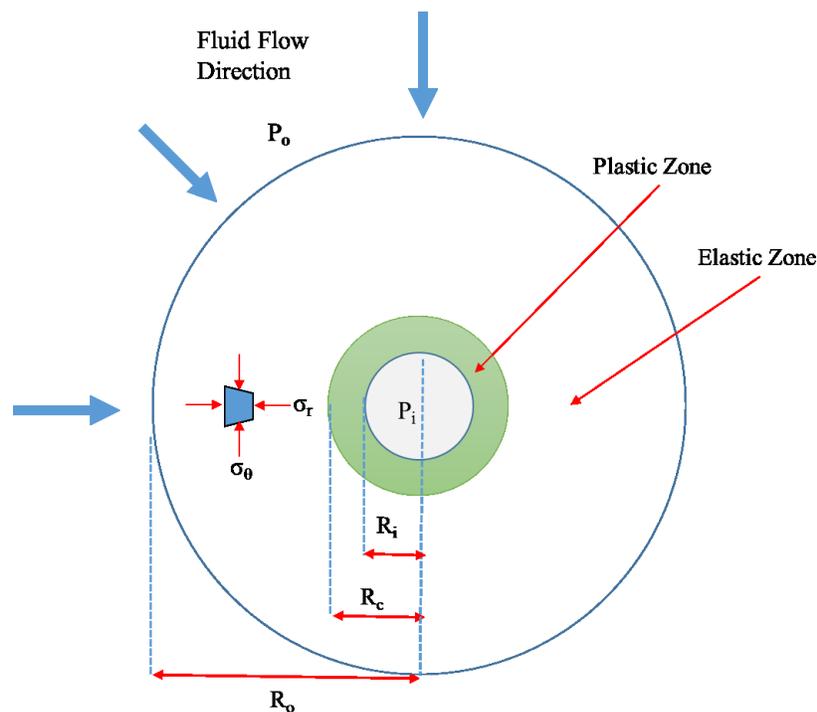
Figure 3.5: Model geometry considered by Risnes et al. (1982)

The expressions for the stresses in both the plastic and elastic zones are given in Equation 3.24. through 3.28.. Within the plastic zone, the radial and tangential total stress, σ_r and σ_θ, at a radial distance of r can be determined from Risnes et al. [6]:

55

$$\sigma_r = P_i + \frac{\mu q}{2\pi h k_c} \ln \frac{r}{R_i} + \frac{1}{\gamma}\left(2c\tan\alpha - \frac{\mu q}{2\pi h k_c}\right)\left[\left(\frac{r}{R_i}\right)^\gamma - 1\right] \qquad [3.24.]$$

$$\sigma_\theta = P_i + \frac{\mu q}{2\pi h k_c}\left(1 + \ln \frac{r}{R_i}\right) + \frac{1}{\gamma}\left(2c\tan\alpha - \frac{\mu q}{2\pi h k_c}\right)\left[(\gamma + 1)\left(\frac{r}{R_i}\right)^\gamma - 1\right] \qquad [3.25.]$$

where P_i and P_0 are the fluid pressures at the inner and outer cylindrical boundaries, c is the cohesion of the material, α is the failure angle which is equal to $\pi/4 + \phi/2$, ϕ is the internal friction angle, $\gamma = \tan^2\alpha - 1$, μ is the fluid viscosity, k_c is the permeability of the material in the plastic zone, and q is the fluid flow rate calculated from:

$$q = \frac{2\pi k h (P_0 - P_i)}{\mu \ln\left(\frac{R_0}{R_i}\right)} \qquad [3.26.]$$

where h is the height of the model.

Radial and tangential total stresses in the elastic zone are calculated from Risnes et al. (1982):

$$\sigma_r = \sigma_{r0} + (\sigma_{r0} - \sigma_{rc})\frac{R_c^2}{R_0^2 - R_c^2}\left[1 - \left(\frac{R_0}{r}\right)^2\right] - (P_0 - P_c)\frac{1 - 2\upsilon}{2(1 - \upsilon)}\beta\left\{\frac{R_c^2}{R_0^2 - R_c^2}\left[1 - \left(\frac{R_0}{r}\right)^2\right] + \frac{\ln\frac{R_0}{r}}{\ln\frac{R_0}{R_c}}\right\} \qquad [3.27.]$$

$$\sigma_\theta = \sigma_{r0} + (\sigma_{r0} - \sigma_{rc})\frac{R_c^2}{R_0^2 - R_c^2}\left[1 + \left(\frac{R_0}{r}\right)^2\right] - (P_0 - P_c)\frac{1 - 2\upsilon}{2(1 - \upsilon)}\beta\left\{\frac{R_c^2}{R_0^2 - R_c^2}\left[1 + \left(\frac{R_0}{r}\right)^2\right] + \frac{\ln\frac{R_0}{r} - 1}{\ln\frac{R_0}{R_c}}\right\} \qquad [3.28.]$$

where σ_{ro} is the radial stress at the outer boundary, σ_{rc} and P_c are the radial total stress and the fluid pressure at the plastic-elastic boundary ($r = R_c$), υ is the material Poisson's ratio and β is the coefficient of rock compressibility which is equal to $1 - C_r/C_b$, C_r is the rock matrix compressibility, and C_b is the rock bulk compressibility.

3.3.2. Input Parameters

We used Castlegate sandstone properties in the analytical and numerical models for a Thick-Walled Cylindrical (TWC) sample with the inner and outer radius of 8 mm and 80 mm, respectively, with a sample height of 15 mm. Castlegate sandstone is a weak, high-porosity sandstone with low clay content, which has been used in triaxial testing (e.g., Bradford and cook, 1994). Rahmati (2013) calibrated the micro properties of Castlegate sandstone and performed DEM simulation of Thick Walled Cylinder samples to study borehole breakout mechanisms (Rahmati et al., 2013b). The unconfined compressive strength is around 20 MPa; the porosity is 0.25 and the permeability is 500 to 1000 mD (Rahmati, 2013). Cheung (2010) reported that the cement content for the Castlegate sandstones is equal to 6.4% by mass. Rahmati (2013) calibrated the macro properties of Castigate sandstone from laboratory triaxial tests. Cohesion, friction angle, and elastic properties were determined from triaxial tests on Castlegate sandstone. Young's modulus was based on a value calculated at 50% of the peak stress as recommended by Schanz et al. (1999). Poisson's ratio was averaged at different effective confining stresses. The macro parameters for the numerical model are summarized in Table 3.1.

Table 3.1: Analytical input data for flow analysis and Castlegate sandstone properties

Sample Dimension and Fluid Properties		Rock Properties (Rahmati, 2013)	
Outer boundary pressure P_o (MPa)	Variable	Possion's ratio ν	0.2
Inner boundary pressure P_i (MPa)	0	$\beta = 1 - C_r / C_b$	1
Sample thickness h (cm)	1.5	Cohesion C (MPa)	4.3
Sample inner radius R_i (cm)	0.8	Friction angle ϕ (deg)	46.5
Sample outer radius R_o (cm)	8	$\alpha = \frac{\pi}{4} + \frac{\phi}{2}$ (deg)	61.5
Water viscosity μ (cp)	1	Elastic zone permeability K_e (Darcy)	0.6
Fluid flow rate q (cm^3/s)	By case	Plastic zone permeability K_c (Darcy)	0.6

The DEM model was generated using two horizontal and one cylindrical rigid wall with a radius of 80 mm and height of 15 mm (Figure 3.6). Table 3.2 presents the micro-parameters of DEM particles calibrated using triaxial test results (Rahmati et al., 2013c). A constant radial stress of 60 MPa was applied at the outer boundary by moving the outer cylindrical wall using a servo control algorithm while the top and the base platens were fixed in all directions. An inner hole of 8 mm radius was then drilled by removing particles. An initial calculation was carried out to eliminate unbalanced forces at the contact. The calculation continued until the ratio of average unbalanced force to the average contact forces converged to a value of less than 1%.
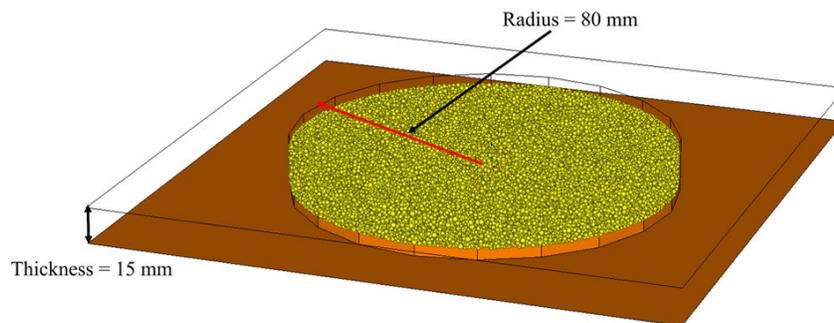
Figure 3.6: DEM model for the TWC test

Table 3.2: Micro properties of Castlegate sandstone for DEM simulations (Rahmati, 2013)

Particle properties		Parallel bond properties	
Particle Yong's modulus E_p (GPa)	7	Parallel bond Yong's modulus E_{pb} (GPa)	20
Particle normal to shear stiffness ratio $(K_S/K_N)_p$	0.2	Parallel bond normal to shear stiffness ratio $(K_S/K_N)_{pb}$	0.2
Partial friction coefficient μ	1.5	Parallel bond normal strength $S_{N\,pb}$ (MPa)	400
Particle radius R_p (mm)	0.4 to 1.3	Parallel bond shear strength $S_{S\,pb}$ (MPa)	900
Particle density ρ (kg/m³)	2,650	Degree of bonding λ	0.3

The fluid model was introduced by dividing the domain into 324 flow elements with 9 sections in the radial direction, 18 sections in the circumferential direction, and 2 in the vertical direction. Figure 3.7 shows the sample geometry and the flow mesh.
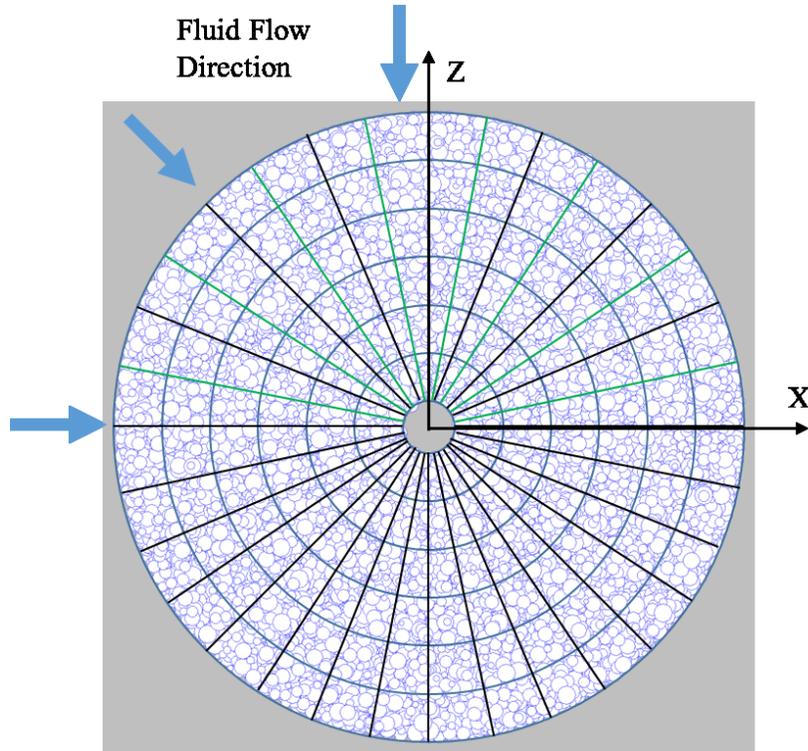
(a) Top plan view (x-z plan)
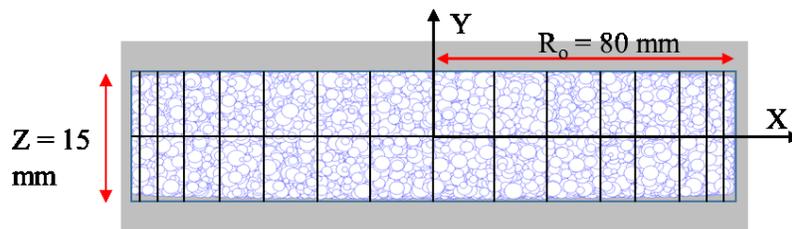
(a) Side plan view (x-y plan)

Figure 3.7: DEM model of the TWC test overlain by grid blocks for flow analysis in cylindrical coordinate system

Water was injected from the outer cylindrical boundary into the specimen using the flow boundary conditions shown in Figure 3.7. Since sanding is not considered in the analytical model, the fluid pressure at the outer boundary was kept below a critical level to avoid any sand mobilization toward the center hole. Nodal pressures in the flow model were transferred to the DEM model

where the pressures were converted to seepage forces and applied on each particle. The DEM calculations were then performed until the solutions converged within a small tolerance.

3.3.3. Verification Results of the Analysis

The radial and tangential stresses in the specimens were determined by calculating the average stress in the measurement spheres. Comparisons of the numerical and analytical results for tangential and radial stress along the radial direction are shown in Figure 3.8 and Figure 3.9.

The width of the plastic zone can be considered to extend from the face of the borehole to the location of maximum tangential stress. Figure 3.8 shows the radial and tangential stress profiles at a confining stress of 60 MPa without fluid flow. It is observed that a plastic zone has already been developed around the hole even when there is no fluid flow. However, with fluid flow, the plastic zone further expands in both the numerical and analytical models (Figure 3.9). The tangential and radial stresses of both analytical and numerical solutions approach the boundary stress of 60 MPa at the outer boundary. The difference between the peak values for the analytical and numerical tangential stresses can partly be attributed to the averaging procedure in calculating stresses in the numerical model which has a smoothing effect on the stress calculations (Climent et al., 2014).
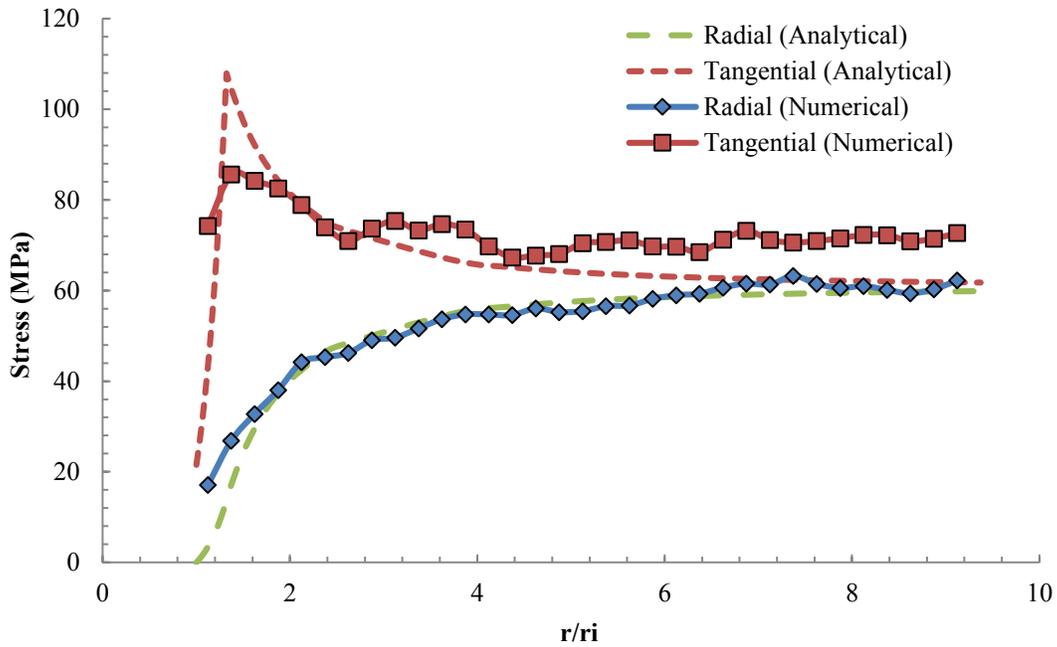
Figure 3.8: Comparison between numerical and analytical results for tangential and radial stress in the radial direction for the case without fluid flow
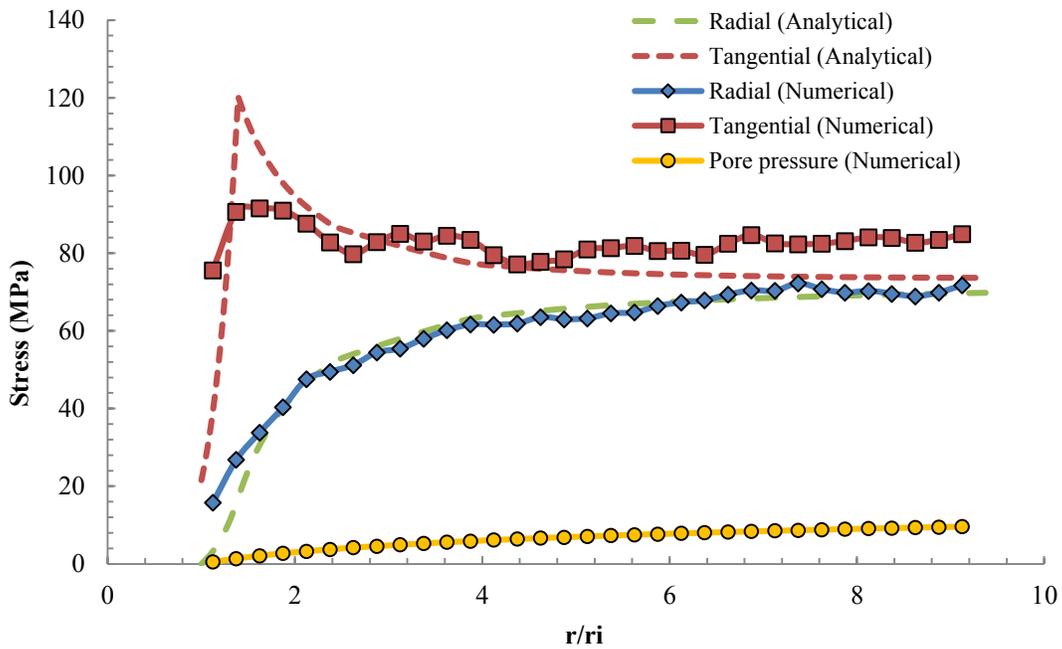
Figure 3.9: Comparison between numerical and analytical results for total tangential and radial stress in the radial direction for the case with fluid flow and 10 MPa for outer boundary fluid pressure

3.4. Sand production simulation

In this section, we describe the simulation of a synthetic sanding test using the DEM model. We first specify the model geometry and boundary conditions. Next, we describe the results of a series of sensitivity analysis to optimize the number of DEM steps that need to be performed within each numerical iteration.

3.4.1. Model Geometry and Boundary Conditions

The DEM model was generated in a rectangular box with length, width and depth equal to 120 mm, 120mm, and 15 mm, respectively. The domain is bounded by six frictionless rigid walls (Figure 3.10). The model creation procedure followed the same way as in the verification model. Parallel bonds were randomly imposed on 30% of the contacts after the material generation stage. The bond radius multiplier was varied randomly between 0 and 1 (Rahmati, 2013), based on the observations from Scanning Electron Microscope (SEM) images of Castlegate sandstone (Cheung, 2010). Based on the SEM image of Castlegate sandstone in Figure 3.11, it is evident that not every grain-grain contact in the Castelgate sandstone is cemented. Contact A is a cemented, Contact B is not cemented, and contact C has broken cementation. Meanwhile, the degree of cementation varies at the contacts. Table 3.2 presents the DEM micro-properties for this model.

DEM simulations started with the sample compaction by applying three perpendicular and unequal stresses using a servo control algorithm (Itasca, 2008). The vertical borehole with 8 mm radius was drilled by gradually decreasing the grain stiffness inside the borehole to zero followed by removing the grains inside the borehole. Initial analysis was carried out until the average unbalanced forces divided by the average contact forces was smaller than 1%.
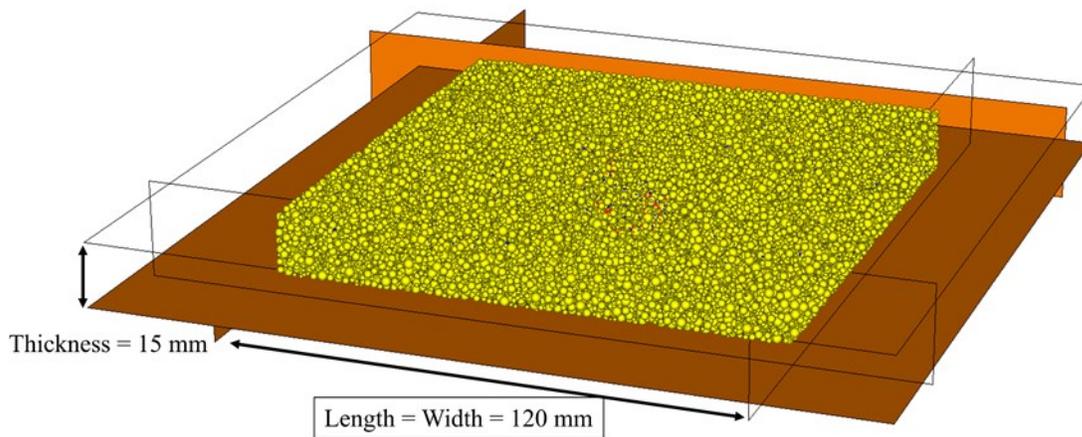
Figure 3.10: DEM sanding block model
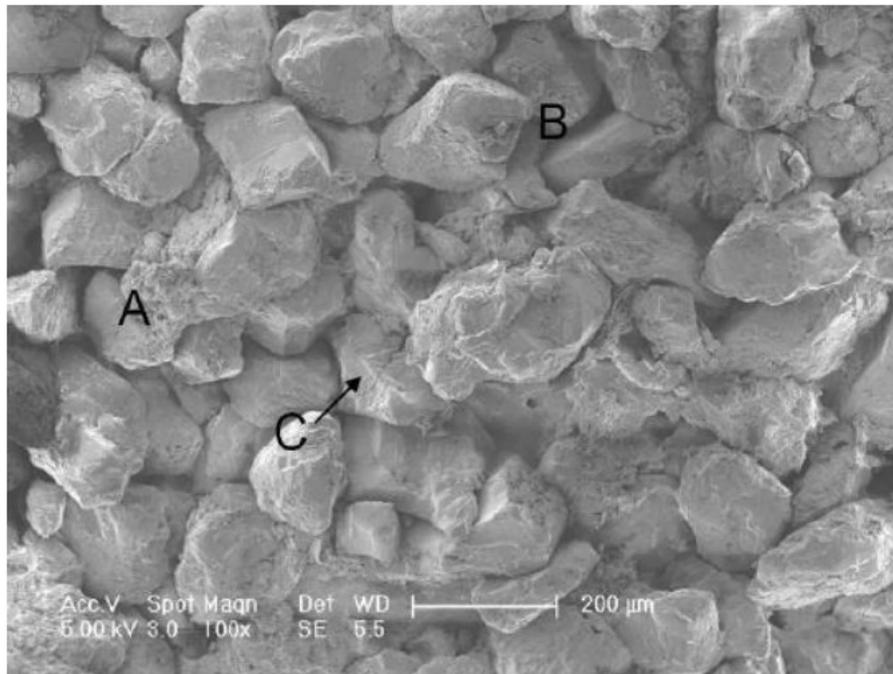
Figure 3.11: The SEM image for the Castlegate sandstone (Alvarado, 2007)

The fluid flow model was linked to the DEM model. The flow model has 324 grid blocks with nine sections in the radial direction, 18 sections in circumferential directions, and two in the vertical direction, as shown in Figure 3.12.
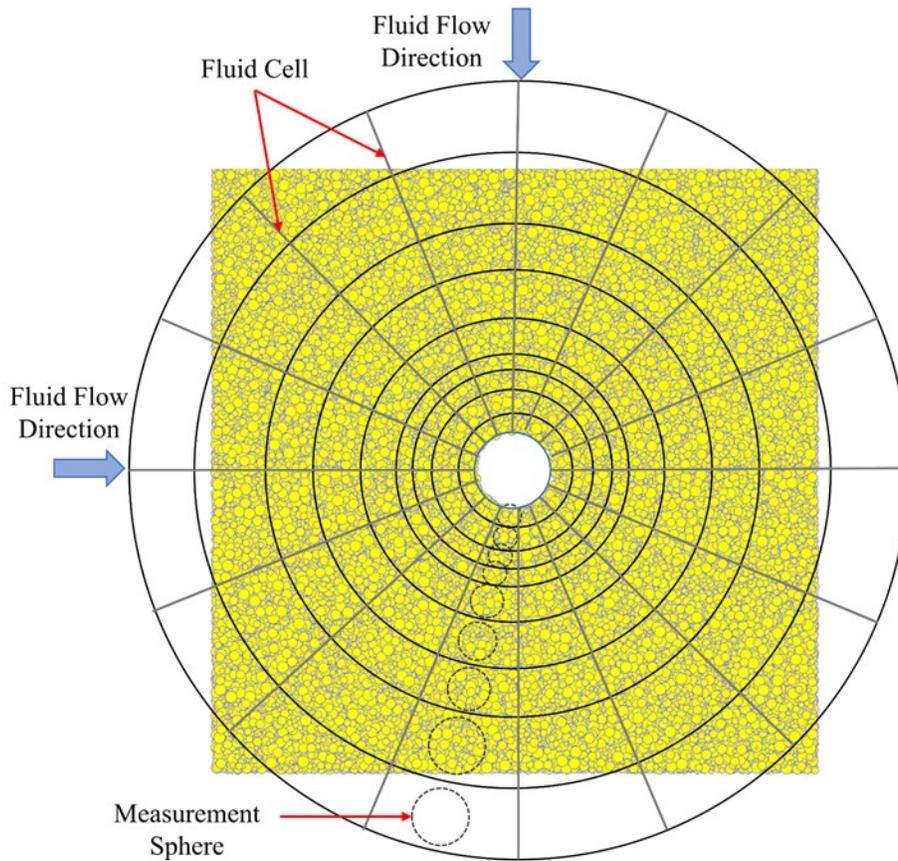
Figure 3.12: Block sample overlain by grid blocks in cylindrical coordinate system

In linking fluid flow-DEM calculations, convergence was considered to be achieved when the number of particles in the measurement spheres, as well as permeability and porosity in each grid block, had converged within a tolerance of 5%.

3.4.2. Sensitivity Analysis for Model Optimization

In order to determine the effects of various parameters in the model, a sensitivity study was performed to optimize the size of the measurement sphere, the permeability of the sanding zone used in Equation 3.22, and also the number of DEM steps required in each numerical iteration. A uniform far field effective stress of 60 MPa was applied which was enough to induce breakage of

bonds near the hole before the application of fluid flow. An outer boundary fluid pressure of 0.5 MPa was applied resulting in the flow rate of 11.53 cm^3/sec in wellbore surface.

The sanding response was studied for different DEM steps in each DEM-fluid flow iteration. Figure 3.13 shows the effects on sanding due to the number of DEM steps. The solutions seemingly are converging at about 10,000 DEM steps. However, the total produced sand mass for different number of DEM steps was the same. Therefore, we chose 10,000 DEM steps for each iteration in all subsequent analyses.
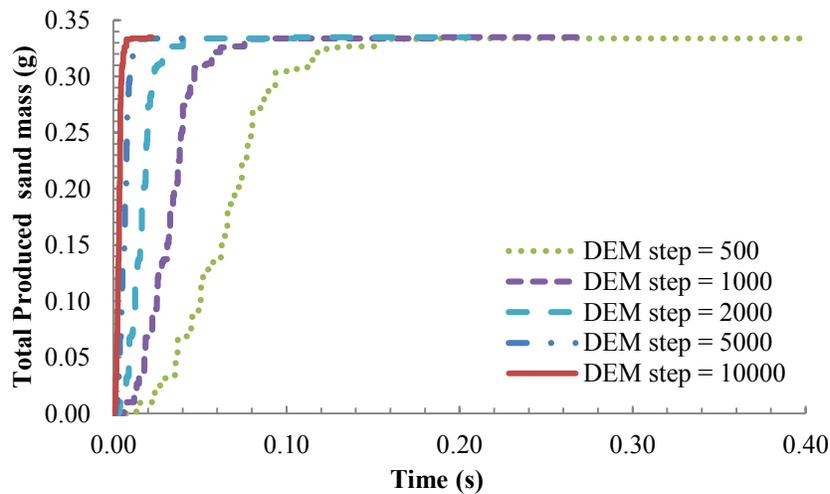
Figure 3.13: Produced sand mass for different number of DEM steps in each DEM-fluid flow iteration

A sensitivity analysis was performed to study the effect of the assigned permeability for the sanded zone in Equation 3.22. A fluid pressure of 0.1 MPa was applied at the outer boundary with an in situ effective stress of 60 MPa. The permeability assigned to the fully produced cell was fixed during each test. Figure 3.14 shows that the sanding response is not sensitive to the permeability of the produced zone for k values greater than 50 Darcy. Therefore, we assigned a permeability of 100 Darcy in all subsequent analyses.
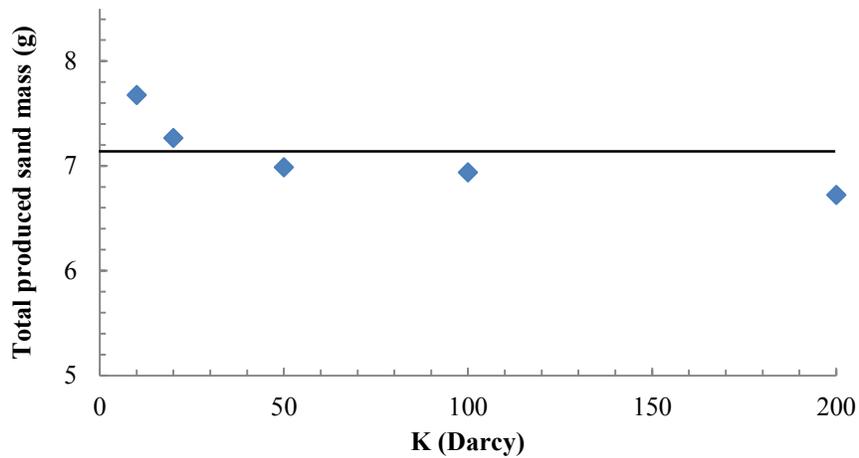
Figure 3.14: Cumulative sanding for different values of permeability for the produced zone

Another study was performed to study the effect of the size of the measurement sphere on the results. Significant errors in the calculated stress, strain, and porosity result when the measurement sphere includes only four or less particles (Itasca, 2008). On the other hand, inaccurate permeability calculations result when large measurement sphere sizes that cover more than one flow grid block are selected. We chose the size of the grid block in such a way to include a minimum six particles. The final size of the measurement sphere was chosen to be 1.6 times the length of the grid block, so that it would circumscribe the flow grid blocks and include a representative number of particles in the sphere.

3.4.3. Effect of Maximum and Minimum Horizontal Effective Stress and Pore Pressure on Rock Degradation and Sanding

In this section we study the effect of boundary effective stress and pressure on sandstone degradation and sanding. Two cases were considered: (1) the horizontal effective stresses were equal to 60 MPa, (2) maximum and minimum horizontal stresses were equal to 60 and 30 MPa,

respectively. In both cases, the fluid pressure at the outer boundary was kept constant at 10 MPa. The DEM – fluid flow analysis was cycled until 0.03 sec.

A map of broken bonds of a horizontal section are shown in Figure 3.15, for different boundary stress and pressure cases after 0.12 sec. Micro-failure at the contacts is represented by red and blue for bonds failed in tension and shear, respectively. Figure 3.15a shows uniform breakout for the case with uniform boundary stress without fluid flow. Figure 3.15b shows V-shaped breakout for the same case but with uneven boundary stresses. Some sand particles are observed to be produced from the breakout zone by seepage forces after the application of fluid flow.

The analysis of breakout zone for the dry case (Figure 3.15a) showed that even the in situ stress is symmetric, the breakout zone is not a perfect circle around the borehole. This is consistent with what we expected and also past research by using DEM in dry case (Rahmati, 2013). If we performed the analysis in a homogeneous continuum medium with symmetric loading, we would expect a symmetric failure zone around the hole. However, our DEM medium is not perfectly homogeneous with the inter-granular bonds scattered in the medium in a random fashion only in 30 percent of the grain contacts. Hence, the failure onset (debonding of grains) occurs at slightly weaker zones (due perhaps to slightly fewer bonds), which makes the zone even weaker, hence, further propagation of debonding in the zone and asymmetric shape of the debobded cloud.
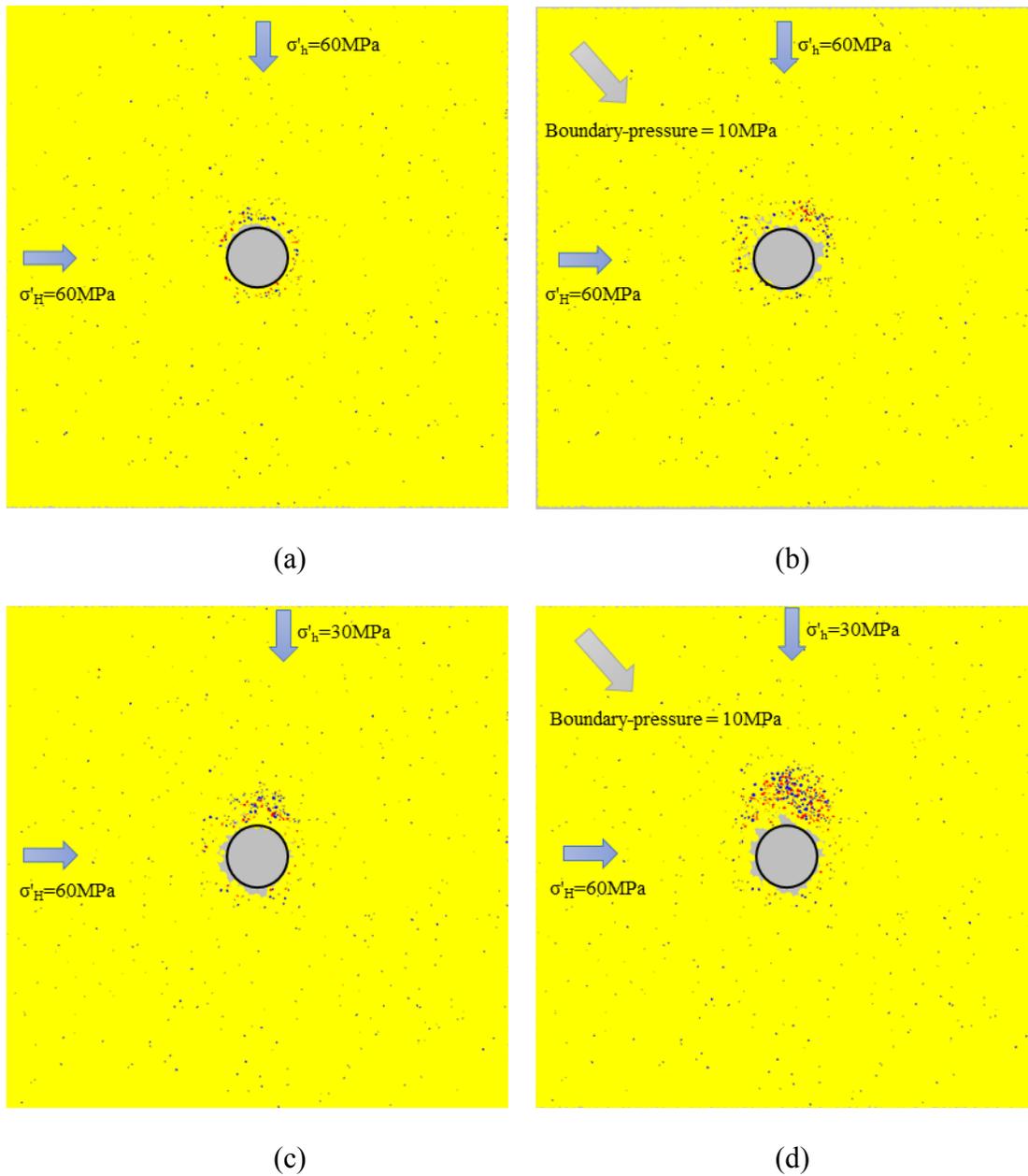
Figure 3.15: Cross section of borehole breakout and sanding zone for different far-field stress. (a) isotropic far field stress case, before the application of fluid flow, (b) after the application of fluid flow with pore pressure = 10 MPa, at time = 0.03 sec, (c) anisotropic far field stress case, before the application of fluid flow, (d) after the application of fluid flow with pore pressure = 10 MPa, at time = 0.03 sec.

Figure 3.16 compares the maximum thickness of the plastic zone for the dry case based on the DEM solutions (Figure 3.15 a and c) and the analytical solutions in dash line. The analytical

formulation of isotropic case is presented by Risnes et al (1982), and the analytical formulation of anisotropic case is presented by Fjar (2008). The macro properties of Castlegate sandstone used in analytical solution is listed in Table 3.1. For 60 MPa isotropic effective stress case, analytical solutions result in 2.6 mm for the maximum thickness of the plastic zone while DEM measurement from Figure 3.15a indicate 3 mm for the maximum plastic thickness in average. For the case with σ'_h= 30 MPa, DEM and analytical solution result in 8 mm and 7 mm for the thickness of the plastic zone, respectively. Results indicate a reasonable agreement between the DEM and analytical solutions before introducing the fluid flow. Based on Figure 3.15, the plastic zone further expands once the pressure drawdown is applied.

(a)   (b)
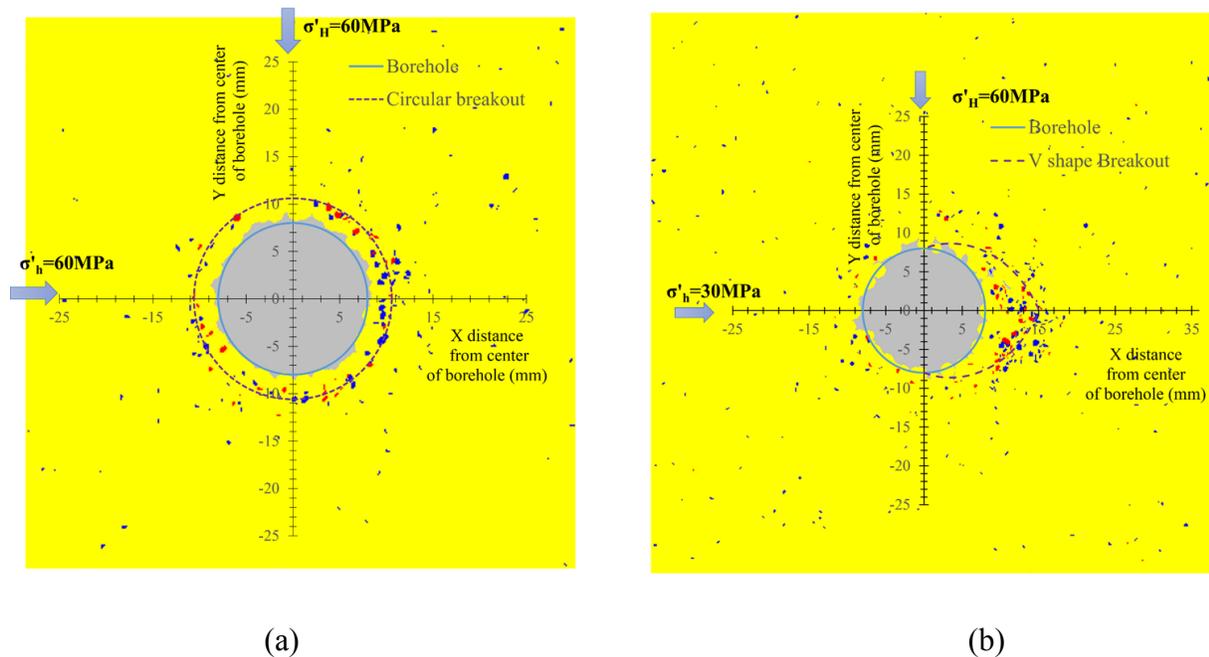
Figure 3.16: The analytical solution of plastic zone for the dry case of (a) isotropic boundary effective stress (b) anisotropic boundary effective stress.

Figure 3.17 shows the effect of the minor principle stress on the produced sand. As expected, larger amount of sand is produced for the case with anisotropic boundary effective stress than the

isotropic counterpart. However, sanding is observed to be only slightly different for the vastly different minimum far field effective stresses.
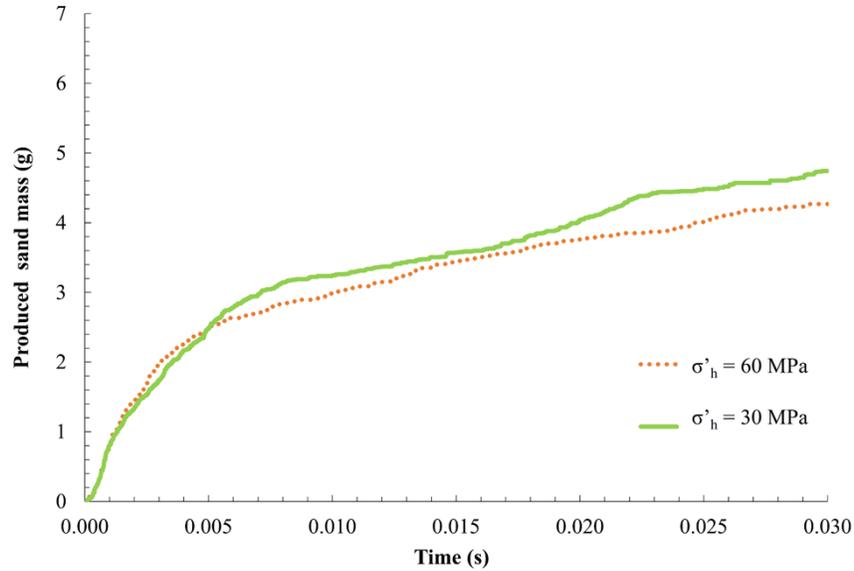
Figure 3.17: Cumulative sanding for different far-field stress conditions

Next, both boundary effective stresses were kept constant at 50 MPa in a series of analysis with varying outer boundary fluid pressure from 0.1 MPa to 15 MPa. Figure 3.18 shows the high-rate sanding at the beginning of the simulation leading to stabilized sanding at different times. The total amount of sand produced and steady-state time increase significantly for outer boundary pressures larger than 10 MPa. We notice a significant jump in the amount of produced sand when the boundary pressure increases from 10 to 15 MPa. The reason is mainly due to the contribution of the seepage forces in additional sandstone degradation through more and faster removal of degraded materials.
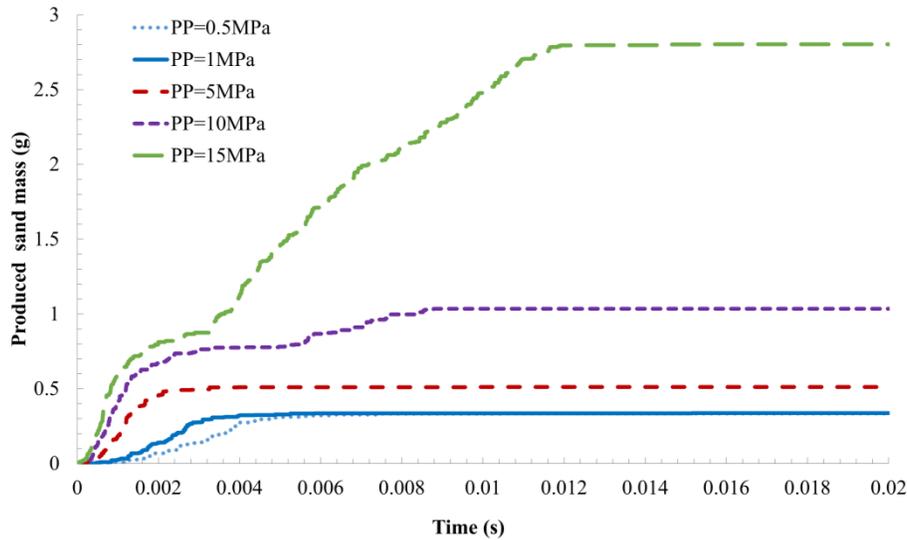
Figure 3.18: Sand production for different boundary pressures

3.4.4. Simulation of Step-Rate Sanding Test on Block Sample

We simulated a synthetic sanding test on a hollow cylinder sample using the model presented in Figure 3.10 and Figure 3.12 and material micro properties presented in Table 3.2. In the simulations, the outer boundary effective stress was incrementally increased with the step-rate increase of the fluid pressure within each boundary stress increment (Figure 3.19). The analysis for each step continued until the steady-state condition was reached (sanding rate is equal to zero at this stage). Figure 3.19 indicates the onset of sanding at the outer boundary effective stress of 30 MPa. Cumulative sand production shows a gradual increase for each increase in the boundary effective stress or pressure. However, sanding stabilizes within each increment. Massive sanding occurs when the boundary effective stress and pressure reach 58 and 20 MPa, respectively.
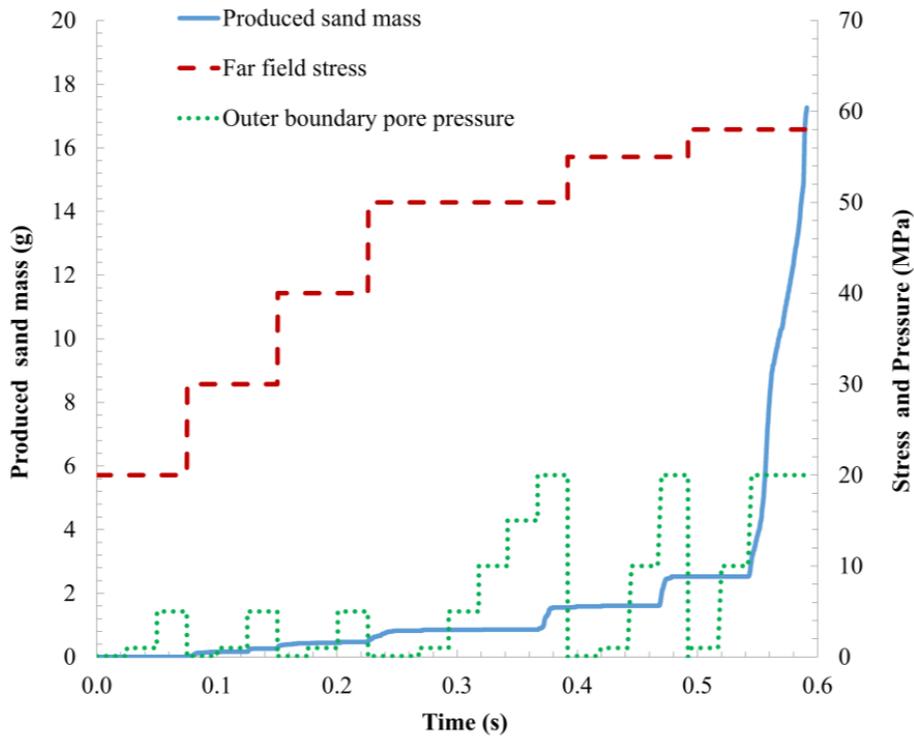
Figure 3.19: Sanding response under incrementally increasing boundary stress and pressure for final boundary stress of 58 MPa

To further examine the role of fluid flow, we repeated the same analysis but changed the final modelling step (Figure 3.20). The last loading step in Figure 3.20 shows the boundary effective stress equal to 65 MPa with lower boundary pressure of 1 MPa. Despite significantly higher boundary effective stress, we can see much less sanding compared to the last step in Figure 3.19. The large boundary pressures in Figure 3.19 result in larger seepage forces leading to further removal of detached sand particles, redistribution of contact forces, and propagation of the degraded zone.
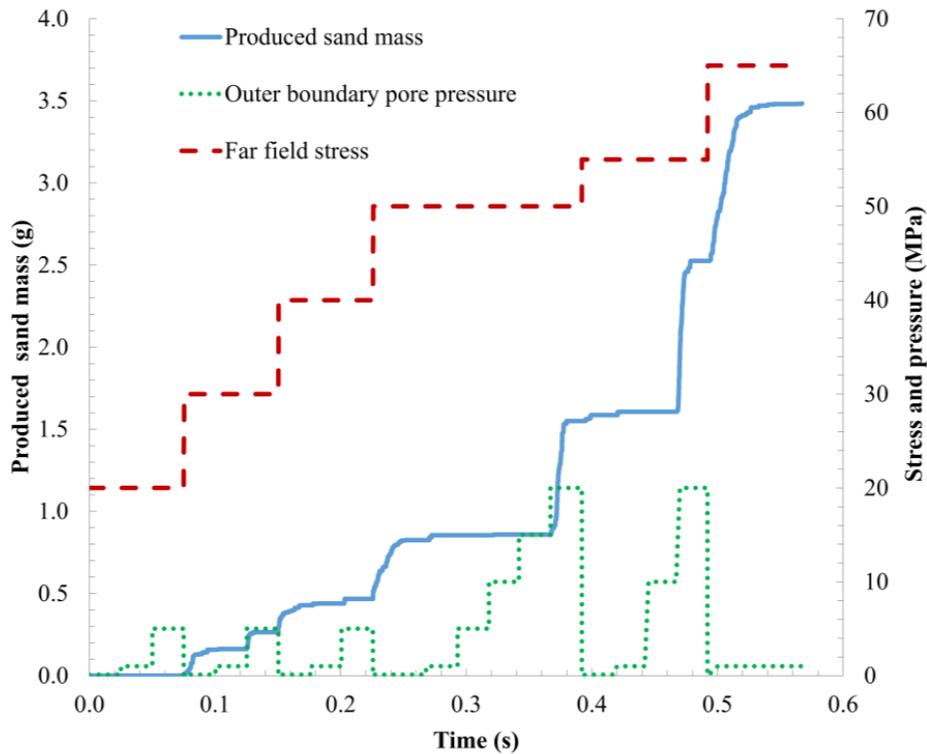
Figure 3.20: Sanding response under incrementally increasing boundary stress and pressure for final boundary stress of 65 MPa

Figure 3.21a shows little degradation at a boundary effective stress of 50 MPa and boundary pressure of 20 MPa. Figure 3.21b shows a larger size of the degraded zone at the boundary stress of 58 MPa and boundary pressure of 20 MPa. The degraded zone is significantly smaller at the higher boundary stress of 65 MPa and low boundary pressure of 1 MPa (Figure 3.21c). However, the degraded zone is significantly enlarged when the outer boundary pore pressure reaches 20 MPa. The reason for the above observation is that the additional degradation is due to seepage forces being strong enough to remove more particles leading to stress redistribution thus more degradation is observed. When the outer boundary pore pressure is small, say 1 MPa, the fluid force near the wellbore face is not large enough to break the bond between the particles. The case with 65 MPa's confining stress shows a higher tangential stress resulting in higher frictional

74

resistance, thus, less sand production at the same levels of boundary pressure. This may explain lower sand production for the case with 65 MPa confining stress in the period between 0.52 to 0.6 s. The asymmetric plastic zone shown in Figure 20b is due to the expansion of the breakout due to the fluid seepage. The asymmetric breakout and expansion of plastic zone is also observed in past research works (Li et al., 2006; Climent et al., 2013) for cases with fluid flow.
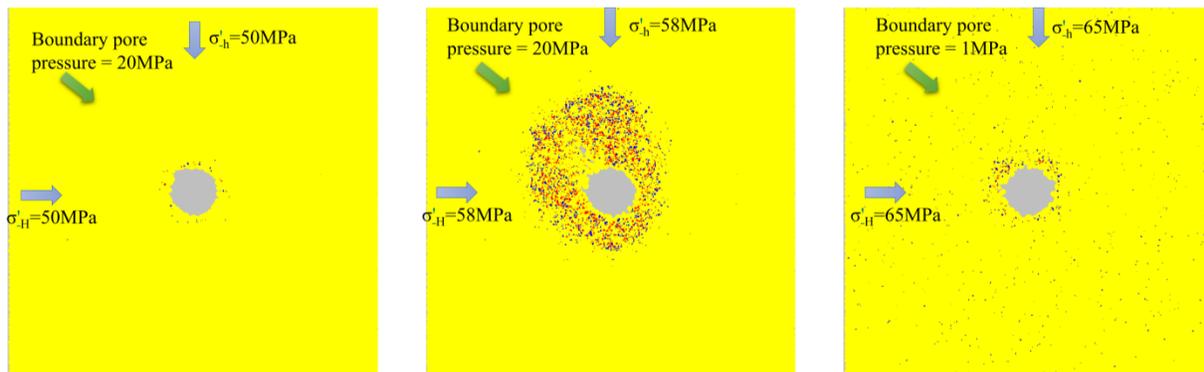
Figure 3.21: Cross section of failure shape around wellbore. (a) Far field effective stress = 50 MPa, outer boundary pressure = 20 MPa. (b) Far field effective stress = 58 MPa, outer boundary pressure = 20 MPa. (c) Far field effective stress = 65 MPa, Outer boundary pressure = 1 MPa

3.4.5. Simulation of Step-Rate Sanding Test on Hollow Cylinder Sample

A synthetic sanding test on hollow cylinder sample by using the model specifications presented in Figure 3.6 and Figure 3.7 and the material micro parameters presented in Table 3.2 was simulated. In the simulation, the effect of far field boundary stress to the sand production was analyzed in the simulation. Two type of tests were conducted, one with low confining far field stress of 40 MPa, and another with the high confining stress of 60 MPa. During the simulation, the far field stress was kept as constant, and the pore pressures at the outer boundary was increased in a step-wise manner as shown in Figure 3.22.

For the low confining stress case, the loading was started by applying uniform boundary effective stresses of 40 MPa and boundary pressure of 1 MPa. The DEM-fluid flow simulation was then cycled until the steady-state condition was reached. The outer boundary pore pressure was then increased to the next level of 10 MPa while the far field stress was still maintained at the same level of 40 MPa. Figure 3.22a indicated the onset of sanding at the boundary pore pressure of 1 MPa followed by a steady sand production (zero sanding rates) until the next increment of boundary pore pressure. Cumulative sand production is observed when the boundary pore pressure reached to 40 MPa.

The numerical procedure of high confining stress case (60 MPa) is the same as low confining stress case (40 MPa). It is observed that the cumulative sand production happened when the boundary pore pressure reached 55 MPa. By comparing Figure 3.22 and Figure 3.23, it is found that high confining pressure case produced more sand than low confining pressure one with the same outer boundary pore pressure level.
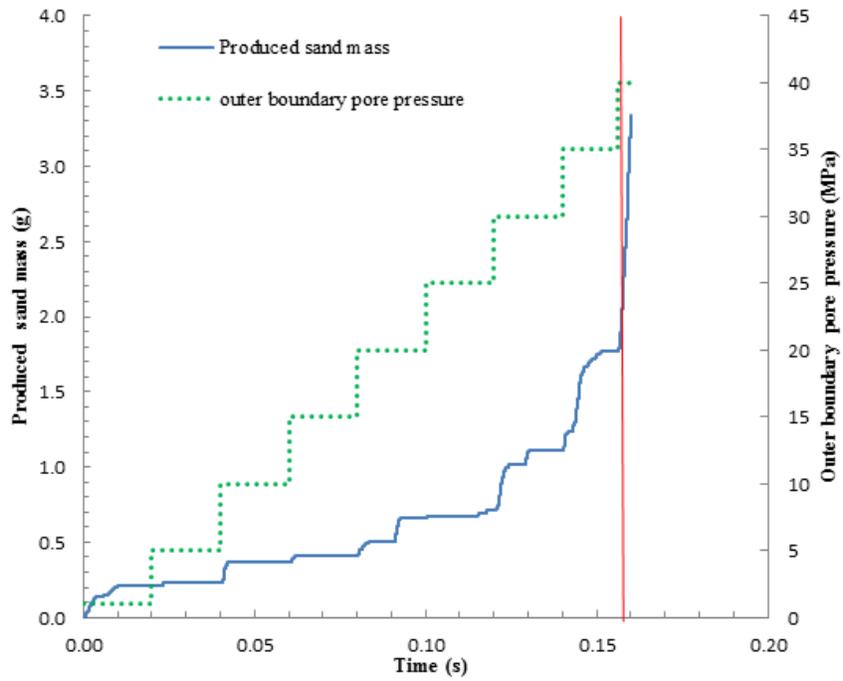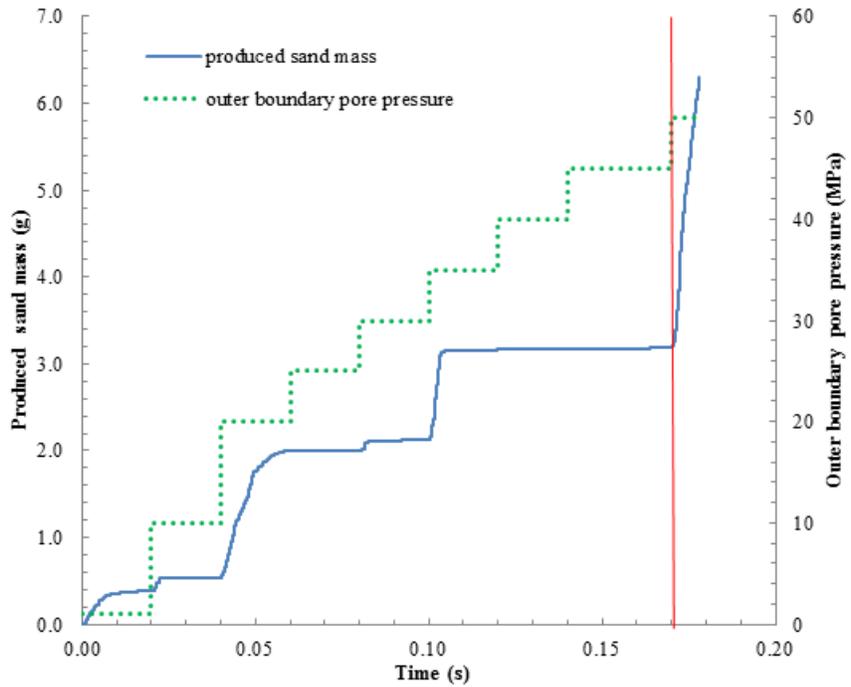
Figure 3.22: Sand production response under incrementally increasing outer boundary pressure conditions: (a) Confining effective stress of 40 MPa (b) Confining effective stress of 60 MPa
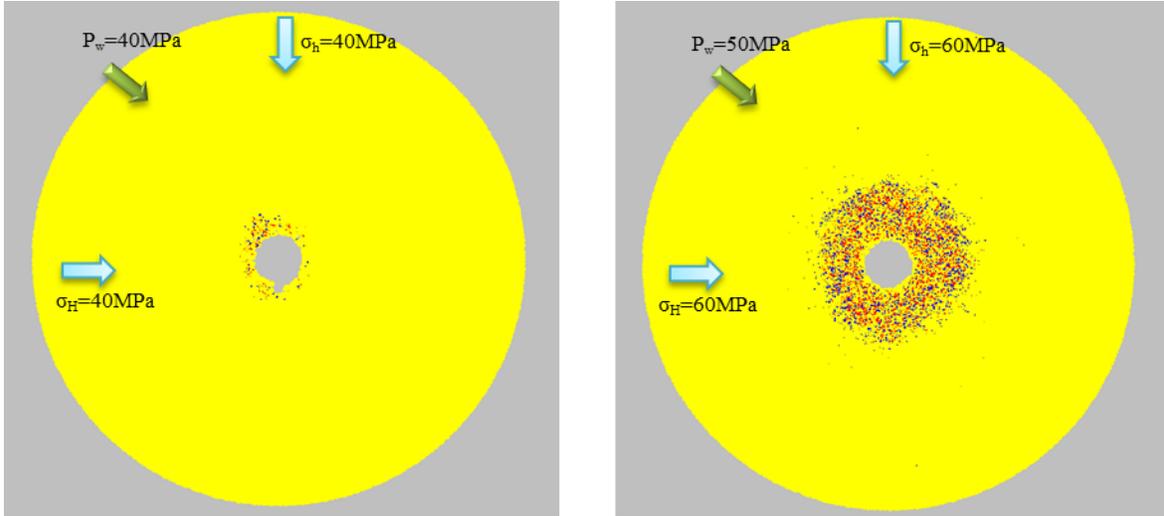
Figure 3.23: The cross sectional view of failure shape of wellbore when reaching cumulative sand production (a) Far field effective stress = 40 MPa, outer boundary pressure = 40 MPa. (b) Far field effective stress = 60 MPa, outer boundary pressure = 50 MPa.

The radial and tangential stress profiles developed in the specimens have been calculated by using the same procedures in the verification process. A relative higher tangential stress is found in 60 MPa's confining stress case, which indicates that the friction force in high confining pressure case is more than in low confining pressure case. The friction force will prevent sand production when applying same levels of outer boundary stress. It may explain there is not too many sand production in 60 MPa's confining stress case between time 0.11 to 0.17 s, even the outer boundary pore pressure is increasing gradually.

3.5. Conclusion

A sand production model has been presented by coupling DEM model with a fluid flow model. The model has been checked with analytical solutions and applied to examine sanding process in synthetic sanding tests. The model accounts for permeability and porosity changes due to solid deformation and sand production. Some simulation results are summarized below:

1. A circular breakout was found for the case of isotropic boundary stress with $\sigma_H = \sigma_h = 60$ MPa. The breakout morphology changes to V-shaped breakout with unequal boundary stresses when $\sigma_H = 60$ MPa and $\sigma_h = 30$ MPa .

2. Larger sanding occurs with with unequal boundary stresses when $\sigma_H = 60$ MPa and $\sigma_h = 30$ MPa, compared to the case with isotropic boundary stress with $\sigma_H = \sigma_h = 60$ MPa.

3. Sand production occurs from degraded zones where most bond failures has occurred. Sand production from V-shaped breakout changes the wellbore shape from circle to ellipse.

4. The boundary stress plays a major role in sand production through sandstone degradation. However, less sanding occurs at higher boundary effective stress but considerably lower boundary pressure due to the ineffective removal of the degraded materials for weaker seepage forces. For high boundary pressure, seepage force plays a major role in the sand production as it removes degraded materials, results in stress redistribution which can then contribute to further degradation and sanding. More sand production occurs at lower far-field stress (in this case, 58 MPa) but higher boundary pressure (in this case, 20 MPa).

Chapter 4. Solid Deformation Pressure Coupling[2]

4.1. Introduction and Background

Another important factor affecting stability of wellbore is the generation and dissipation of excess pore pressure in the reservoir during drilling as well as during oil production due to the deformation of the formation. The accumulation of excess pore water pressure is caused by the change of pore volume and insufficient dissipation of pore water pressure. The changes of the pore volume are caused by soil/rock deformation due to changes in the mechanical boundary conditions. Examples of changes in mechanical boundary conditions include borehole drilling, and shear deformation and localization of the rock. The increase of excess pore pressure will cause displacement and deformation of the solid particles and void space, and the movement of the solid particles will change the void space that is occupied by the fluid. At the laboratory scale, the conditions relate to undrained or partially drained cases in triaxial tests. In field cases, undrained deformation occurs in liquefaction of soil during an earthquake. During undrained deformation, pore space connectivity and pore space deformation in a porous medium results in uncertainty of the fluid force applied on individual particle. Therefore, the SPF coupling method developed in the last chapter is not able to simulate pore pressure induced force. A new method is needed to provide more accurate simulation of the effect of pore pressure on particles.

Cook (2001) developed a coupled numerical method for the direct simulation of particle-fluid systems. The fluid flow was solved using lattice-Boltzmann (LB) method, which can accurately

---

reproduce Navier-Stokes equations. In LB model, fluid is represented as packets of mass that move on a regular lattice, defined with the appropriate boundary conditions. Collision and redistribution of fluid packets occur at the lattice nodes according to relationships that conserve mass and momentum. The coupling of LB and DEM is accomplished through a moving solid boundary condition. An immersed moving boundary scheme proposed by Noble and Torczynski (1998) was adopted. The fluid-induced force was calculated by summing up the momentum tum transfer that occurs over all nodes covered by the solid element. Cook et al. (2004) validated the developed method through a comparison of simulation results with the analytical solution of cylindrical Couette flow. The results show the accurate computation of fluid flow and particle forcing. They also performed the erosion simulation of sanding near well bore; the results produced physically realistic behavior. Han (2012) used (lattice-Boltzmann Discrete Element Method) LBM-DEM coupling to simulate the sand arch test. The collapse and re-forming of sand arches in the perforation cavity under increasing fluid pressure gradient was observed in numerical simulation, as observed in the physical experiments.

However, none of the above DEM fluid flow couplings takes into account excess pore pressure generation and dissipation.

Hakuno and Tarumi (1988) developed a method to model liquefaction based on detecting all the pores among particles and connecting them by pipes. The pore water pressure was calculated by assuming constant volume elasticity for the water and the water pressure was proportional to the pore volume. Fluid flow between each pore space and its adjacent pores was calculated based on Darcy's law. This method resulted in a complicated calculation procedure and required subsequent manipulation. Nakase et al. (1999) improved Hakuno and Tarum's method by implementing square elements each containing 15 particles. The pore pressure generation in each cell

corresponded to particle movement in the neighboring cells and was proportional to the decrease of pore volume. The fluid force applied to the particle was depended on the pore pressure gradient between neighbor cells. Mori et al. (2001) studied the liquefaction analysis of River Dike using a two-dimensional discrete element model. In their study, the excess pore water pressure was considered to lead to large permanent displacement due to liquefaction at the microscope level. The accumulative excess pore water pressure caused by the combination of shear force and the effective normal force was equal to the initial effective normal force. The excess pore water pressure caused by the shear force was related to the dissipative energy and stored elastic energy of the model. Boutt et al. (2007) developed a fluid-solid coupling scheme by using LBM-DEM coupling approach by considering pore pressure change during simulation. The fluid node in LB model was constructed to present pore space. The pore pressure was calculated from fluid bulk modulus. The coupling was achieved through momentum transfer from the fluid to the solid by a no-slip condition at the solid/fluid interface. The model captured the 1-D consolidation behavior for both initial pressurization and fluid flow out of the domain. Boutt et al. (2010) then continue the study and apply the same model in 2-D sand production problem. The simulation results are qualitatively consistent with laboratory and field observation.

It is not easy to calculate excess pore water pressure using DEM since it is difficult to determine pore space connectivity and pore space deformation in a discontinuum. In this chapter, a new idea is proposed to incorporate excess pore water pressure calculation in DEM simulation by introducing a new water particle element which has a specific stiffness that enables the calculation of excess pore pressure due to pore space deformation. The pore water pressure is first calculated under the undrained condition, and subsequent dissipation of pore pressure is governed by pore

fluid diffusion using Darcy's Law. The new approach can be used to simulate wet granular deformation using DEM.

4.2. Proposed Methodology

4.2.1. Pore Pressure Generation Process

4.2.1.1 Formulation of loose packing sample

In formulating a new water particle element to calculate pore water pressure, cases with simple boundary conditions are first considered. Isotropic compression is a fundamental case of triaxial testing in which the soil sample is compressed by the same stress in all directions. A new model is firstly developed here based on three-dimensional isotropic compression. The derivation of all equations in this paper is based on the undrained condition of the soil sample. Consider an element of soil of volume V and porosity n, which is subjected to equal increases in total stress $\Delta\sigma_3$ in all directions, resulting an immediate increase in pore pressure ΔU, the reduction in volume of pore space ΔV_v is calculated as (Craig, 2004):

$$\Delta V_v = C_f n V \Delta U \qquad [4.1]$$

where C_f is the compressibility of pore fluid. Rearrange Equation 4.1 and the excess pore water pressure ΔU is calculated as:

$$\Delta U = \frac{\Delta V_v}{C_f n V} \qquad [4.2]$$

A simplified model is first developed with a cube sample. In this case, an assembly of regular distribution and single element size particles are confined by six frictionless confining walls, as shown in Figure 4.1 a and b. The initial state of the sample including the initial total volume V_0,

initial solid volume V_{s0}, initial void volume V_{vo} and initial void ratio e_0, and initial porosity of the sample are calculated as:

$$V_0 = L_0^3$$

$$V_{s0} = N\left(\frac{4}{3}\pi r^3\right)$$

$$V_{v0} = V_0 - V_{s0} \qquad\qquad [4.3]$$

$$e_0 = \frac{V_{v0}}{V_{s0}}$$

$$n_0 = \frac{e_0}{1 + e_0}$$

where L_0 is the cubic sample's original length, r is the particle radius, N is the total number of the particles and is calculated as:

$$N = \left(\frac{L_0}{2r}\right)^3 \qquad\qquad [4.4]$$
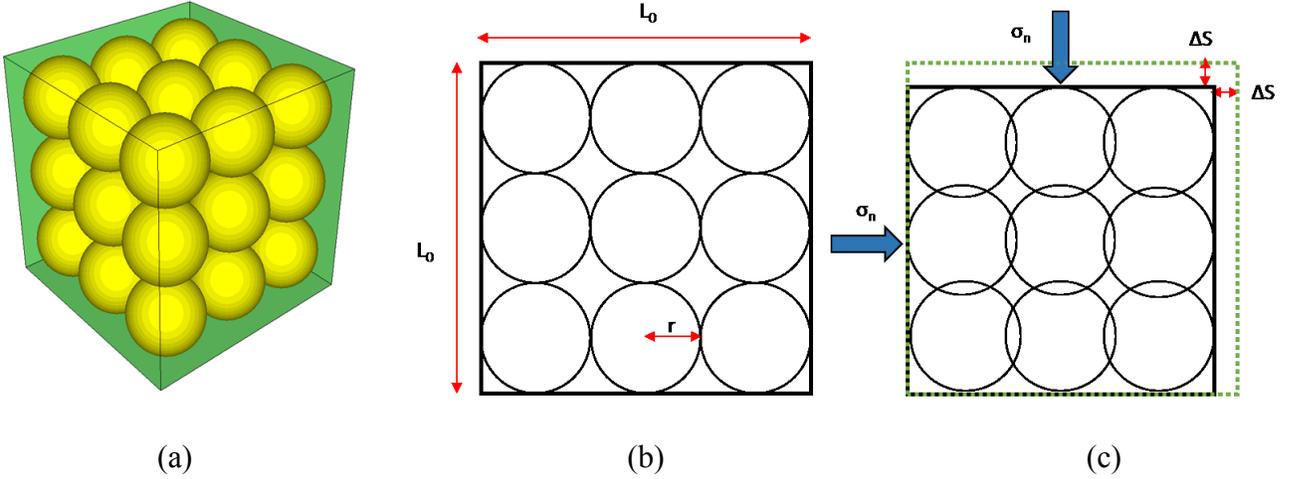
Figure 4.1: DEM particle deformation under isotropic stress compression. (a) 3D view, (b) Plan view before deformation, (c) Plan view after deformation.

When the sample is subjected to isotropic compression with stress equal to σ_n, only the normal force on the particle contact will be considered. The solid particles are considered to be incompressible. However, the intersections of the particles at the contact are allowed in order to model the reduction in the volume of the void as shown in Figure 4.1c. The total force applied on one side of the wall is calculated from:

$$F_{total} = \sigma_n L_0^2 \qquad [4.5]$$

The individual force on one particle is calculated from:

$$F = \frac{F_{total}}{N_1} \qquad [4.6]$$

where N_1 is the number of balls at contact with one side of the wall:

$$N_1 = N^{\frac{2}{3}} \qquad [4.7]$$

The intersection depth between two particles ΔS_{bb} and a particle and a wall ΔS_{b-w} are then calculated from:

$$\Delta S_{b-b} = \frac{F}{K_{b-b}}$$

$$\Delta S_{b-w} = \frac{F}{K_{b-w}}$$

[4.8]

where K_{b-b} and K_{b-w} are the combined stiffness between particle-particle contact and particle-wall contact and are calculated from:

$$\begin{cases} K_{b-b} = \frac{K_{solid}K_{solid}}{(K_{solid} + K_{solid})} = \frac{1}{2}K_{solid} \\ K_{b-w} = \frac{K_{solid}K_{wall}}{(K_{solid} + K_{wall})} = \frac{\alpha}{1+\alpha}K_{solid} \end{cases}$$

[4.9]

where K_{solid} is the normal stiffness of the single particle, and α is the ratio between the normal stiffness of current particle and wall such that $\alpha = \frac{K_{wall}}{K_{solid}}$.

The total displacement in one direction Δs and the sample's final volume V_1 is calculated from:

$$\Delta s = \left(N^{\frac{1}{3}} - 1\right)\Delta S_{b-b} + 2\Delta S_{b-w}$$

$$V_1 = (1 - \Delta s)^3$$

[4.10]

The volume of intersection is calculated as shown in Figure 4.2 a and b:

$$V_{b-b} = \frac{\pi}{12d}(R + r - d)^2[d^2 + 2d(R + r) - 3(R - r)^2]$$

[4.11]

86

$$V_{b-w} = \frac{\pi h^2}{3}(3r - h)$$

where V_{b-b} is the volume of particle-particle intersection, and V_{b-w} is the volume of particle-wall intersections.

(a)   (b)
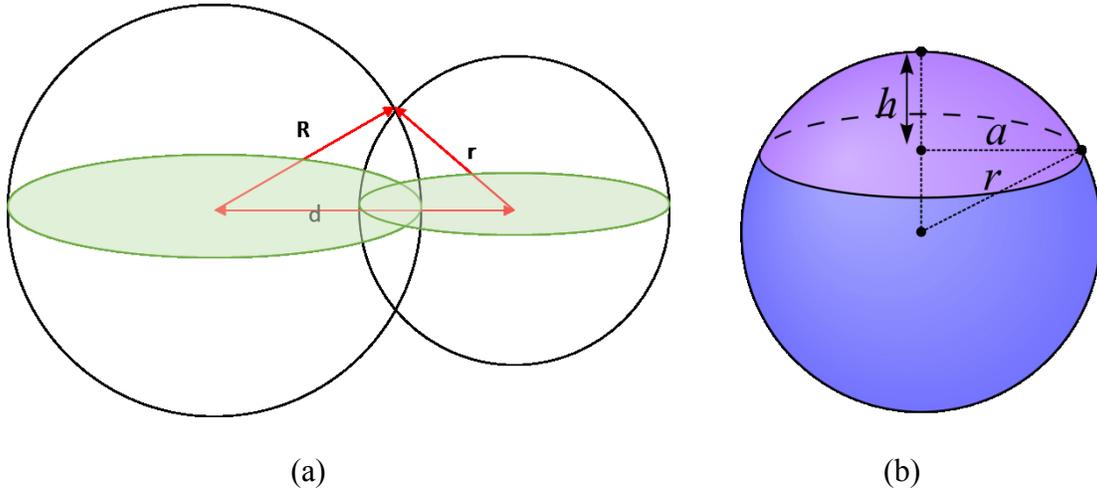
Figure 4.2: Calculation of particles intersection volume. (a) particle-particle intersection, (b) particle-wall intersection.

The final solid volume is calculated from:

$$V_{s1} = V_{s0} - \left(3N_1\left(N_1^{\frac{1}{2}} - 1\right)\right)V_{b-b} - (6N_1)V_{b-w} \qquad [4.12]$$

The pore space volume change ΔV_v can also be calculated. When the material is fully saturated, the volume reduction in the pore space will cause excess pore water pressure ΔU to build up, which can be calculated from Equation 4.2:

$$\Delta U = \frac{V_{v0} - V_{v1}}{C_f n_0 V_0} \qquad [4.13]$$

87

$$V_{v1} = V_1 - V_{s1}$$

where V_{v1} is void volume after deformation, and n_0 is the initial porosity.

In order to calculate the pore water pressure generated due to deformation of the discrete element, a water element is introduced that overlaps the solid element. Since the forces at the contact between solid elements represent effective stress in dry granular material, the introduction of water in the pores reduces the contact forces under the Principle of Effective Stress. In order to reduce the effective stress due to the generation pore water pressure in discrete modelling, the contact forces at the contact of the solid element should be reduced. Therefore the idea of the water element is to provide changes, increase or decrease, of the solid contact force due to the generation or dissipation of pore water pressure in the pores. In this case, the contact forces between two elements consist of a solid component and a fluid, water, component.

Compared with a solid element, the water element is assumed to have the size and location. The water element also has the same deformation at each contact points as the solid element, as shown in Figure 4.3. However, water element will have a different stiffness compared to solid element. In DEM analysis of undrained condition, the total stress is divided into two parts: effective stress and pore water pressure. The effective stress is carried by the solid element, and the pore water pressure is carried by the water element. The existence of water element will decrease the particle intersections during undrained condition compared with solid particle only case (drained condition). In other words, the pore pressure generated from the deformation of solid particles is now considered as an outer boundary pressure on the sample that only consist water particle. The water element stiffness k_{water} (micro) is then related to change in the pore space and the compressibility of water (macro) as:

$$k_{water} = \frac{2\Delta U L_0^2}{N_1 \Delta S_{b-b}}$$

[4.14]
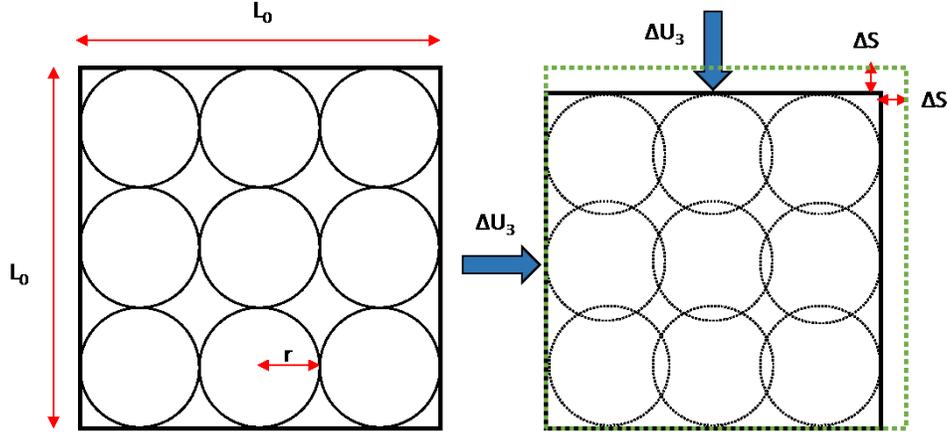
Figure 4.3: DEM water element arrangement before and after deformation

4.2.1.1 Formulation of irregular packing sample

When considering the random arrangement of particles in a numerical case as shown in Figure 4.4, the formulation in Equation 4.14 needs to be modified. In the discrete PFC^{3D} model, contact force and particle displacement are computed in the x, y, and z (defined by index i and with range set $i \in \{1,2,3\}$) direction, the average stress $\bar{\sigma}_{ij}$ in a volume V of material is defined by (Itasca, 2008):

$$\bar{\sigma}_{ij} = \frac{1}{V} \int \sigma_{ij} dV = \frac{1}{V} \sum_{N_p} \bar{\sigma}_{ij}^{(p)} V^{(p)}$$

[4.15]

(a)	(b)
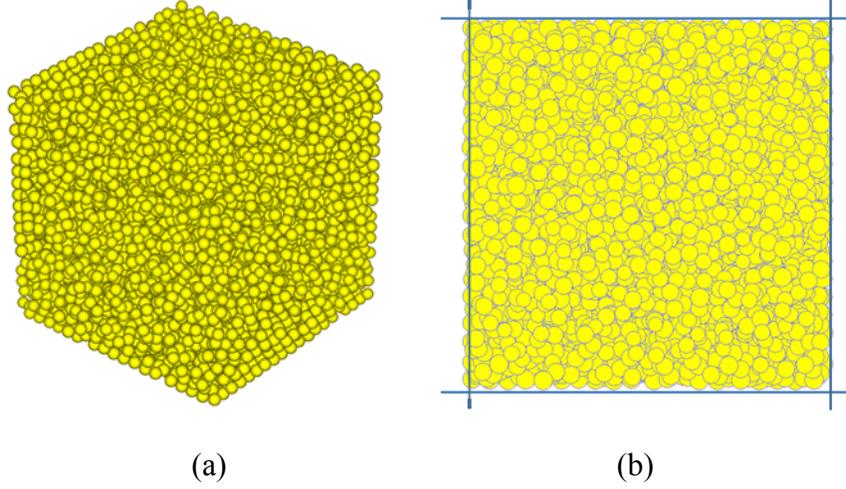
Figure 4.4: Random packing of particles in a cube sample. (a) 3D view, (b) Plan view.

where V is the total volume of material, $\bar{\sigma}_{ij}{}^{(p)}$ is the average stresses in particle *(p)*, $V^{(p)}$ is the volume of the particle *(p)*, and N_p is the number of particles in the control volume. In the same way, the average stress in each particle could be written using Equation 4.15 as:

$$\bar{\sigma}_{ij}{}^{(\phi)} = \frac{1}{V^{(\phi)}} \int \sigma_{ij}^{(\phi)} dV^{(\phi)}, \qquad \phi = \{p\} \qquad [4.16]$$

The identity $S_{ij} = \delta_{ik} S_{kj} = x_{i,k} S_{kj} = \left(x_i S_{kj} \right)_{,k} - x_i S_{kj}{}_{,k}$ holds for any tensor. Applying this identity to the stress tensor in each particle, one obtains:

$$\bar{\sigma}_{ij}{}^{(\phi)} = \frac{1}{V^{(\phi)}} \int \left[\left(x_i \sigma_{kj}^{(\phi)} \right)_{,k} - x_i \sigma_{kj,k}^{(\phi)} \right] dV^{(\phi)} = \frac{1}{V^{(\phi)}} \left\{ \left(I_{ij} \right)_1 - \left(I_{ij} \right)_2 \right\} \qquad [4.17]$$

where the integrals are denoted by $\left(I_{ij} \right)_1$ and $\left(I_{ij} \right)_2$. The first integral in Equation 4.17 can be rewritten as a surface integral by applying the Gauss divergence theorem such that

$$\left(I_{ij} \right)_1 = \int \left(x_i \sigma_{kj}^{(\phi)} \right)_{,k} dV^{(\phi)} = \int \left(x_i \sigma_{kj}^{(\phi)} \right) n_k dS^{(\phi)} = \int x_i t_j^{(\phi)} dS^{(\phi)} \qquad [4.18]$$

where $S^{(\phi)}$ is the boundary surface of the particle, n_k is the unit outward normal to the boundary surface, and $t_j^{(\phi)}$ is the traction vector, the term $\left(x_i \sigma_{kj}^{(\phi)}\right)$ is assumed to be continuously differentiable. If the moment carried by each parallel bond is neglected, and only point forces are applied at the particle contact, the above integral can be replaced by a sum over the number of contacts on the surface of particle $N_c^{(\phi)}$ as:

$$\left(I_{ij}\right)_1 = \sum_{N_c^{(\phi)}} x_i^{(c)} F_j^{(c,\phi)}$$

$$x_i^{(c)} = x_i^{(\phi)} + \left(x_i^{(c)} - x_i^{(\phi)}\right)$$

[4.19]

where $x_i^{(c)}$ is the location of the contact point and $x_i^{(\phi)}$ is the location of the particle centroid, and $F_j^{(c,\phi)}$ is the force acting on particle (ϕ) at contact (c). By substituting Equation 4.19 into Equation 4.18, one obtains

$$\left(I_{ij}\right)_1 = \sum_{N_c^{(\phi)}} x_i^{(\phi)} F_j^{(c,\phi)} + \sum_{N_c^{(\phi)}} \left(x_i^{(c)} - x_i^{(\phi)}\right) F_j^{(c,\phi)}$$

[4.20]

The second integral can be modified using the equations of motion for particle (ϕ), neglecting body forces, under the action of externally applied forces

$$\sigma_{kj,k} = \rho a_j = \rho \left(\frac{F_j}{m}\right) = \frac{F_j}{V}$$

[4.21]

where ρ is the density, a_j is the acceleration at the centroid, and F_j is the resultant force acting at the centroid. The second integral can be written following this relation

$$\left(I_{ij}\right)_2 = \int x_i \sigma_{kj,k}^{(\phi)} dV^{(\phi)} = \frac{F_j^{(\phi)}}{V^{(\phi)}} \int x_i dV^{(\phi)} = F_j^{(\phi)} x_i^{(\phi)} \qquad [4.22]$$

Substituting Equation 4.22 and 4.20 into Equation 4.18 gives

$$\bar{\sigma}_{ij}^{(\phi)} = \frac{1}{V^{(\phi)}} \sum_{N_c^{(\phi)}} \left(x_i^{(c)} - x_i^{(\phi)}\right) F_j^{(c,\phi)} \qquad [4.23]$$

Note that for the above equations, the particle may not be in static equilibrium, but the body forces should be small compared to the contact forces and no externally applied force acting on the particle. When we substitute Equation 4.23 into Equation 4.15, we get

$$\bar{\sigma}_{ij} = \frac{1}{V} \sum_{N_p} \bar{\sigma}_{ij}^{(p)} V^{(p)} = \frac{1}{V} \sum_{N_p} \sum_{N_c^{(p)}} \left(x_i^{(c)} - x_i^{(p)}\right) F_j^{(c,p)} \qquad [4.24]$$

where n is the porosity of the measurement region, $x_i^{(p)}$ and $x_i^{(c)}$ are the coordinates of the centroid and contact points of a particle, respectively, $F_j^{(c,p)}$ is the force acting on a particle (p) at contact (c). $F_j^{(c,p)}$ includes both the contact and parallel-bond normal and shear forces, but neglects the moment due to the parallel-bond. A contact force has both normal and shear components and the normal component can be calculated from:

$$F_j^{(c,p)n} = K^n D_j^n$$

$$D_j^n = D_{total}^n \frac{x_j^p - x_j^c}{\sqrt{\sum_{j=1}^{j=3}\left(x_j^c - x_j^p\right)^2}} \qquad [4.25]$$

$$D_{total}^n = 2 \left[R^A - \sqrt{\sum_{j=1}^{j=3} \left(x_j^c - x_j^p \right)^2} \right]$$

where K^n is the combined stiffness between the two entities (solid and water) at the contact, D_j^n is the particle intersection in the x, y, and z component and can be calculated by first finding the total intersection D_{total}^n in the direction normal to the contact plane as shown in Figure 4.5.

(a)   (b)
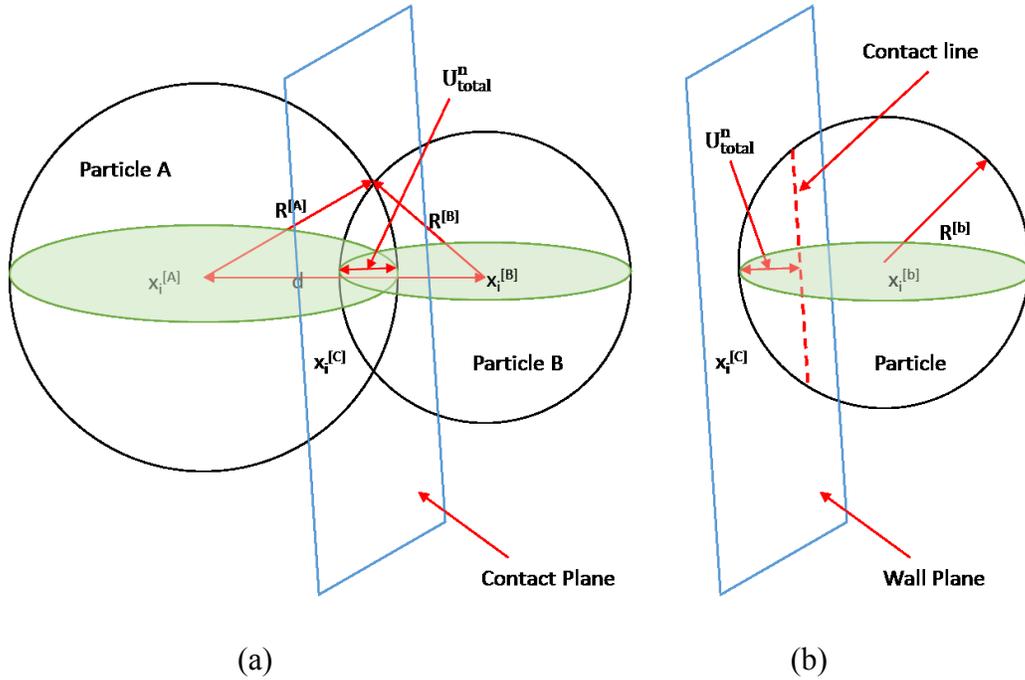
Figure 4.5: Notations used to describe (a) Particle-particle contact (b) Particle-wall contact

In relating the pore water pressure in a water element to the contact forces acting on the water element, the pore water pressure can be related to the average means stress due to the water particle contact forces. Mathematically it can be written as:

$$\Delta U = \overline{\sigma_{ii(w)}} = \frac{1}{3} \left(\frac{1}{V_{total}} \right) \left[\sum_{i=1}^{i=3} \sum_{N_p} \sum_{N_c^{(p)}} \left(x_i^c - x_i^p \right) F_{i(w)}^{(c,p)} \right] \tag{4.26}$$

$$F_{i(w)}^{(c,p)} = K_{w(c)}D_i^n$$

where $\overline{\sigma_{u(w)}}$ is the stress caused by fluid element averaged from 3 principle direction in sample, $F_{i(w)}^{(c,p)}$ is the contact force provided by fluid element, $K_{w(c)}$ is the combined normal stiffness of fluid particles in the linear contact model and is calculated from:

$$\begin{cases} K_{w(c)} = \dfrac{K_w K_w}{(K_w + K_w)} = \dfrac{1}{2}K_w; \text{ for particle} - \text{particle contact} \\ K_{w(c)} = \dfrac{K_w K_{wall}}{(K_w + K_{wall})} = \dfrac{\alpha}{1 + \alpha}K_{solid}; \text{ for particle} - \text{wall contact} \end{cases} \quad [4.27]$$

where K_w is the normal stiffness of the single water particle, and α is the ratio between the normal stiffness of current water particle and wall expressed as $\alpha = \dfrac{K_{wall}}{K_w}$:

When substituting Equation 4.27 into Equation 4.26, it results in:

$$\Delta U = \frac{1}{3V_{total}}\left[\sum_{i=1}^{i=3}\sum_{N_p}\sum_{N_c^{(p)}}(x_i^c - x_i^p)K_{w(c)}(\eta D_i^n)\right] \quad [4.28]$$

$$\eta = \begin{cases} \dfrac{1}{2}; for\ particle - particle\ contact \\ \dfrac{\alpha}{1 + \alpha}; for\ particle - wall\ conatct \end{cases} \quad [4.29]$$

Since water particle has zero shear stiffness, the only unknown is normal stiffness of water particle. The pore pressure in an undrained sample is averaged along 3 principle directions, the water particle stiffness is then calculated by using the average method:

$$K_w = \frac{3V_{total}\Delta U}{\sum_{i=1}^{i=3}\sum_{N_p}\sum_{N_c^{(p)}}(x_i^c - x_i^p)(\eta D_i^n)}$$ [4.30]

Potyondy and Cundall (2004) states that for sample with a constant solid Young's modulus E_s, the normal stiffness of sample is calculated as:

$$K_{sm} = 4R_m E_s$$ [4.31]

where R_m is the radius of each particle, for sample with particle size distribution, the calculated normal stiffness is different for each of the particle. Rearrange of Equation 4.31, the Young's modulus of sample can be calculated as:

$$E_s = \frac{K_{s(avg)}}{4R_{avg}}$$ [4.32]

where $K_{s(avg)}$ is the average particle solid stiffness, and R_{avg} is the average particle radius. The calculated water particle stiffness can be treated as the average stiffness, by using Equation 4.32, an virtual Young's modulus for water particle E_w is introduced here:

$$E_w = \frac{K_{w(avg)}}{4R_{avg}}$$ [4.33]

The water particle stiffness for each particle is then calculated as:

$$K_{wm} = 4R_m E_w$$ [4.34]

4.2.2. Pore Pressure Dissipation Process

The consolidation process of soil or porous medium, which is the gradual reduction in the volume of a fully saturated soil of low permeability due to the draining of some of the pore water, will

continue until the excess pore water pressure has been completely dissipated. During this water diffusion process, the excess pore pressure will drop from a maximum value to zero while the effective stress carried by soil skeleton will increase to a value which is equal to the total stress when the pore water pressure is zero.

In DEM analysis, the total stress is divided into two parts: effective stress and pore pressure. The effective stress is carried by solid particle, and pore pressure is carried by water particle. During water diffusion process, the total stress on the outer boundary wall is maintained the same, and the solid stiffness remains unchanged. However, the volume of the total sample decreases due to the drainage of some of the pore water, the DEM simulations here reduce the water particle stiffness in a certain amount to maintain an expected volume reduction. The total water diffusion process in DEM simulation can be shown in Figure 4.6：
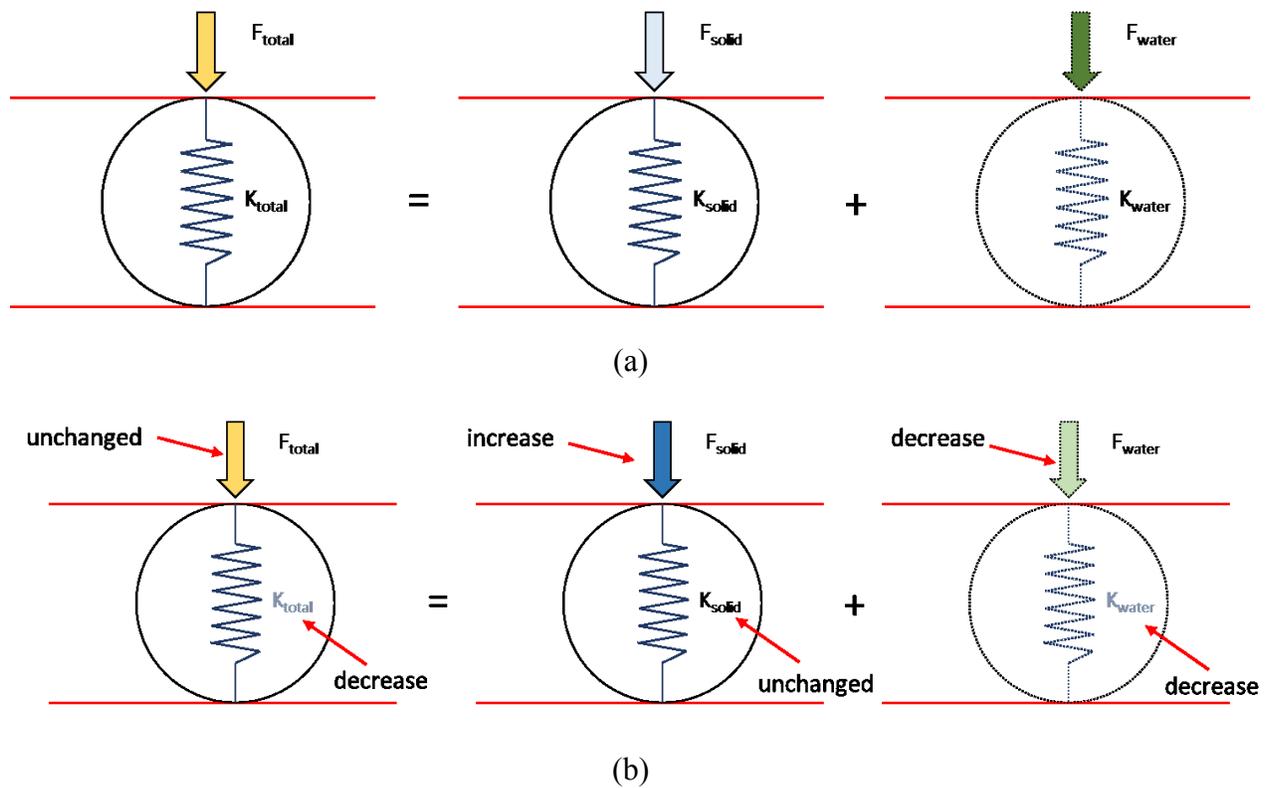
Figure 4.6：DEM simulation of effective stress and pore pressure (a) before water diffusion process (b) during water diffusion process

4.2.2.1 Loose packing

In order to calculate the water particle stiffness for various degree of consolidation or various stages of pore water diffusion, several particle packing configurations will be considered. The calculation of the water particle stiffness is important since it controls the component of the contact force that will be supported by the water element and the remaining part supported by the solid element. By changing the stiffness of the water element, different degree of consolidation can be simulated by changing the forces support by the water element.

First, the loosest particle packing configuration with uniform particle size is considered for 1D consolidation analysis as shown in Figure 4.7. The force between particles is only transmitted in

the vertical direction along the z axis. Therefore, during drained dissipation process, there is no force acting on side walls in the x and y directions.

(a)   (b)
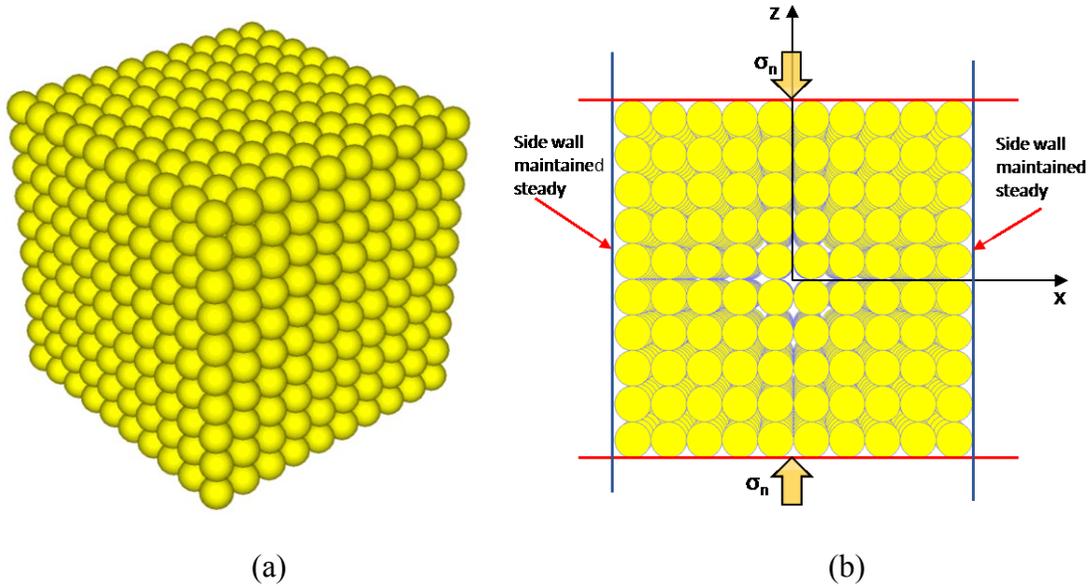
Figure 4.7: DEM formulation of loose packing. (a) 3D view, (b) the x-z plane view

During consolidation, pore water pressure can be converted to particle contact force between two particles calculated from the water particle stiffness:

$$p_1 = \alpha p_0 \qquad\qquad [4.35]$$

$$F_{w1} = \alpha F_{w0} \qquad\qquad [4.36]$$

where p_1 and p_0 are pore pressure in the sample before and after dissipation occurs, F_{w0} and F_{w1} are the force at the contact between two particles calculated from the water particle stiffness before and after pore pressure reduction, and α is the reduction factor range from 0 to 1. For particle-particle contact:

$$F_{w0} = \Delta_0 \frac{K_{w0}{}^2}{2K_{w0}} \qquad\qquad [4.37]$$

$$F_{w1} = \Delta_1 \frac{K_{w1}{}^2}{2K_{w1}} \qquad\qquad [4.38]$$

$$\Delta_0 = \frac{F}{\left(\dfrac{(K_s + K_{w0})(K_s + K_{w0})}{(K_s + K_{w0}) + (K_s + K_{w0})}\right)} \qquad\qquad [4.39]$$

$$\Delta_1 = \frac{F}{\left(\dfrac{(K_s + K_{w1})(K_s + K_{w1})}{(K_s + K_{w1}) + (K_s + K_{w1})}\right)} \qquad\qquad [4.40]$$

where K_{w0} and K_{w1} are the water particle stiffness before and after the pore pressure reduction, K_s is the solid particle stiffness and it is a constant during the pore pressure dissipation process, Δ_0 and Δ_1 are the particle – particle intersection before and after the pore pressure reduction, and F is the total force maintained on the particle contact when combining Eq. 4.37 to 4.40 with Eq. 4.36. The water particle stiffness after pore pressure reduction is calculated as:

$$K_{w1} = \frac{\alpha K_{w0}\Delta_0 K_s}{2 - \alpha K_{w0}\Delta_0} \qquad\qquad [4.41]$$

4.2.2.1 Dense and Irregular packing

For the random particle packing as shown in Figure 4.8, the force between the particles is not only transmitted in the vertical direction along z axis for 1D consolidation; it is also transmitted in horizontal directions along x and y axis because of irregular contacts between particles. Although no deformation is allowed to occur in the x and y directions due to the boundary walls, stresses are still generated on the boundary walls, which mean that the linear relationship between single force

induced by water particle on a contact and the pore pressure of the whole sample no longer exist. In this case, the water particle stiffness can be determined using an iterative scheme.

(a)   (b)
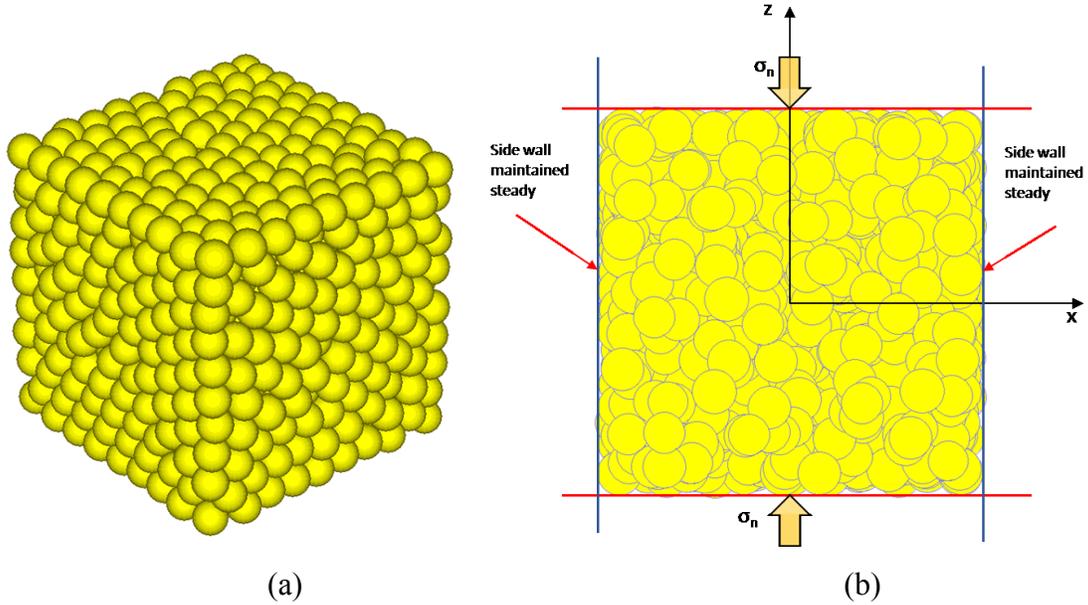
Figure 4.8: DEM formulation of irregular packing. (a) 3D view, (b) the x-z plane view

During the water pressure dissipation process, a pore pressure dissipation factor β is used to calculate the degree of changes of pore pressure as:

$$u_1 = \beta u_0 \tag{4.42}$$

where u_1 is the pore pressure at the current stage of pore pressure dissipation, and u_0 is the initial pore pressure of the whole sample. It is assumed that the change in pore pressure is uniform through the sample and the contact forces of the water particle will change by the same percentage as the pore pressure. In other words, the same β value can be used in calculating the current contact force in the water particle:

$$F_{w1} = \beta F_{w0} \tag{4.43}$$

$$F_{w0} = \Delta_0 K_{w0}$$

$$F_{w1} = \Delta_1 K_{w1}$$

where F_{w0} and F_{w1} are the force on a contact between two particles calculated from the water particle stiffness before and after the pore pressure reduction, and K_{w0} and K_{w1} are the water particle stiffness before and after the pore pressure reduction, Δ_0 and Δ_1 are the contact intersection between two particles before and after the pore pressure reduction.

Since total force F_t applied on the contact is the same before and after the pore pressure dissipation, then:

$$F_t = F_s + F_w = K_s\Delta_0 + K_{w0}\Delta_0 = K_s\Delta_1 + K_{w1}\Delta_1 \qquad [4.44]$$

where F_s and F_w are the contact force induced by solid and water stiffness respectively, K_s is the solid particle stiffness and is kept as a constant during pore pressure dissipation process. Assuming that the pore pressure reduction is linearly related to the changes in effective stress, it follows that:

$$K_s\Delta_1 = K_s\Delta_0 \left(\frac{(1-\beta)\Delta_0 K_{w0} + K_s\Delta_0}{K_s\Delta_0} \right) \qquad [4.45]$$

Substituting Eq. 4.45 in Eq. 4.43, a new water stiffness can be calculated from:

$$K_{w1} = \frac{\beta K_{w0}}{(1-\beta)\frac{K_{w0}}{K_s} + 1} \qquad [4.46]$$

In DEM calculation, because each particle will have its own pore pressure reduction factor β_m, the pore pressure u_m calculation is based on individual particle m, and modified from Eq. 4.28:

$$u_m = \frac{1 - n_{avg}}{V_m^{(p)}} \left[\sum_{N_c^{(p)}} (x_i^c - x_i^p) K_{w(c)} \gamma D_i^n \right]$$ [4.47]

where $V_m^{(p)}$ is the volume of individual particle m, $K_{w(c)}$ is the combined water stiffness at a contact between two particles, and n_{avg} is the average porosity of the whole sample. Due to the nonlinear relationship between the single force induced by the water particle on a contact and the pore pressure of the whole sample, the pore pressure dissipation factor β cannot be directly calculated from Eq. 4.46. The final pore pressure dissipation factor β is calculated from the bisection method (Chapra, 2012):

$$Q_n = u_{n(DEM)} - u_f, u_f = \alpha u_0$$

$$if\ Q_n > 0, \beta_{right} = \beta_n\ and\ \beta_{n+1} = \frac{\beta_{left} + \beta_{right}}{2}$$ [4.48]

$$if\ Q_n < 0, \beta_{left} = \beta_n\ and\ \beta_{n+1} = \frac{\beta_{left} + \beta_{right}}{2}$$

where α is the target pore pressure reduction factor, $u_{n(DEM)}$ is the pore pressure calculated at the end of current DEM iteration. Subscript n denotes the number of iteration steps, β_{left} and β_{right} are minimum and maximum boundary values of β. The first trial values of β_{left} and β_{right} are 0 and 1, respectively. The first trial value of β is equal to α. β_{n+1} is then calculated based on boundary values and will be used in the next iteration. The iterative process continue until the changes in pore pressure are within a specified tolerance:

$$\frac{\frac{u_{n(average)}}{u_{0(average)}} - \alpha}{\alpha} \leq 0.005 \qquad [4.49]$$

where $u_{n(average)}$ is the DEM calculated pore pressure, averaged from total number of particles.

The graphic depiction of the bisection method to find the final pore pressure dissipation factor β

is illustrated in Figure 4.9: a. The algorithm for the DEM calculation is presented in Figure 4.9: b:

(a)

Calculate pore pressure of individual particles before pore pressure dissipation, marked as u_0

If $u_0 = 0$, $u_0 = u_{average}$

Reduce particle stiffness, by formula: $K_{w1} = \dfrac{\beta K_{w0}}{(1-\beta)\frac{K_{w0}}{K_s}+1}$

PFC calculation until steady state

Calculate pore pressure of individual particles after pore pressure dissipation, marked as u_1

$Q_n = u_{n(DEM)} - u_f, u_f = \alpha u_0$

$if Q_n > 0, \beta_{right} = \beta_n \quad \beta_{n+1} = \dfrac{\beta_{left} + \beta_{right}}{2}$

$if Q_n < 0, \beta_{left} = \beta_n \quad \beta_{n+1} = \dfrac{\beta_{left} + \beta_{right}}{2}$

$\dfrac{\frac{u_{1(avg)}}{u_{0(avg)}} - \alpha}{\alpha} \le 0.005$

Exit

(b)

Figure 4.9: (a) A graphical depiction of the bisection method based on DEM calculation. (b)The scheme of iteration method to find the corresponding pore pressure dissipation factor.

4.3. Numerical verifications and results

4.3.1. Undrained deformation - Loose packing

The loose packing sample simulated here is used to verify the derivation from Equation 4.3 to Equation 4.14. The DEM model in loose packing state is generated in a cube box with the length,

width and depth of 20 mm, bounded by six frictionless rigid walls as shown in Figure 4.10. Table

4.1 presents the DEM micro-properties for this model.
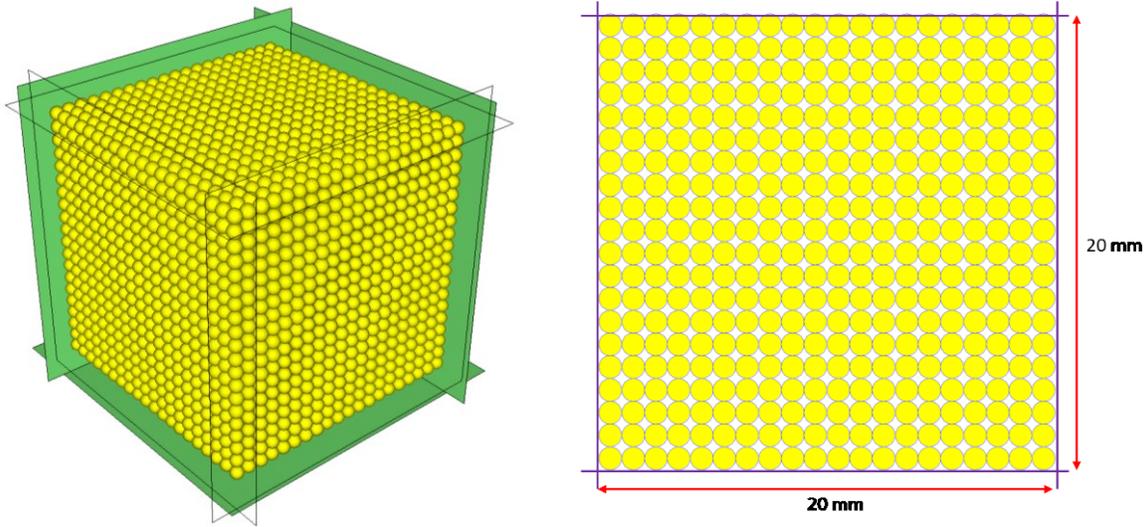
Figure 4.10: DEM generation of loose packing particles (a) 3-D view; (b) plane view.

Table 4.1: The detail of isotropic compression example in loose packing state.

Parameters	Values	Units
Sample Height (H)	20	mm
Sample Length (L)	20	mm
Sample Width (W)	20	mm
Wall Normal Stiffness (K_{nwall})	7×10^7	N/m
Wall stiffness ratio (K_{nwall}/K_{swall})	1	
Particle Normal Stiffness (K_{nball})	1.4×10^7	N/m
Particle stiffness ratio (K_{nball}/K_{sball})	1	
Particle Radius (r)	0.5	mm
Particle Density (ρ)	2650	kg/m^3
Number of Particles	8000	
Particle Friction Coefficient (μ)	0.5	
Initial Porosity	0.46387	
Gravity (g)	9.8	m/s^2
Compressibility of Water (C_w)	4.6×10^{-10}	m^2/N

In analytical solution, the first step is to obtain the compressibility of soil skeleton C_s, which is

calculated based on DEM solid particle only case. An isotropic stress of 1 MPa is applied on the

cube sample by using servo control algorithm until steady state reached. The initial total volume of sample V_0 and change of total volume ΔV is calculated from Equation 4.3 and Equation 4.10, the C_s is then calculated from:

$$C_s = \frac{\Delta V/V_0}{\Delta \sigma}$$

[4.50]

$$\Delta \sigma = \frac{1}{3}(\Delta \sigma_1 + \Delta \sigma_2 + \Delta \sigma_3)$$

[4.51]

where $\Delta \sigma$ is the average total stress increment, and $\Delta \sigma_1$, $\Delta \sigma_2$, $\Delta \sigma_3$ are the total stress increase on the sample in three principle stress directions.

The analytical solution of the pore pressure buildup is based on fundamental soil mechanics, the pore pressure build-up under isotropic compression can be calculated using pore pressure B parameter as:

$$\Delta U = \Delta \sigma B$$

[4.52]

$$B = \frac{1}{1 + n_0 \frac{C_w}{C_s}}$$

where C_w is the compressibility of water from Table 4.1, n_0 is the initial porosity of the whole sample, calculated from Equation 4.3. When a continuous outer boundary total stress increment from 0 MPa to 5 MPa on the sample is applied, a continuous pore pressure generation can then be calculated from Equation 4.52.

In the case of an undrained test, when the fluid and soil grains are fully incompressible, and the sample is fully saturated, no volume change will occur after isotropic compression and the entire load will be carried by the pore fluid. However, if both fluid and soil grains are assumed compressible, fluid and soil will theoretical resist part of the total load. In the presented DEM analysis, the total stress is divided into two parts: effective stress and pore pressure. The effective stress is carried by the solid particle, and pore pressure is carried by the water particle as shown in Figure 4.11.
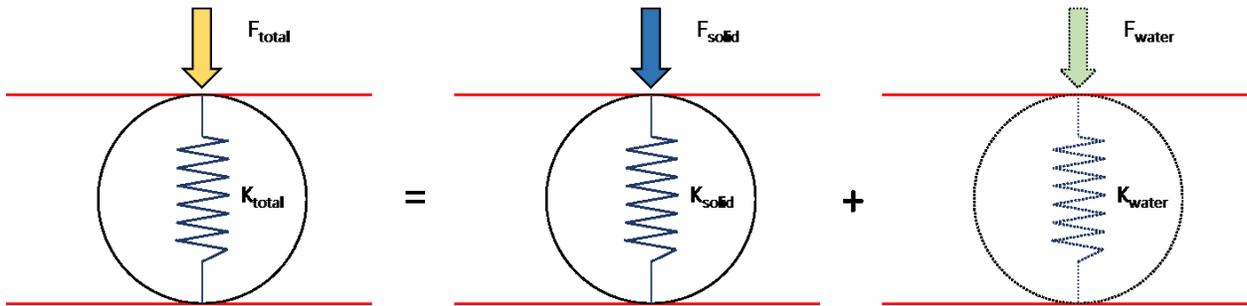
Figure 4.11: DEM simulation of effective stress and pore pressure

In DEM simulation, a continuous outer boundary total stress increment from 0 MPa to 5 MPa on the sample is applied in steps. The isotropic stress of 1 MPa is first applied on the sample with the solid particle only since the water particle stiffness is calculated from the pore pressure buildup due to porosity change from Equation 4.14. The calculated water particle stiffness is then applied back to the original sample with 0 MPa's outer boundary total stress. Then both solid and water particles are activated, and both particles experienced an outer boundary total stress increment of 1 MPa. The water particle stiffness in the next load increment, from 1 MPa to 2 MPa, will be adjusted based on the pore pressure increase difference of the current load increment:

$$K_w^{n+1} = K_w^n + \Delta K_w \qquad [4.53]$$

where K_w^{n+1} is the water particle stiffness at next loading increment, K_w^n is the water particle stiffness at the current loading increment, and ΔK_w is the adjusted water particle stiffness and is calculated from Equation 4.14:

$$\Delta K_w = \frac{2\Delta U' L_0^2}{N_1 \Delta S_{b-b}}$$ [4.54]

where $\Delta U'$ is the difference in pore pressure build up between the two loading increment and is calculated by:

$$\Delta U' = \Delta U^{n+1} - \Delta U^n$$ [4.55]

The result of isotropic compression test is shown in Figure 4.12 and Figure 4.13, which show good agreements between analytical and numerical results.
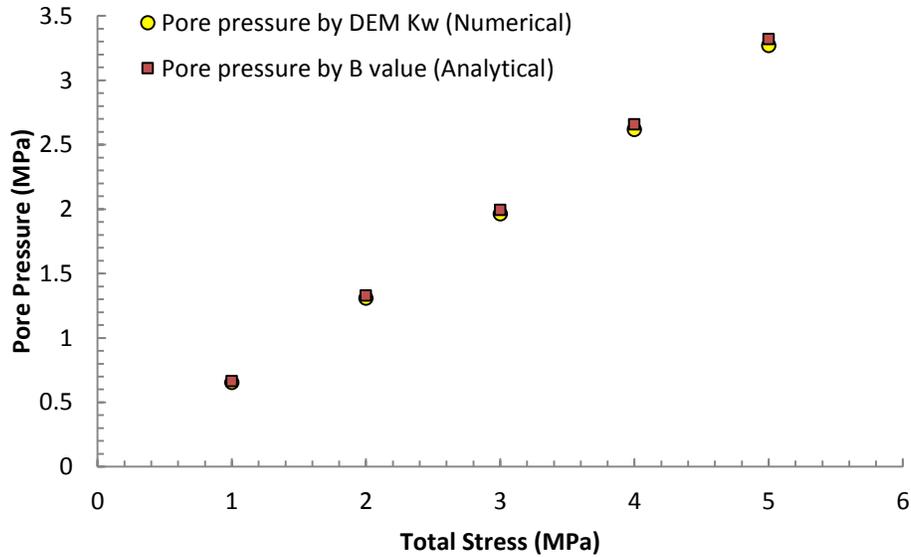
Figure 4.12: Comparison between analytical and numerical pore pressure buildup against the total stress increase on boundary walls in isotropic compression case with loose particle packing.
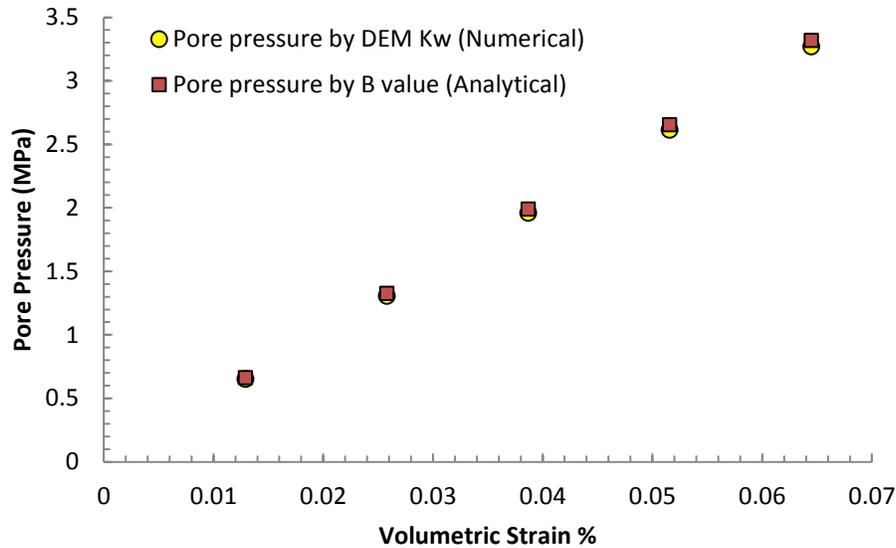
Figure 4.13: Comparison between analytical and numerical pore pressure build up against the volumetric strain of cube sample in isotropic compression case with loose particle packing.

4.3.2. Undrained deformation - Irregular packing

The irregular packing sample presented here is used to verify the derivation from Equation 4.15 to Equation 4.30. Here two cases are considered, the first case is isotropic compression and the second case is triaxial compression.

4.3.2.1. Isotropic compression

The DEM model for isotropic compression case is generated in a cube box with the length, width and depth of 20 mm, bounded by six frictionless rigid walls as shown in Figure 4.14. Table 4.2 presents the DEM micro-properties for this model. The sample is first compacted by applying three perpendicular and unequal stresses 0.1 MPa using a servo control algorithm. The model is run until the average unbalanced forces divided by average contact forces became equal to or smaller than 0.01.

To measure the porosity of the sample, a group of measurement spheres is first inserted into the sample, as shown in Figure 4.14. The measurement sphere is a built-in tool in PFC^{3D} to help the user to calculate quantities such as porosity, stress and strain rate in a specific measurement volume (Itasca, 2008). Significant errors in the calculated porosity will result when the measurement sphere includes only four or fewer particles (Itasca, 2008). On the other hand, inaccurate permeability calculations result when some part of the measurement sphere covers outside the sample (Cui et al., 2016). As shown in Figure 4.15, the criterion for distance d from measurement boundary to boundary wall, in radial direction is:

$$d < \frac{\Delta s}{2}$$
[4.56]

where Δs is the total displacement in one principle direction within maximum applied boundary stress during simulation, calculated from the movement of boundary walls.

Therefore, the number of particles with centroids that lie in the specific measurement sphere is determined first at the beginning of the calculation to assure at least 10 particles (chosen in this study) is included in the measurement sphere. In this case, the radius of measurement sphere is assigned as 2 mm.

(a)   (b)
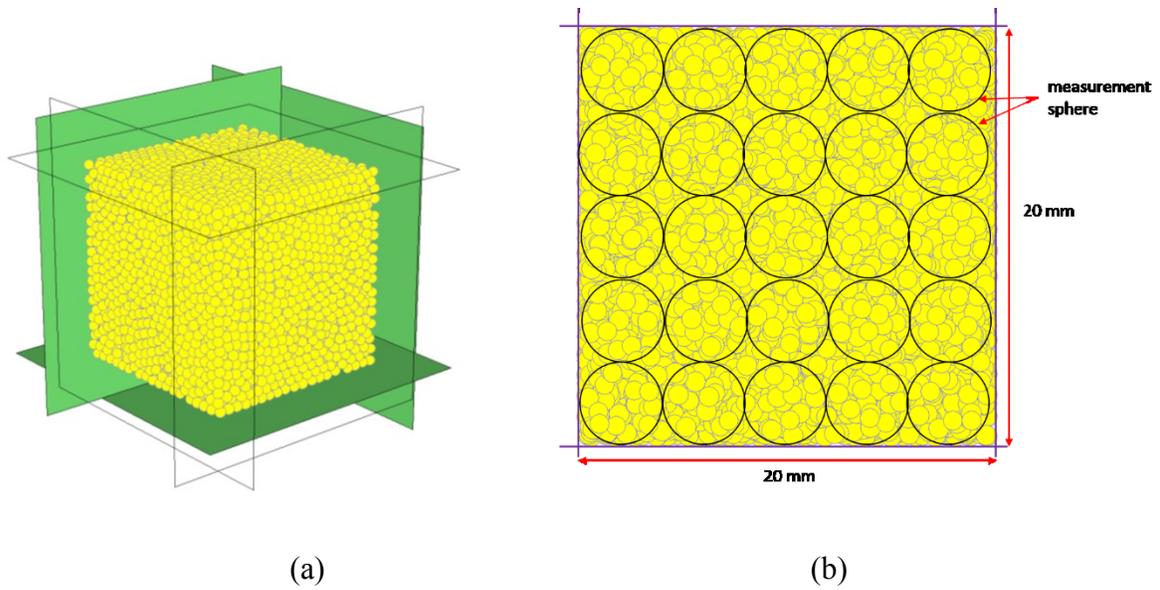
Figure 4.14: Discrete element model of the isotropic compression example (a) 3D view; (b) plane view with the location of measurement spheres.
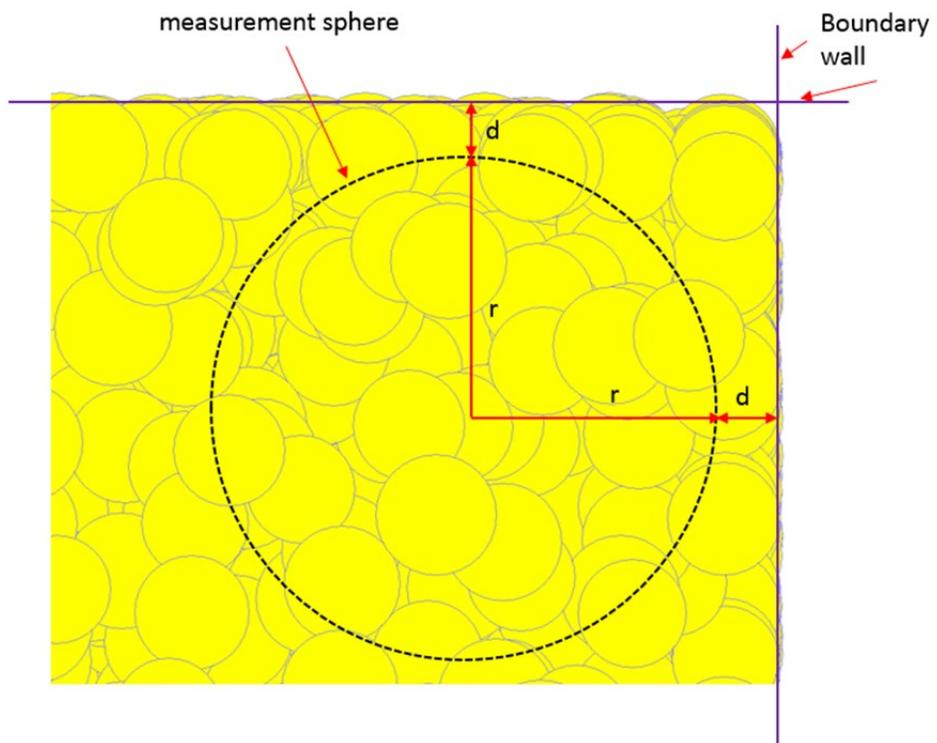
Figure 4.15: Location of measurement sphere related to boundary wall

111

Table 4.2: The detail of isotropic compression example in irregular packing state

Parameters	Values	Units
Sample Height (H)	20	mm
Sample Length (L)	20	mm
Sample Width (W)	20	mm
Wall Normal Stiffness (K_{nwall})	7×10^7	N/m
Wall stiffness ratio (K_{nwall}/K_{swall})	1	
Particle Normal Stiffness (K_{nball})	1.4×10^7	N/m
Particle stiffness ratio (K_{nball}/K_{sball})	1	
Particle Radius (r)	0.5	mm
Particle Density (ρ)	2650	kg/m³
Number of Particles	9931	
Particle Friction Coefficient (μ)	0.5	
Initial Porosity	0.362	
Gravity (g)	9.8	m/s²
Compressibility of Water (C_w)	4.6×10^{-10}	m²/N

A continuous outer boundary total stress increment from 0.1 MPa to 5 MPa on the sample is applied in steps. The isotropic stress of 1 MPa is first applied on the sample with the solid particle only in order to calculate the water particle stiffness from Equation 4.30. The calculated water particle stiffness is then applied back to the original sample with 0.1 MPa's outer boundary total stress. Then both solid and water particles are activated, and both particles experienced an outer boundary total stress increment of 0.9 MPa. The water particle stiffness in the next load increment, from 1 MPa to 2 MPa, will be adjusted based on the pore pressure increase difference of the current load increment from Equation 4.53. The adjusted water particle stiffness ΔK_w is calculated from Equation 4.30:

$$K_w = \frac{3V_{total}\Delta U'}{\sum_{i=1}^{i=3} \sum_{N_p} \sum_{N_c^{(p)}} \left(x_i^c - x_i^p\right)\left(\eta D_i^n\right)} \qquad [4.57]$$

The analytical pore pressure buildup against the total stress increase on boundary walls is calculated by using the same procedures in the loose packing case.

In numerical solution, the pore pressure build-up is calculated by the applied water particle stiffness in DEM phase, from Equation 4.26. Another way to calculate pore pressure builds up in numerical solution is to use porosity change calculated from measurement sphere, from Equation 4.13:

$$\Delta U = \frac{\Delta V_v}{C_w n_0 V_0} \qquad [4.58]$$

where C_w is the compressibility of water, n_0 is the initial porosity before the total stress increase, V_0 is the initial controlled total volume, and ΔV_v is the void volume change during compression:

$$\Delta V_v = V_{v0} - V_{v1} = V_0 n_0 - V_1 n_1 \qquad [4.59]$$

where V_1 is the total control volume after deformation, n_1 is the porosity after the total stress increase.

The result of isotropic compression test is shown in Figure 4.16 and Figure 4.17, which show good agreements between analytical and numerical results. The good agreement between DEM results and analytical solution reveals the capability of this approach in simulating fluid-solid interactions under undrained condition.
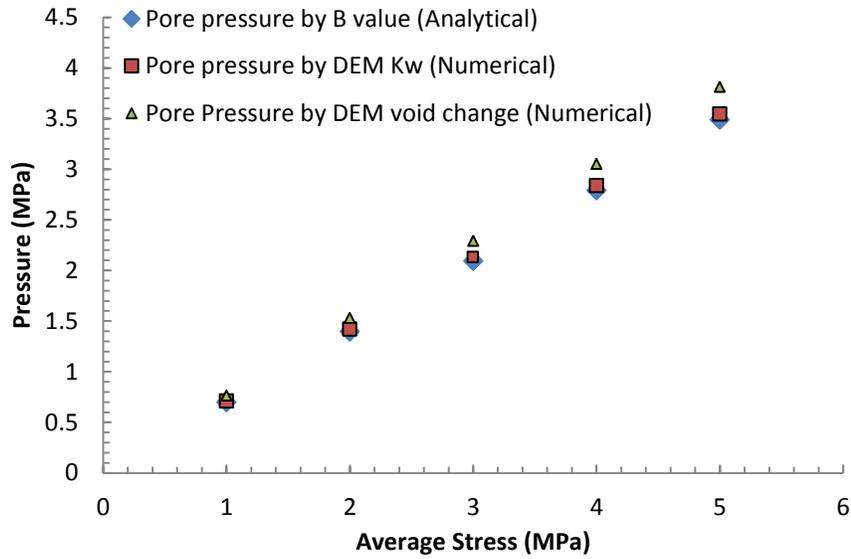
Figure 4.16: Comparison between analytical and numerical pore pressure build up against the total stress increase on boundary walls in isotropic compression case
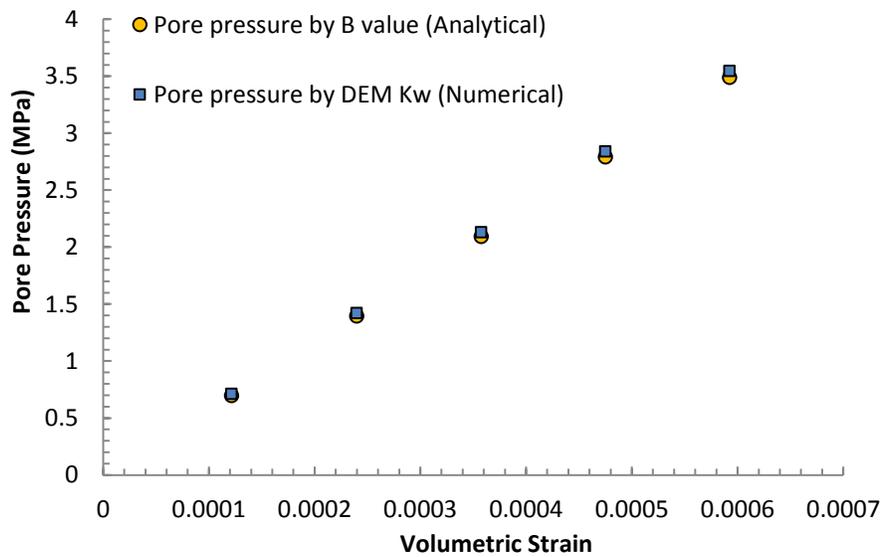
Figure 4.17: Comparison between analytical and numerical pore pressure build up against the volumetric strain of cube sample in isotropic compression case

114

4.3.2.2. Triaxial Undrained Test

The unconsolidated undrained triaxial test is a classical problem in soil mechanics, which can be described as a cylindrical specimen subjected to a specified all-round pressure and then the principal stress difference is applied immediately with no drainage allowed.

A DEM model is generated using two horizontal and one cylindrical rigid wall with a radius of 25 mm and height of 100 mm, shown in Figure 4.18. To obtain the optimum calculation speed, the simulation here increase the particle size to 1mm but keep the same Young's modulus (7×10^9 Pa in current simulation) compared with the isotropic compression test. The micro-parameters of the DEM model is presented in Table 4.3. A radial stress of 0.01 MPa is applied at the outer boundary by moving the outer cylindrical wall together with the top and the base platens using a servo control algorithm after the sample generation. The calculations are continued until the ratio of average unbalanced force to the average contact forces converge to 0.01.

(a)   (b)
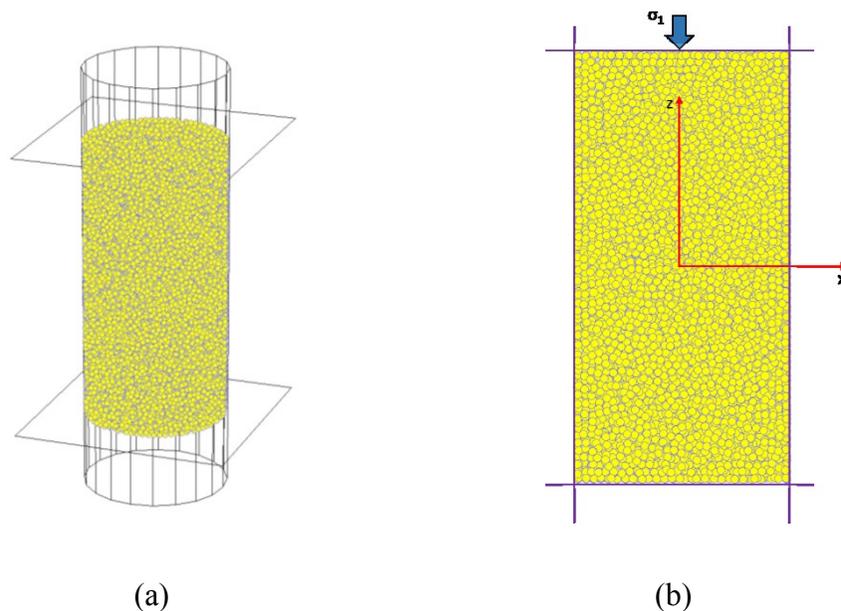
Figure 4.18: Discrete element model of the triaxial compression sample (a) 3D view; (b) the x-z plane view.

115
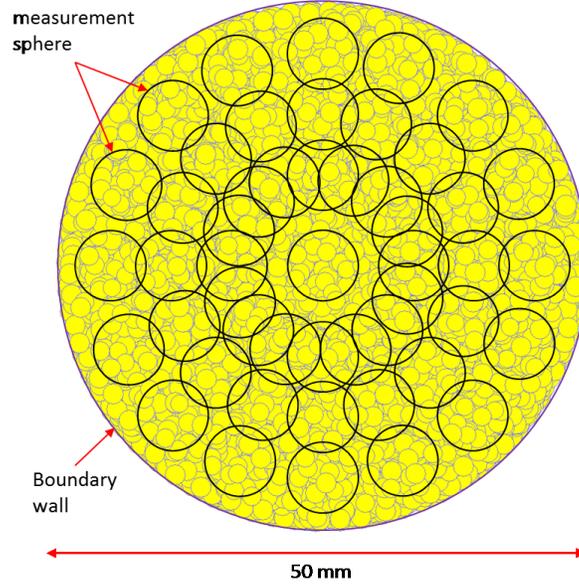
Figure 4.19: Location of measurement spheres in cylindrical sample in the x-y plane view

Table 4.3: The detail of triaxial compression example.

Parameters	Values	Units
Sample Height (H)	100	mm
Sample Radius (R)	25	mm
Wall Normal Stiffness (K_{nwall})	1.4×10^8	N/m
Wall stiffness ratio (K_{nwall}/K_{swall})	1	
Particle Normal Stiffness (K_{nball})	2.8×10^7	N/m
Particle stiffness ratio (K_{nball}/K_{sball})	1	
Particle Radius (r)	1	mm
Particle Density (ρ)	2650	kg/m^3
Number of Particles	31858	
Particle Friction Coefficient (μ)	0.5	
Initial Porosity	0.359	
Gravity (g)	9.8	m/s^2
Compressibility of Water (C_w)	4.6×10^{-10}	m^2/N

The measurement spheres are introduced with 4 sections in the radial direction, 16 sections in the circumferential direction, and 20 in the vertical direction, as shown in Figure 4.19. The porosity change of the sample is calculated by the average readings from all measurement spheres.

During the triaxial test, a continuous outer boundary axial stress increment in the z direction from 0.1 MPa to 4 MPa is applied to the top and bottom wall of the sample by using a servo control algorithm, while the cylinder wall boundary is fixed. The axial boundary stress of 1 MPa is first applied to the sample containing solid particles only. The water particle stiffness is then calculated from the pore pressure generation as a result of porosity change, from Equation 4.30. The calculated water particle stiffness is then applied back to the original sample with 0.1 MPa's axial boundary stress. Then the sample with both solid and water particles is subjected to an axial boundary stress increment of 0.9 MPa. The axial stress increment from 1 MPa to 4 MPa and pore pressure calculation method followed the same procedure as described in the isotropic compression case.

The analytical solution of the pore pressure buildup is calculated from Equation 4.50 to Equation 4.52.

The result of the triaxial compression test is shown in Figure 4.20: and Figure 4.21, which show good agreements between analytical and numerical results. It should be noted that during axial boundary stress increment, the boundary stress in the radial direction is not equal to stress in the axial direction due to the restraint of boundary wall, which indicates it is not an isotropic compression case. This indicates that even sample is not in an isotropic compression state, the approach used in this study still reveals the capability of simulating fluid-solid interactions under undrained condition.
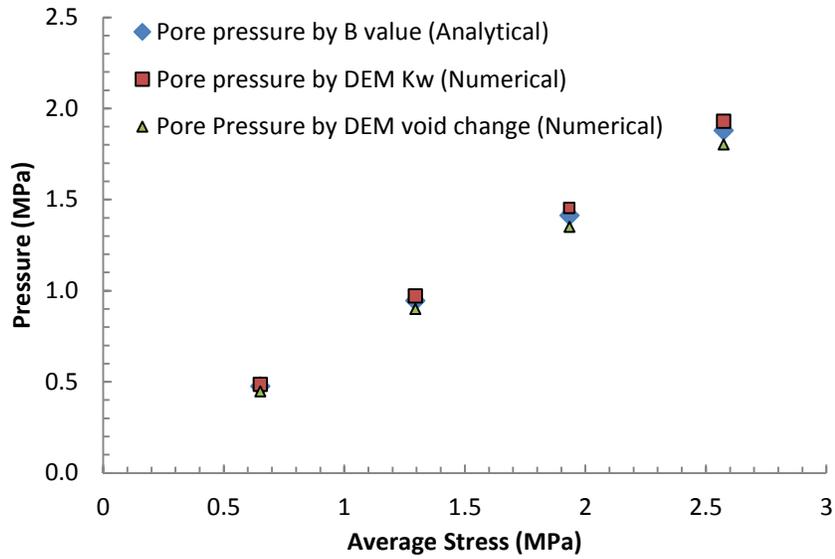
Figure 4.20: Comparison between analytical and numerical pore pressure build up against the total stress increase on boundary walls in triaxial compression case
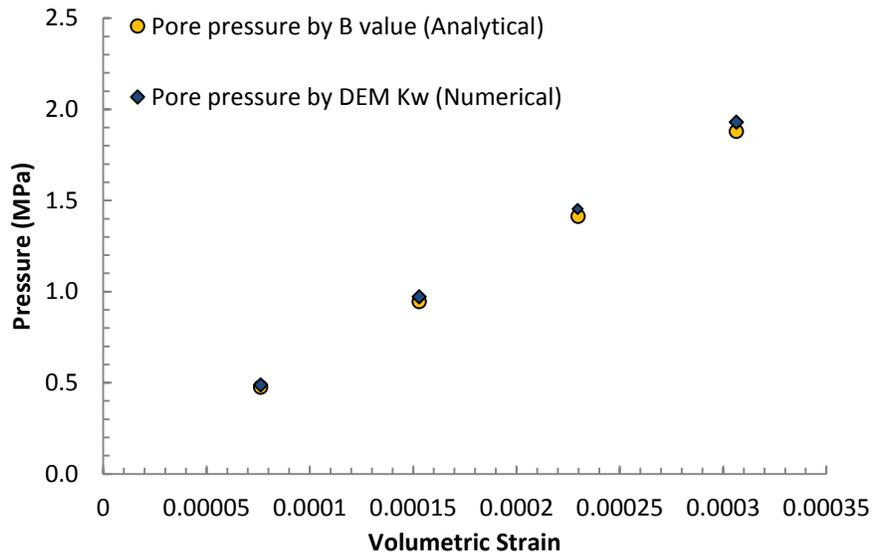

Figure 4.21: Comparison between analytical and numerical pore pressure build up against the volumetric strain of the sample in triaxial compression case

4.3.3. 1D Consolidation of Soil – Oedometer test

4.3.3.1 Loose particle packing configuration

The DEM model used in the simulation of 1D consolidation test has the minimum diameter, height and diameter-to-height ratio of 50 mm, 12 mm and 2.5, respectively (ASTM standard, 2011). In order to generate a DEM model that fit this sample size, the DEM model has the length, width and depth of 75 mm, 75 mm, and 15 mm, bounded by six frictionless rigid walls. An initial seating load of 10 kPa is applied on all the boundary producing an isotropic stress condition as shown in Figure 4.22. Although the model is 3D, forces are applied and displacements are changing only in the vertical z direction resulting in a 1D simulation. No deformation is allowed to occur in the x and y directions, but forces can develop in these 2 directions due to the restraint imposed by the boundary walls.
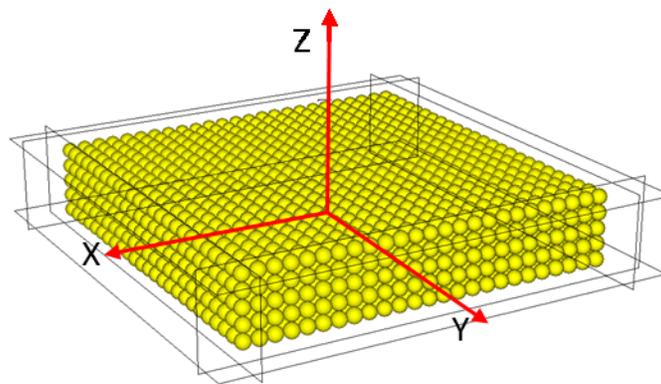
(a)
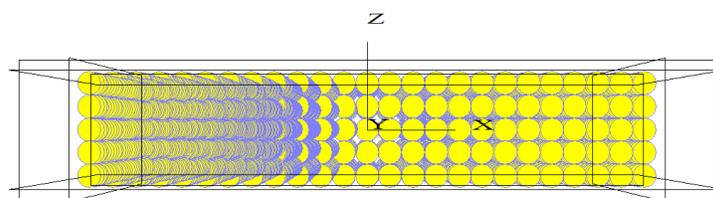
(b)

Figure 4.22: DEM generation of loose packing particles, the outer boundary stress is only applied in the z direction (a) 3D view (b) Side view.

Measurement spheres are used to calculate the porosity of the sample. The measurement spheres are evenly distributed in the sample and contain at least 5 particles inside. The porosity of the whole sample is averaged by all measurement spheres, as shown in Figure 4.23.

(a)

(b)
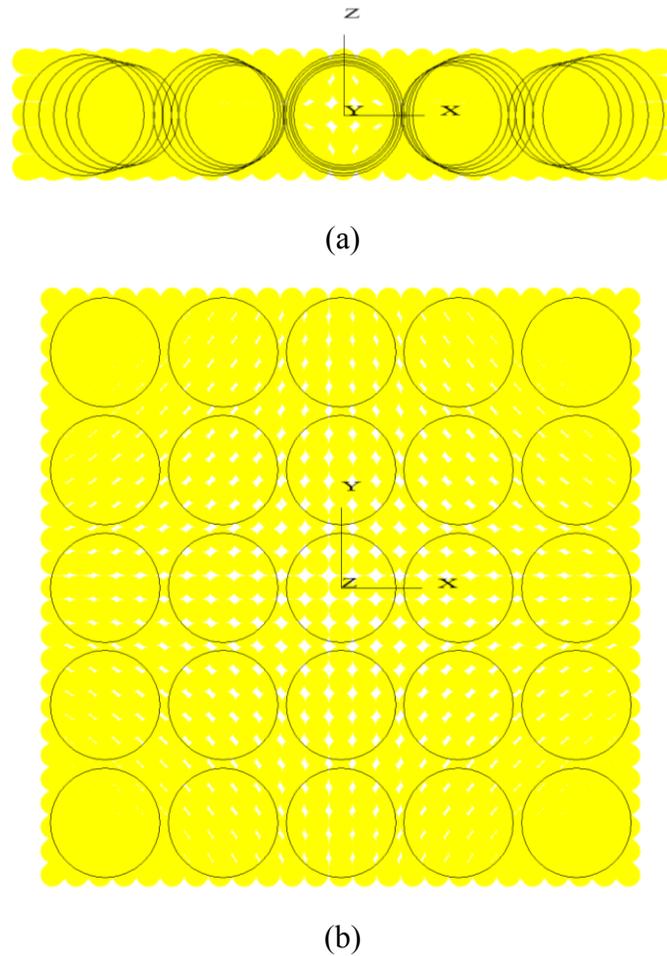
Figure 4.23: The measurement sphere distribution in the sample. (a) x-z plane view, (b) x-y plane view.

In conventional odeometer consolidation test, the specimen ring shall be stiff enough to prevent significant lateral deformation of the specimen throughout the test. Therefore, the stiffness of boundary wall is set to be equal to 5 times the particle normal stiffness. The coefficient of volume

compressibility of the soil skeleton can be calculated from DEM 1D compression on solid particles for the dry case as (Craig, 2004).

$$m_v = \frac{1}{1 + e_0} \left(\frac{e_0 - e_1}{\sigma_1' - \sigma_0'} \right) \qquad [4.60]$$

where e_0 and e_1 are the void ratios before and after stress application, and $(\sigma_1' - \sigma_0')$ is the stress increment in z direction and is chosen as 0.1 MPa in this case. The variation of the coefficient of volume compressibility based on the increasing solid particle stiffness is shown in Figure 4.24. It is observed that the coefficient of volume compressibility increases with the increase of solid particle stiffness. The final coefficient of volume compressibility is adjusted as 0.0447 with particle micro properties shown in Table 4.4.
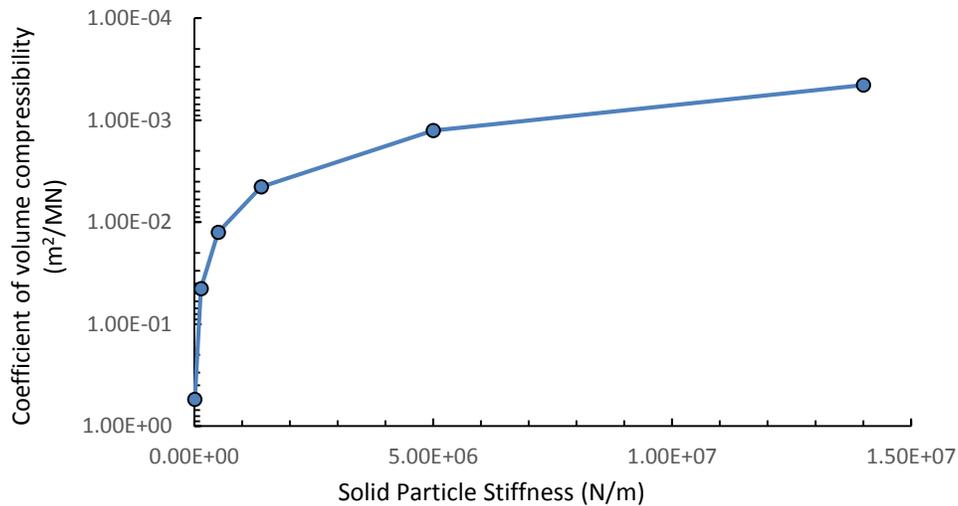
Figure 4.24: The variation of coefficient of volume compressibility base on different solid particle stiffness

Table 4.4: DEM micro properties used in oedometer test of loose packing case

Parameters	Values	Units
Sample Height (H)	15	mm
Sample Length (L)	75	mm
Sample Width (W)	75	mm
Wall Normal Stiffness (K_{nwall})	7×10^5	N/m
Wall stiffness ratio (K_{nwall}/K_{swall})	1	
Particle Normal Stiffness (K_{nball})	1.4×10^5	N/m
Particle stiffness ratio (K_{nball}/K_{sball})	1	
Particle Radius (r)	1.5	mm
Particle Density (ρ)	2650	kg/m^3
Number of Particles	3125	
Particle Friction Coefficient (μ)	0.5	
Initial Porosity	0.468	
Gravity (g)	9.8	m/s^2
Compressibility of Water (C_w)	4.6×10^{-10}	m^2/N

The process of 1D consolidation has an initial stage and a final stage being a fully undrained compression stage and final fully drained stage. The undrained compression stage first started with an application of a vertical stress in the z direction of 0.1 MPa on the sample with the solid particle only. The water particle stiffness is calculated from the pore pressure buildup because of the porosity change.

$$K_w = \frac{3V_{total}\Delta U}{\sum_{i=1}^{i=3}\sum_{N_p}\sum_{N_c^{(p)}}\left(x_i^c - x_i^p\right)(\eta D_i^n)} \qquad [4.61]$$

$$\eta = \begin{cases} \dfrac{1}{2}; & \text{for particle} - \text{particle contact} \\ \dfrac{K_{wall}}{K_w + K_{wall}}; & \text{for particle} - \text{wall contact} \end{cases} \qquad [4.62]$$

where K_w and K_{wall} are the normal stiffness of a single water particle and the wall respectively, ΔU is the pore pressure build up due to porosity change, and subscript i has a range of $i \in \{1,2,3\}$ for the components in the x, y, and z directions.

The calculated water particle stiffness is introduced in the DEM calculation, and the boundary stress of 0.01 MPa is reapplied again. Once the water elements are introduced with a finite stiffness, the sample which combines both solid and water particles will support the stress increment applied on the boundary.

Analytical solution for the consolidation test can be calculated by considering a half drained layer shown in Figure 4.25.
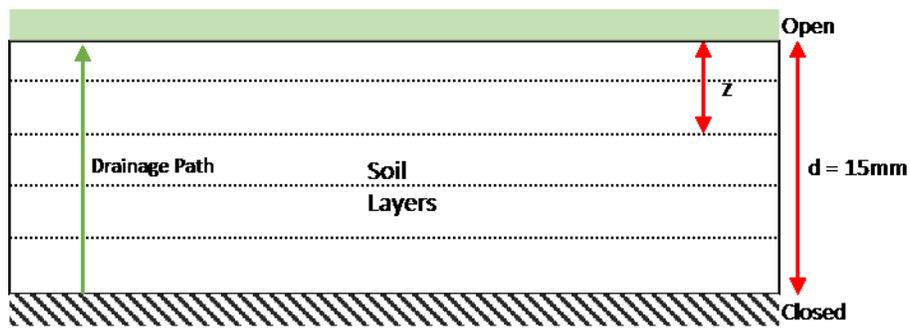
Figure 4.25: The side view of soil drainage layers for analytical solution

The excess pore pressure at any distance z from drained layer is calculated as (Craig, 2004):

$$u_e = \sum_{m=0}^{m=\infty} \frac{2u_i}{M}\left(\sin\frac{Mz}{d}\right)e^{(-M^2T_v)}$$

[4.63]

$$M = \frac{\pi}{2}(2m+1)$$

where u_i is the initial excess pore pressure, d is the drainage path, m can be any integer, T_v is time factor and is calculated as:

$$T_v = \frac{C_v t}{d^2}$$

[4.64]

$$C_v = \frac{k}{m_v \gamma_w}$$

where C_v is defined as the coefficient of consolidation, k is the permeability in clay, m_v is the coefficient of volume compressibility of soil skeleton, γ_w is the unit weight of water. The basic parameters used in the analytical 1D consolidation solution is shown in Table 4.5:

Table 4.5: Basic soil and fluid characteristics in analytical 1D consolidation test

Parameters	Values	Units
Permeability (k)	1×10^{-10}	m/s
Coefficient of volume compressibility (m_v)	0.044742398	m²/MN
Unit weight of water (γ_w)	9.81	kN/m³
Coefficient of consolidation (c_v)	2.2783×10^{-7}	m²/s
Drainage path (d)	0.015	m
Distance to open drainage (z)	Case depend	m
B value	0.99623	
Initial excess pore pressure (u_i)	0.09962	MPa

In the analytical solution, the final 1D consolidation settlement of the whole soil layer is calculated based on the change in effective stress as (Craig, 2006):

$$\Delta H_f = m_v \Delta \sigma' H \tag{4.65}$$

where $\Delta \sigma'$ is the effective stress change on the soil skeleton which is equal to 0.1 MPa in this case, and H is the length of the drainage layer which is equal to oedometer sample's depth in z direction before the beginning of dissipation process.

The consolidation settlement of the whole soil layer at any time T_v during the consolidation process is calculated by using the average degree of consolidation $\overline{U}$:

$$\Delta H = \Delta H_f (1 - \overline{U}) \tag{4.66}$$

$$\bar{U} = 1 - \sum_{m=0}^{m=\infty} \frac{2}{M^2} \exp(-M^2 T_v) \qquad\qquad [4.67]$$

The DEM calculation is divided into 5 layers for pore pressure calculation, as shown in Figure 4.26 below:
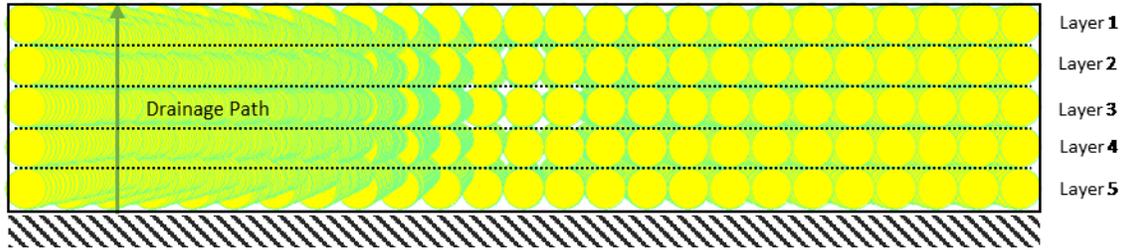
Figure 4.26: The side view of soil drainage layers for DEM calculation of loose packing case

During the drained consolidation test, the water particle stiffness is reduced from the maximum value to zero corresponding to the pore pressure decrement at each step, according to Eq. 4.41. The difference in pore pressure at a specific time along each layer in the analytical solution (Eq. 4.63) will result in different stiffness reduction in the water particles along each layer. The excess pore pressure of each layer from the DEM solution is calculated from Eq. 4.26. The consolidation settlement of the whole soil layer at any time during the consolidation process is calculated by the difference in displacement between the upper and lower wall in the z direction.

Figure 4.27 compares the particle intersection before (time = 0 s) and after the end of (time = 200 s) pore pressure dissipation. It is observed that the intersection of particle contact in z direction between layer 2 and layer 3 increase because of water particle stiffness reduction, which lead to the total volume decrease of the sample, which is consistent with the laboratory observation as expected in traditional soil mechanics.

(c)

(b)
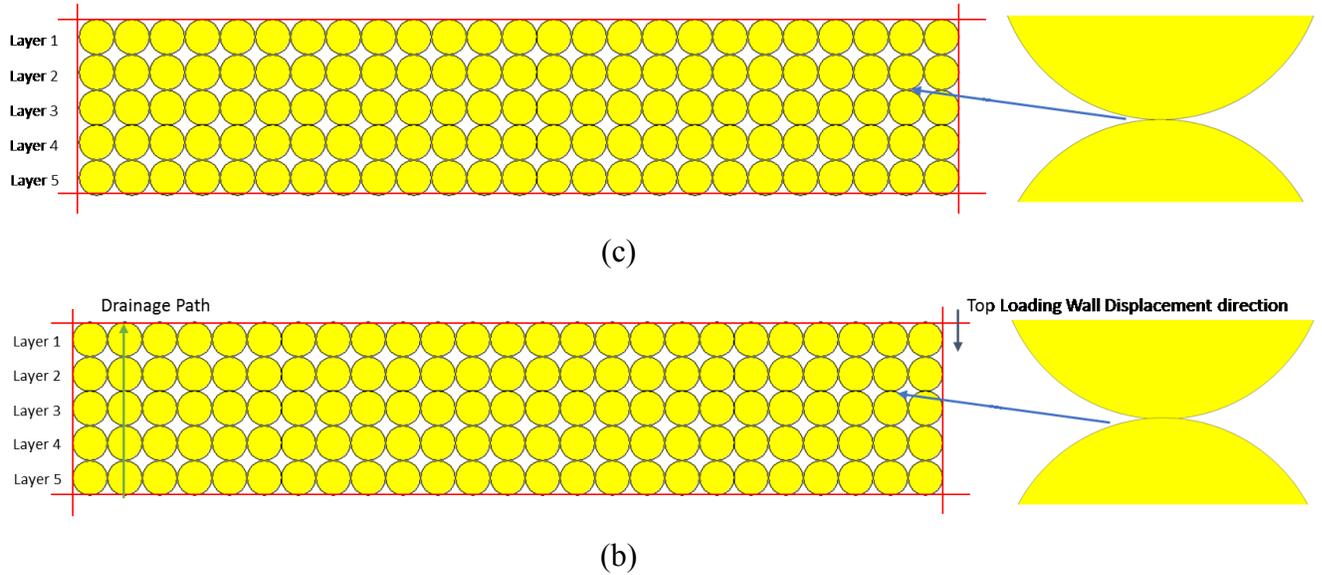
Figure 4.27: Intersection of particle contact (a) before pore pressure dissipation, time = 0 s; (b) at the end of pore pressure dissipation, time = 2000 s.

The comparison of excess pore pressure drop in each layer between the DEM and the analytical solution is shown in (e)

Figure 4.28 (a) to (e). The comparison of consolidation settlement of the whole soil sample against the time increment between analytical and DEM solution is shown in Figure 4.29. It is observed that the proposed method is able to calculate pore water pressure dissipation using the water particles with good accuracy.
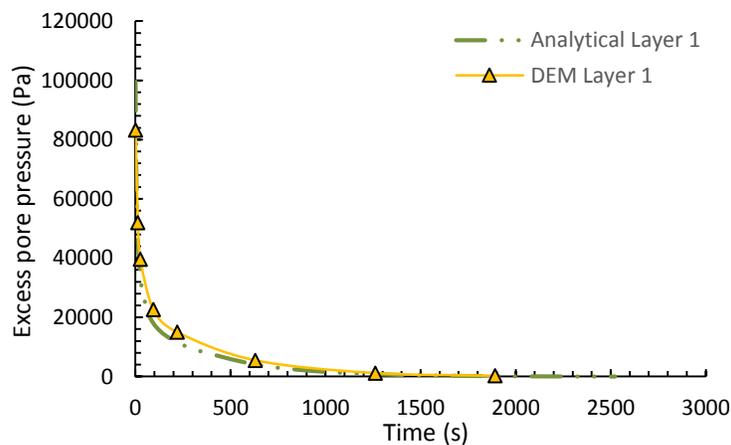
(a)
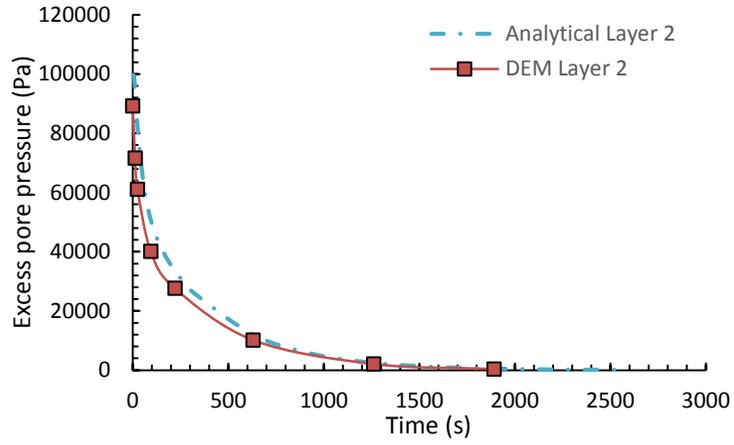
(b)
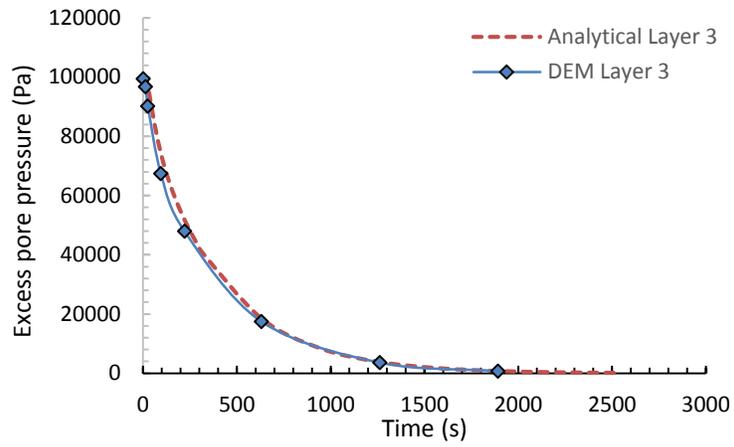
(c)
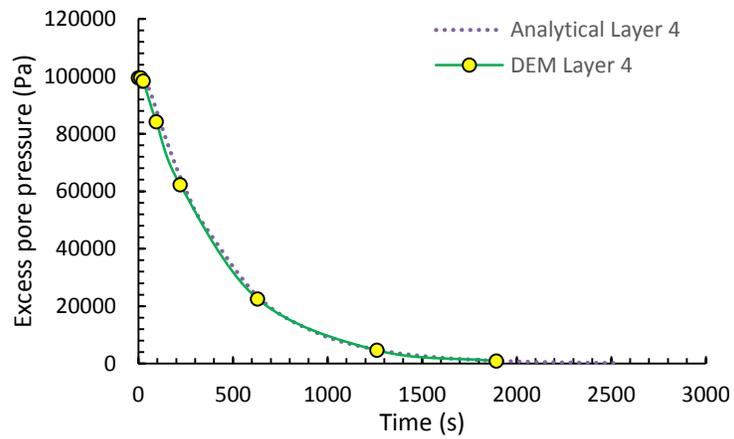
(d)
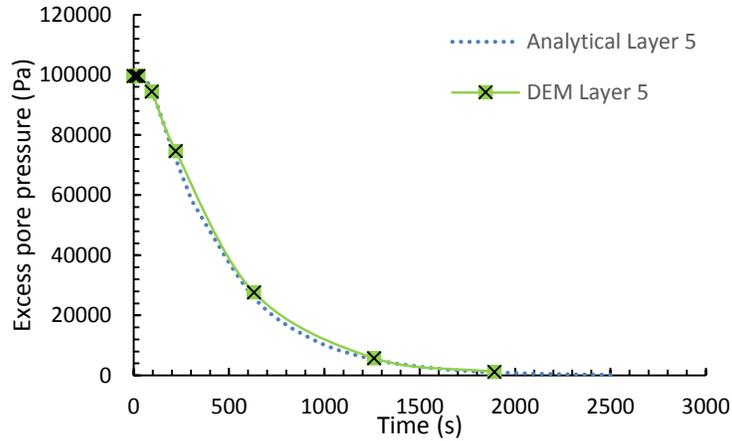
(e)

Figure 4.28: Comparison of excess pore pressure drop of each layer against time increment between analytical solution and DEM solution of loose packing case
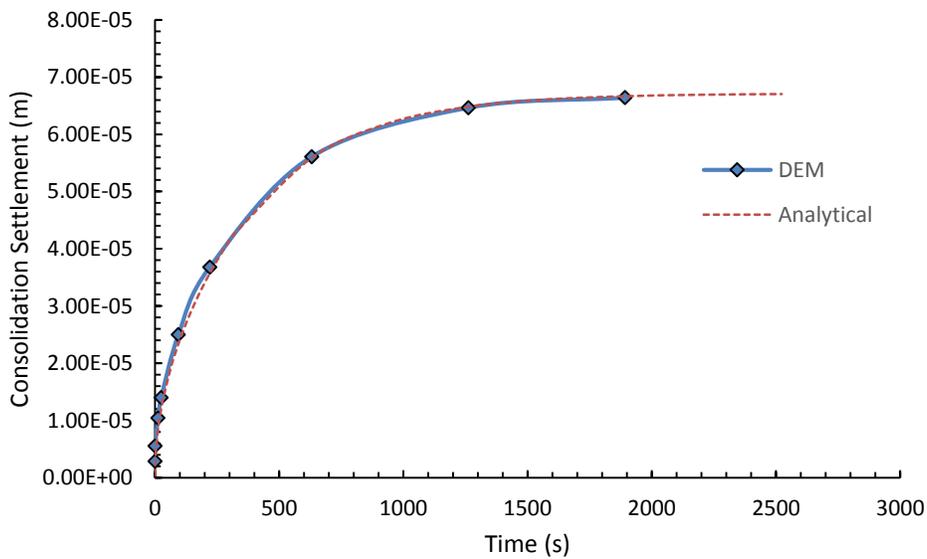
Figure 4.29: Comparison of consolidation settlement of whole soil sample against time increment between analytical solution and DEM solution of loose packing case

4.3.3.2. Irregular particle packing configuration

A DEM model is generated using uniform size irregular dense packing particles in a rectangular box with length, width and depth of 75 mm, 75 mm, and 15 mm respectively. The elements are

bounded by six frictionless rigid walls as shown in Figure 4.30. The application of load is 1D and the boundary walls in the x and y directions are fixed by setting the wall velocities to zero. The wall in z direction can move freely based on the servo control method.

(a)

(b)
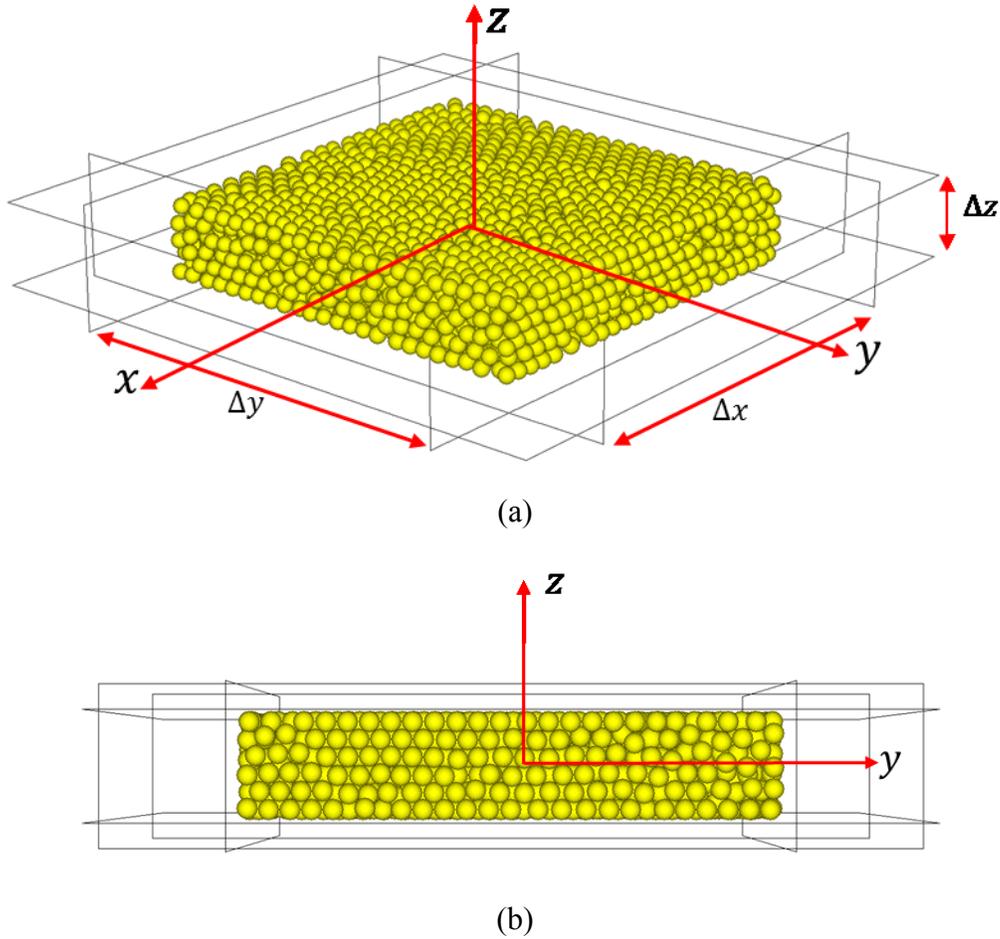
Figure 4.30: DEM generation of dense packing particles, the outer boundary stress is only applied in the z direction (a) 3D view (b) Side view.

To calculate the porosity of the sample, a more precise method is used instead of inserting the measurement sphere used in the loose packing case. From Figure 4.30: , the total volume of sample V_T is calculated as:

$$V_T = \Delta x \cdot \Delta y \cdot \Delta z \qquad [4.68]$$

where $\Delta x, \Delta y$, and Δz are the perpendicular distances between two walls in x y and z direction.

The solid volume V_s is calculated as:

$$V_s = V_b^T - V_{b-b}^T - V_{b-w}^T \qquad [4.69]$$

where V_b^T is the volume of total particles, V_{b-b}^T is the total particle-particle intersection volume, and V_{b-w}^T is the total particle-wall intersection volume. The total solid volume of all the particles is calculated from:

$$V_b^T = \sum_{m=0}^{m=N_p} \frac{4}{3} \pi r_m^3 \qquad [4.70]$$

where N_p is the total number of particles in the sample, r_m is the current particle radius. The volume of particle-particle intersection and particle-wall intersection is calculated separately and following the index notation as shown in Figure 4.31, where index i has a range of $i \in \{1,2,3\}$) for x, y, and z directions. For particle-particle contact, each volume contains only half of total intersection volume because two particles share one contact:

$$V_{b-b}^T = \sum_{N_p} \sum_{N_c} \frac{1}{2} \Big(\frac{\pi}{12d} (R^A + R^B - d)^2 [d^2 + 2d(R^A + R^B)$$

$$- 3(R^A - R^B)^2] \Big) \qquad [4.71]$$

$$d = \sqrt{\sum_{i=1}^{i=3} (x_i^A - x_i^B)^2} \qquad [4.72]$$

130

$$V_{b-w}^T = \sum_{N_p} \sum_{N_c} \frac{\pi (D_{total}^n)^2}{3} (3R^b - D_{total}^n) \qquad [4.73]$$

$$D_{total}^n = R^b - \sqrt{\sum_{i=1}^{i=3} (x_i^c - x_i^b)^2} \qquad [4.74]$$

The sample's true porosity n is then calculated from:

$$n = \frac{V_v}{V_T} = \frac{V_T - V_s}{V_T} \qquad [4.75]$$

(a)   (b)
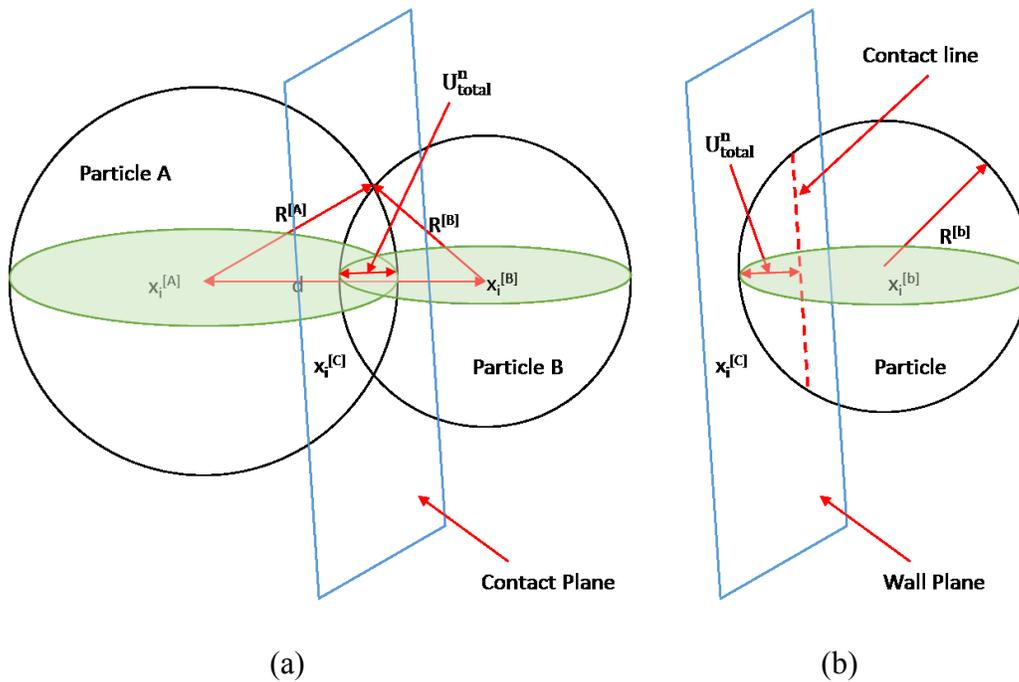
Figure 4.31: Notations used to describe (a) Particle-particle contact (b) Particle-wall contact

The coefficient of volume compressibility is adjusted following the same procedure described for the loose packing case. The particle micro properties are given in Table 4.6, and the basic parameters used in analytical 1D consolidation test is shown in Table 4.7:

Table 4.6: DEM micro properties used in oedometer test of irregular packing case

Parameters	Values	Units
Sample Height (H)	15	mm
Sample Length (L)	75	mm
Sample Width (W)	75	mm
Wall Normal Stiffness (K_{nwall})	1.5×10^6	N/m
Wall stiffness ratio (K_{nwall}/K_{swall})	1	
Particle Normal Stiffness (K_{nball})	3×10^5	N/m
Particle stiffness ratio (K_{nball}/K_{sball})	1	
Particle Radius (r)	1.5	mm
Particle Density (ρ)	2650	kg/m^3
Number of Particles	3879	
Particle Friction Coefficient (μ)	0.5	
Initial Porosity	0.389	
Gravity (g)	9.8	m/s^2
Compressibility of Water (C_w)	4.6×10^{-10}	m^2/N

Table 4.7: Basic soil and fluid characteristics in analytical 1D consolidation

Parameters	Values	Units
Permeability (k)	1×10^{-10}	m/s
Coefficient of volume compressibility (m_v)	0.036636473	m^2/MN
Unit weight of water (Υ_w)	9.81	kN/m^3
Coefficient of consolidation (c_v)	2.7824×10^{-7}	m^2/s
Drainage path (d)	0.015	m
Distance to open drainage (z)	Case depend	m
B value	0.9952	
Initial excess pore pressure (u_i)	0.0995	MPa

The DEM calculation procedure follows the same process and same boundary stress (0.1 MPa in the z direction) as the loose packing case. During the dissipation process, the DEM calculation is divided into 3 layers for pore pressure calculation, see Figure 4.32. The pore pressure of each layer is first calculated based on the time from Eq. 4.63. The water particle stiffness is then calculated from Eq. 4.46 and applied on each particle until convergence has reached using the iteration

algorithm as shown in Figure 4.9: . The iteration for β using the bisection method continues until convergence is satisfied as defined in Eq. 4.49.

The excess pore pressure of each layer from the DEM solution is calculated from Eq. 4.26. The consolidation settlement of the whole soil layer at any time during the consolidation process is calculated by calculating the difference in displacement between the upper and lower wall in the z direction.
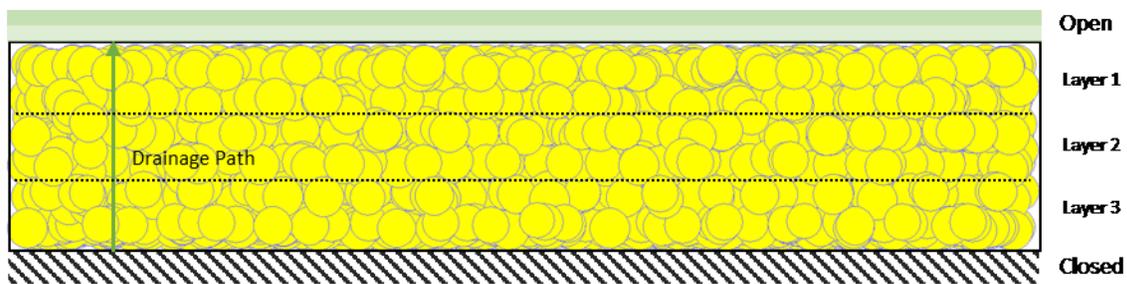
Figure 4.32: The side view of soil drainage layers for DEM calculation of irregular packing case

Figure 4.33 compares the excess pore pressure in each layer between the analytical and DEM solutions. The comparison of consolidation settlement of whole soil sample with time is shown in Figure 4.34. It is observed that the analytical and numerical solutions agree well for both pore pressure and displacement changes with time. The accuracy of these simulations reveals the capability of this algorithm to capture solid-fluid interactions.

(a)

(b)

134
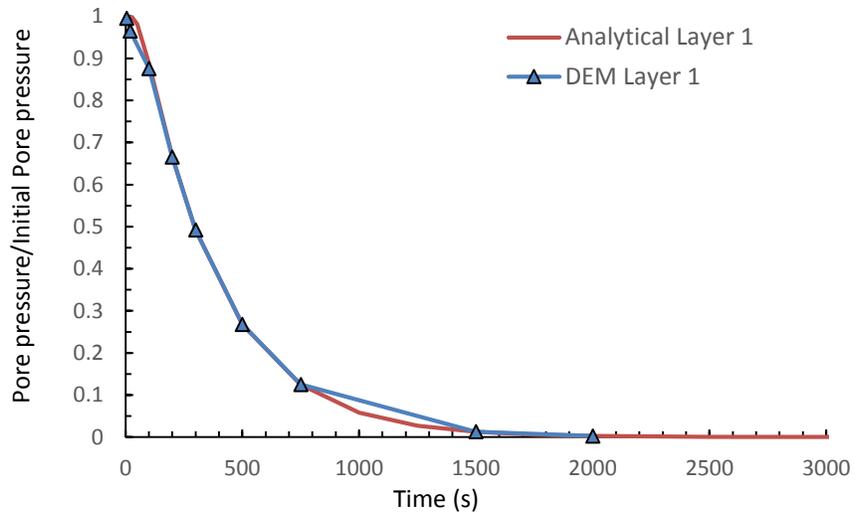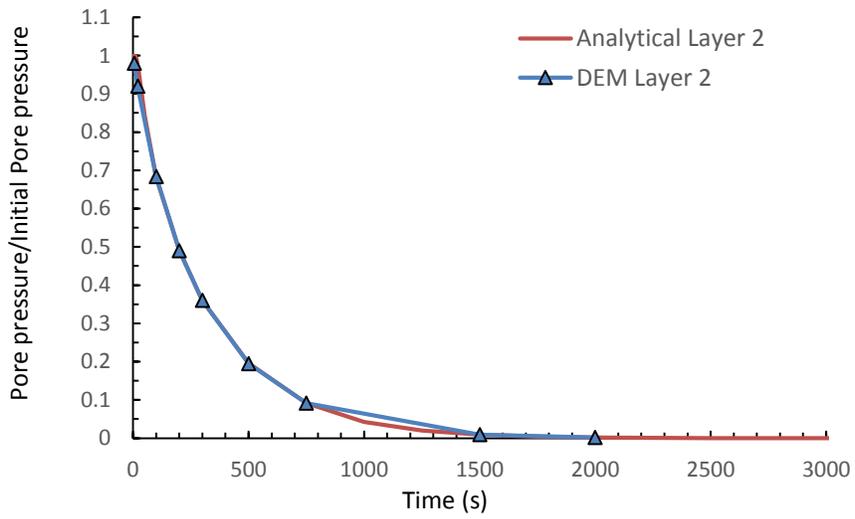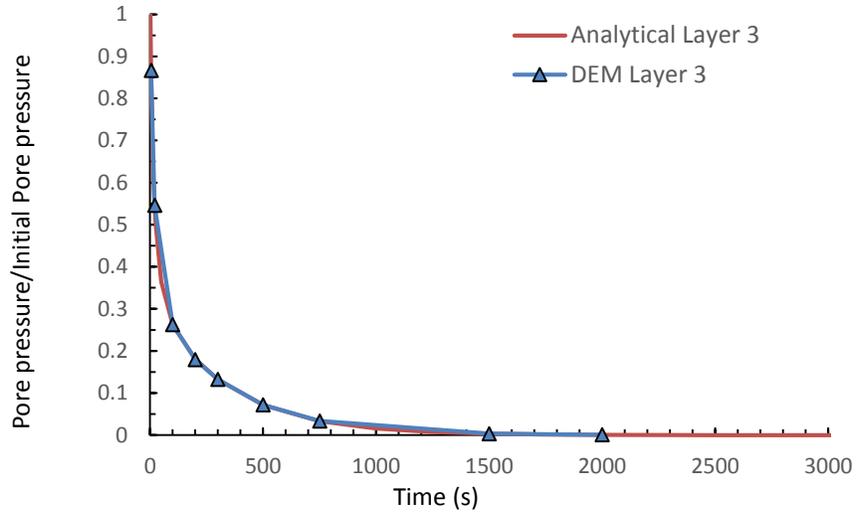
(c)

Figure 4.33: Comparison of excess pore pressure/initial pore pressure of each layer against time increment between analytical solution and DEM solution of irregular packing case
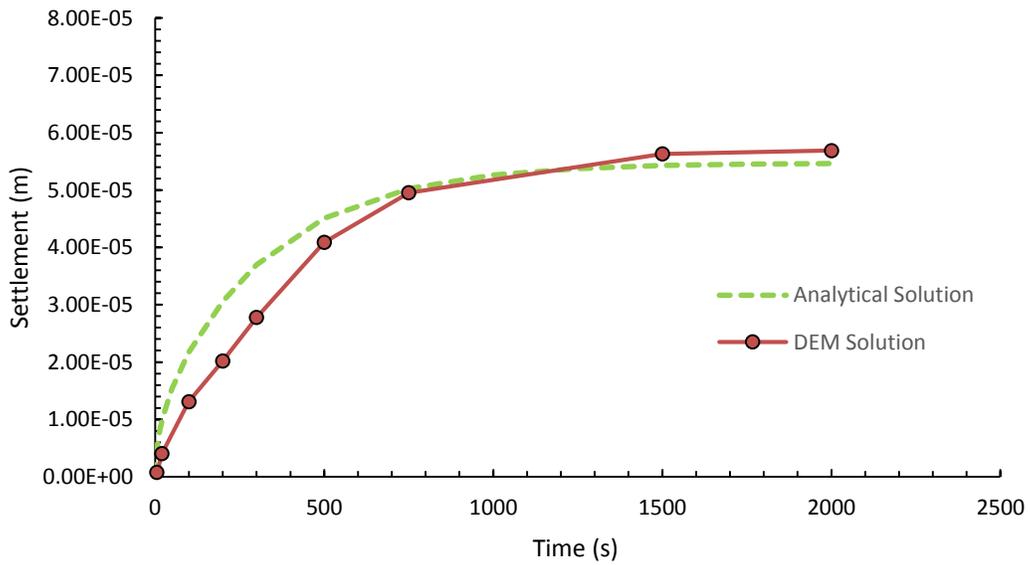
Figure 4.34: Comparison of consolidation settlement of whole soil sample against time increment between analytical solution and DEM solution of irregular packing case

4.4. Conclusion

In this Chapter, a new method has been presented to model solid-fluid interaction in DEM analysis. The pore pressure build-up due to solid deformation is captured using a DEM water element, which occupies the same position and has the same deformation as the solid element. The water element stiffness (micro) is calculated based on changes in pore space and the compressibility of water (macro). Two examples have been presented to demonstrate the approach and check the accuracy of the algorithm. The comparison between the numerical and analytical results shows that this continuum-discrete model can accurately capture the deformation of water saturated densely packed particles. During the dissipation process, pore pressure changes is simulated by reducing the water particle stiffness calculated from pore volume reduction. The bisection method is used to calculate the correct water particle stiffness for a specified pore pressure in each particle. Analytical solutions based on traditional soil mechanic theory for the oedometer test is used to validate the proposed algorithm. Comparison between numerical and analytical results show that the DEM model not only can replicate saturated loosely packed particles deformation but also can capture densely packed particle deformation accurately.

Chapter 5. Simulations of Consolidated Undrained Triaxial Test

5.1. Introduction and Background

The undrained condition of saturated sand has been studied widespread since the original work from Bishop and Eldin (1950, 1953). Laboratory consolidated undrained tests have been performed by past researchers to study the volume change (Newland and Alley, 1959), void ratio change (Been and Jefferies, 1985), and stress path (Vaid et al., 1990; Vaid et al., 1996). Although lots of data have been collected, the undrained behavior of granular material with pore fluid has not been modelled using a discrete approach.

The traditional numerical analysis using continuum model may not sufficiently explain the undrained behavior of sand because the assumption of continuum model is constitutive for the sample's macroscopic behavior and such assumption is unable to provide information at the grain scale (Gong et al., 2012). Such disadvantage can be overcome by introducing the discrete element method (DEM). The DEM simulation of the undrained behavior of loose soil was carried out by Thornton and Barnes (1986), Kishino (1990), Ng and Dobry (1994), Sitharam et al. (2002), Zhang (2003), and Gong (2008) by imposing the constant volume condition in undrained deformation. However, most published DEM research in geomechanics consider dry granular materials at the microscale, which means even simulation of the undrained test is performed in a vacuum without fluid. In principle, the model of fluid phase and how the fluid and particle interact with each other is necessary.

The accumulation of excess pore water pressure is caused by soil deformation due to the changes in the mechanical boundary conditions. Excess pore water pressure can lead to the loss of shear

strength and particles contacts resulting in plastic deformations. Therefore, the existence of excess pore pressure during undrained condition cannot be ignored in DEM simulation.

Hakuno and Tarumi (1988) developed a method to model liquefaction based on detecting all the pores among particles and connecting them by pipes. The pore water pressure was calculated by assuming water had constant volume elasticity and the water pressure was proportional to the pore volume. Fluid flow between each pore space and its adjacent pores was calculated based on Darcy's law. This method resulted in a complicated calculation procedure and required subsequent manipulation. Nakase et al. (1999) improved Hakuno and Tarumi's method by implementing square-cell element each containing 15 particles. The pore pressure generation in each cell corresponded to particle movement in the neighboring cells and was proportional to the decrease of pore volume. The fluid force applied on the particle was depended on the pore pressure gradient between neighbor cells. Mori et al. (2001) studied the liquefaction analysis of River Dike using a two-dimensional discrete element model. In their study, the excess pore water pressure was considered to estimate large permanent displacement due to liquefaction at the microscope level. The accumulative excess pore water pressure caused by the combination of shear force and the effective normal force was equal to the initial effective normal force. The excess pore water pressure caused by the shear force was related to the dissipative energy and stored elastic energy of the model. Bonilla (2004) performed a DEM undrained simulation with fluid coupling by using two-dimensional assemblies of elliptical particles. The pore volume was identified by constructing a polygon around the specified pore surrounded by particles. The volumetric pore changed experienced due to particle rearrangement under external forces is then calculated from volume change of the polygon. The pore pressure change was then calculated from pore volume change. The fluid flow path was constructed by flow network which joining the center of polygons. The

pore pressure force on particles is applied by integration method of pore pressure difference on the adjacent center of polygons. Bonilla observed the temporary liquefaction in DEM simulations. From Bonilla's recommendations, the computational efficiency of such method is still need to be improved.

In this Chapter, a new idea is proposed to incorporate excess pore water pressure calculation in DEM simulation by introducing a new water particle element which has a specific stiffness that enables the calculation of excess pore pressure due to pore space deformation. The numerical simulation of three-dimensional (3D) DEM of undrained compression test on the sand sample with different porosity at the end of consolidation is then carried out. In the following section, brief details of the simulation are given, and DEM results are presented in the following section, and the main conclusions are summarized in the final section.

5.2. Formulation of Model

In DEM analysis of sample under undrained compression case, a DEM water element is introduced here which occupies the same position and has the same deformation as the solid element; the total stress is divided into two parts: effective stress and pore pressure. The details of the formulation of the model are shown in Chapter Solid Deformation Pressure Coupling.

5.3. Model Application

5.3.1. Calibration of the micromechanical parameters

In the DEM models, the micro-properties cannot be determined by direct measurements of the macro responses on the laboratory specimens. The set of DEM input parameters required to capture the macro-scale response of the sample was selected using the existing knowledge in the literature

and methodological trial and error to match the DEM response with the laboratory measurements. The calibration was validated against a series of triaxial tests performed on Syncrude sand.

In the current simulation, a uniform particle size distribution with maximum to minimum particle radius ratio of 15 is chosen, which approximately captures the particle size distribution of Syncrude sand, shown in Figure 5.1.
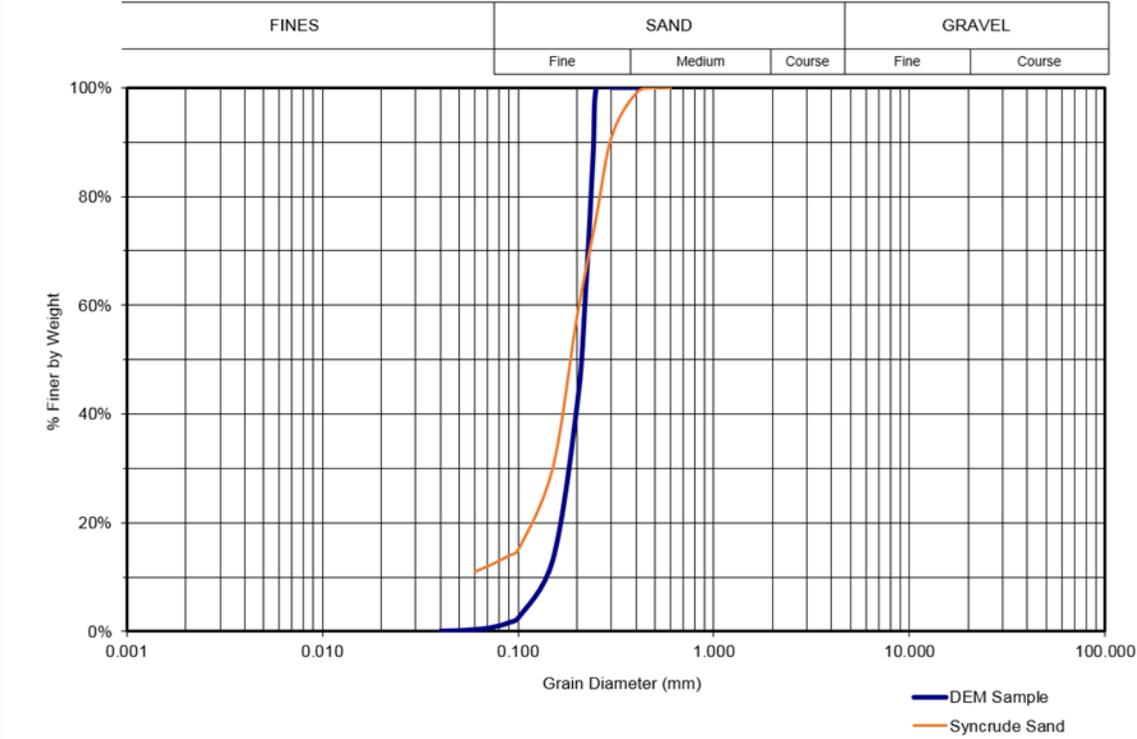
Figure 5.1: Comparison between the actual Syncrude sand and DEM specimen particle size distribution.

In the laboratory test, the specimen for the triaxial test is cylindrical with dimensions of 60 mm diameter and 120 mm height. However, too many particles will be generated in such size of the sample and make the computation speed too slow. The final DEM sample size is set as 1/20 of the original one in order to increase the calculation speed. The DEM particles were generated randomly in a cylinder of 1.5 mm radius and 6 mm height bounded by rigid walls. To ensure initial tight packing, the radial expansion method is used in particle generation. A population of particles

140

with artificially small radii is created within the specified volume. The particles are then expanded with zero friction until the desired porosity is obtained (Itasca, 2008). The particle assembles during initial generation stage is shown in Figure 5.2.
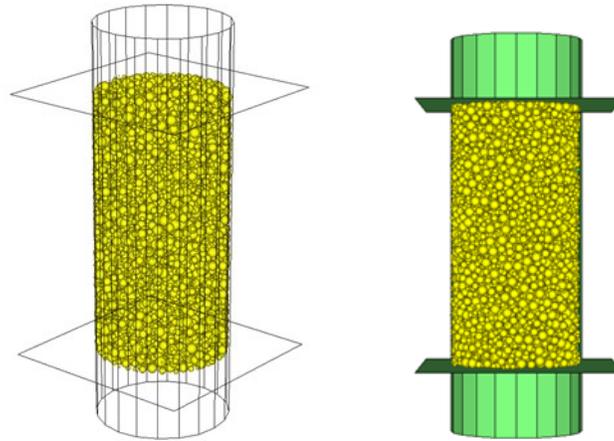
Figure 5.2: Triaxial test specimen at initial particle generation stage

The next step is to perform consolidation by compacting the particle using the servo control method in order to reach the designed compression stress in radial and vertical direction and specified porosity at the end of consolidation. For the densest sample, a gravity of 9.8 m/s^2 is first applied to all particles in the minus z-direction; then a shaking process is carried out by moving the cylindrical wall in the horizontal x-direction back and forth until the large voids are filled with small particles. The shaking process is done by setting a shake velocity to the cylindrical wall in the x direction. Meanwhile, both top and bottom wall are maintained steady during the shaking process.

To obtain the loosest sample, particle rotations were restricted in x, y and z directions before the consolidation compression stage. This is because the assembly behaves stiffer and more resistant to compression without particle rotation (Gong, 2008). The shaking process is not applied before the consolidation compression stage. In this way, a very loose sample can be prepared. For other

medium loose samples, the shaking velocity is adjusted to obtain a sample with the required porosity. Figure 5.3 shows that the DEM calculated porosity using measurement spheres at the end of the consolidation stage behaves with shaking velocity during shaking stage where porosity at particle generation stage is controlled as 0.67 by radial expansion method. It is observed that the porosity at the end of consolidation will drop and become steady with the increase of the shaking velocity. The maximum shaking velocity is then chosen as 30 m/s based on the results of Figure 5.3. However, the porosity ranges from 0.395 to 0.418 in this case. In order to prepare different samples with porosity in a larger range and compare to laboratory results, the initial porosity during particle generation was varied, by coupling different shaking velocity, to give a range of values from 0.34 to 0.425. The EDM calculated porosity at the end of the consolidation stage is shown in Figure 5.4.
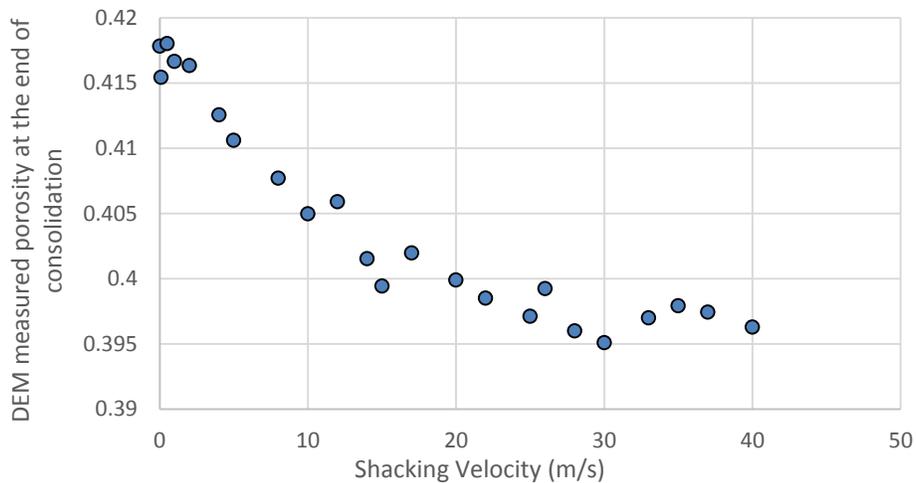
Figure 5.3: DEM measured porosity at the end of consolidation stage behaves with shaking velocity during shaking stage, initial porosity at particle generation is 0.67.
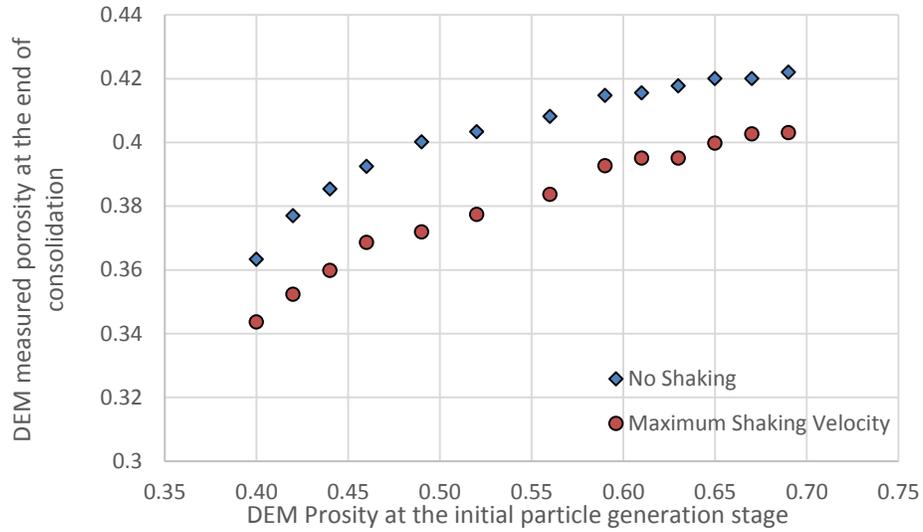
Figure 5.4: DEM measure porosity at the end of consolidation stage behaves with DEM porosity at the initial particle generation stage under different shaking conditions.

From the laboratory test results (Vaid et al. 1996), there are two sets of triaxial drained test with different porosity at the end of consolidation, which is shown in Table 5.1. The calibration method is mainly based on findings from Potyond and Cundall (2004): (1) The macro Young's modulus of the specimen is mainly governed by the particle Young's modulus. (2) The Poisson's ratio the sample is influenced by the packing geometry and ratio of shear to normal contact stiffness. (3) The particle friction coefficient mainly governs the peak and post-peak behavior.

Table 5.1: Laboratory triaxial drained test data (from Vaid et al. 1996)

Specimen Number	FS1 C9B 1	FS5 C13 1
Initial void ratio e_i	0.759	0.817
B value %	100	100
Void ratio after thawing under σ'=20kPa e_{20}	0.702	0.752
Vertical consolidation stress σ_{vc} (kPa)	540	540
Radial consolidation stress σ_{hc} (kPa)	270	270
Void ratio at the end of consolidation e_c	0.684	0.730
Contraction/Dilation (C/D)	D	D

143

The DEM triaxial test was performed in two stages: anisotropic consolidation and deviatoric loading. The anisotropic confining pressure was applied at all boundaries using a servo control algorithm in order to match laboratory consolidation conditions. Then the top platen was moved downward at a velocity of 0.01 m/s to keep the quasi-static condition while the base platen remained stationary. The radius of the cylindrical wall in the DEM model could be increased or decreased using a servo control system to maintain a constant lateral confining pressure. During the loading process, stresses were calculated by using the contact force between particle and wall and area of wall face. Strains were calculated by using the top wall position. The DEM simulation was stopped when the axial strain reached the designed value.

The calibration of the DEM model parameters was based on trial and error and comparison of laboratory and simulated triaxial drained tests. The final set of DEM micro-parameters found to capture the overall behavior of Syncrude sand is summarized in Table 5.2. Figure 5.5 and Figure 5.6 compares the macro responses of the 3D DEM model under same confining stress but different porosity at the end of consolidation, with the corresponding laboratory results. The 3D DEM model for Syncrude sand reasonably captures the initial elastic response, the peak stress and part of the post-peak behavior observed in physical laboratory test results.

Table 5.2: Syncrude sand micro properties, calibrated from laboratory triaxial drained test

Parameters	Values	Units
Wall Normal Stiffness (K_{nwall})	$0.1 \times K_{nball(avg)}$	N/m
Wall stiffness ratio (K_{nwall}/K_{swall})	1	
Particle Young's modulus (Ec)	5.5×10^7	Pa
Particle stiffness ratio (K_{nball}/K_{sball})	1	
Particle Friction Coefficient (μ)	0.3	
Particle Maximum Radius (r_{max})	0.15	mm
Particle Minimum Radius (r_{min})	0.01	mm
Particle Density (ρ)	2650	kg/m^3
Porosity at end of consolidation (n)	Case Depend	
Gravity (g)	9.8	m/s^2
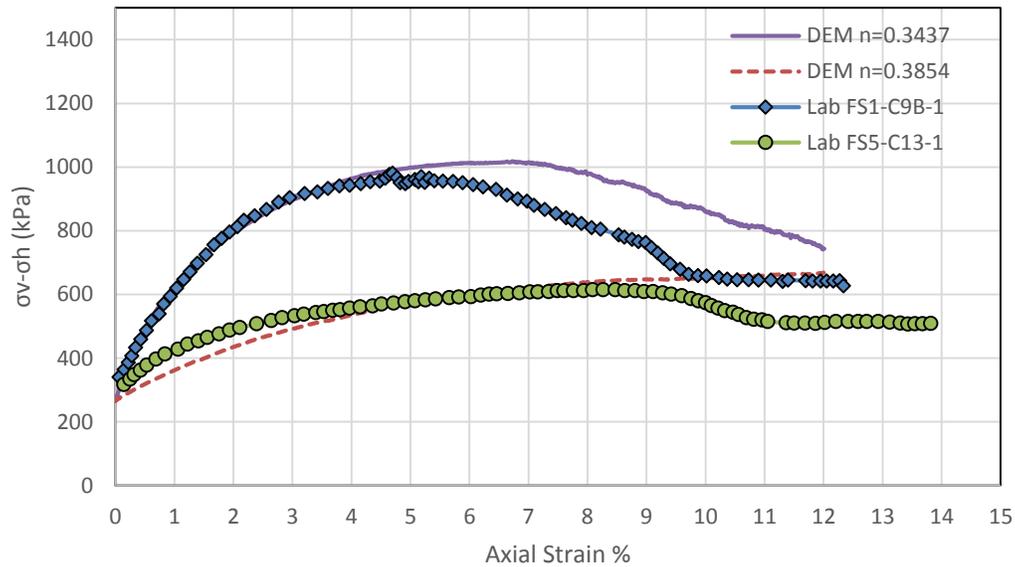
Figure 5.5: Comparison of deviatoric stress versus axial strain between triaxial drained data and numerical simulation, the DEM simulation is based on different porosity measured at the end of consolidation stage.
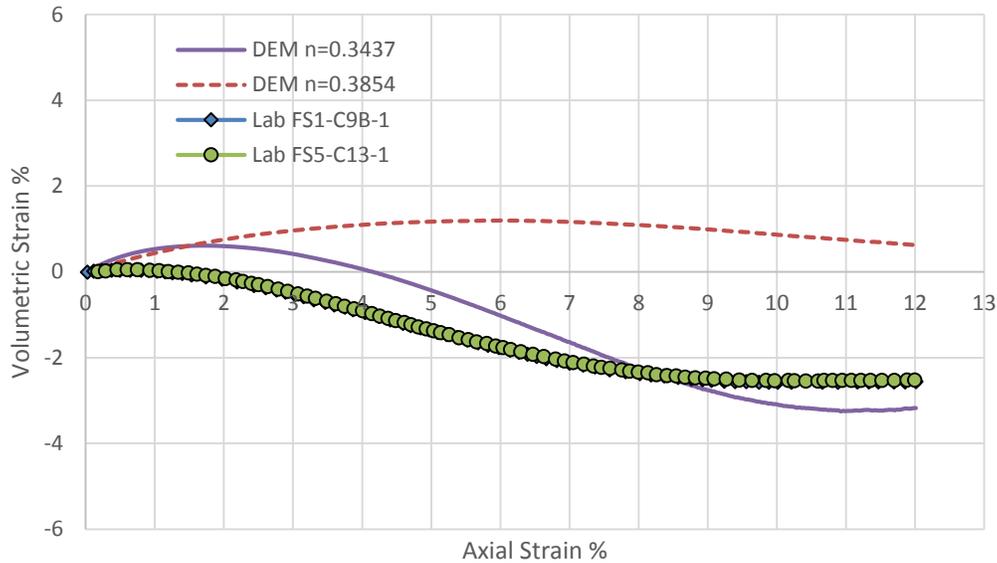
Figure 5.6: Comparison of volumetric strain versus axial strain between triaxial drained data and numerical simulation, the DEM simulation is based on different porosity measured at the end of consolidation stage.

5.3.2. Simulation of Undrained Test

5.3.2.1. Model Geometry and simulation procedure

Vaid et al. (1996) performed several sets of consolidated undrained triaxial test on Syncrude sand based on different porosity and confining pressure at the end of consolidation. The laboratory deviatoric stress – axial strain response behaved as strain hardening. The excess pore pressure at the beginning of the test increases with the increase of axial strain. However, after the phase transformation (PT) point, defined by Ishihara et al. (1975), the excess pore pressure decreases and becomes negative, changing from contractive to dilative behavior. All the laboratory results show a dense sand behavior.

One set of the laboratory triaxial undrained test is chosen based on similarity of test condition and the void ratio at the end of consolidation to give a numerical explanation. The laboratory detail is concluded in Table 5.3.

Table 5.3: Laboratory triaxial undrained test data (from Vaid et al. 1996)

Specimen Number	S6-2
Initial void ratio e_i	0.703
Void ratio after thawing under σ'=20kPa e_{20}	0.714
Vertical consolidation stress σ_{vc} (kPa)	400
Radial consolidation stress σ_{hc} (kPa)	400
Void ratio at the end of consolidation e_c	0.697
Contraction/Dilation (C/D)	D

The DEM particle generation and preparation until the end of the consolidation stage are the same as described in the calibration section. The DEM material micro properties are the same as in drained test, from Table 5.2. The DEM porosity of the sample at the end of consolidation is calibrated from triaxial drained laboratory results using linear interpolation method between laboratory and DEM porosity at the end of consolidation, shown in Figure 5.7 below:
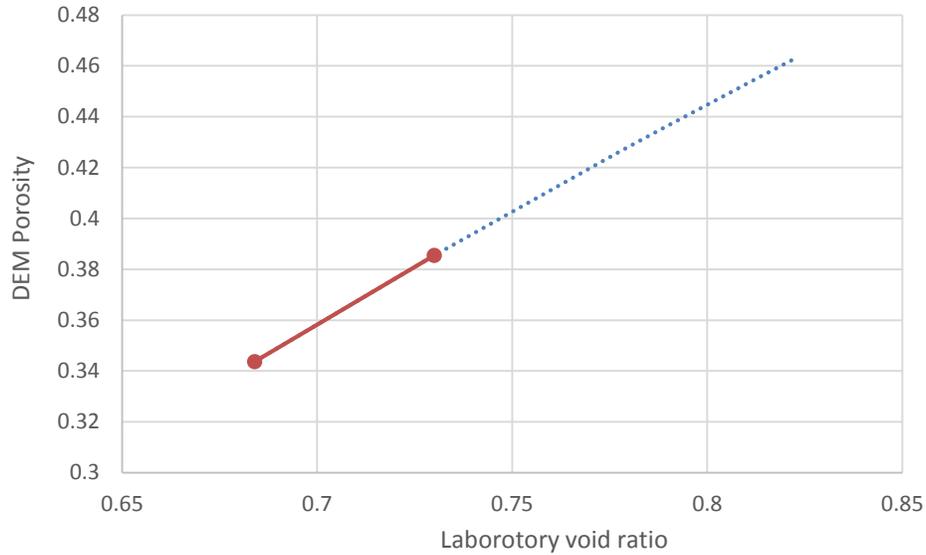
Figure 5.7: Linear correlation between laboratory void ratio and DEM porosity at the end of consolidation stage

Based on the laboratory undrained void ratio of 0.697 in Table 5.3, the DEM porosity at the end of consolidation stage is then calculated as 0.352.

Two measurement spheres are then inserted into the center of upper and lower part of the sample before the start of the undrained test, shown in Figure 5.8. The porosity change of the sample is calculated by the average readings from two measurement spheres. Adaptive measurement sphere is used during the whole calculation process, which means that the center and radius of measurement sphere is varied based on the sample's height and radius during each of iteration.
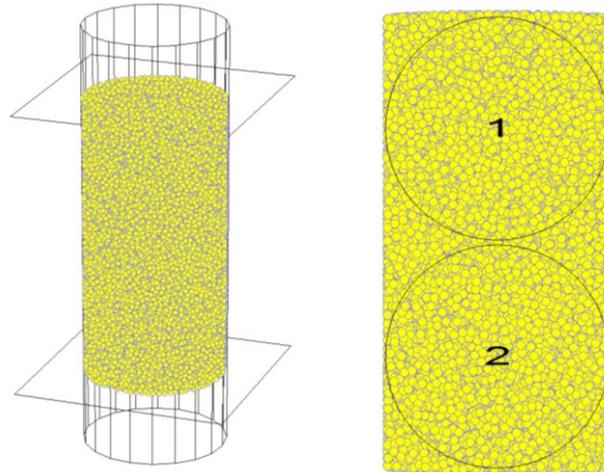
Figure 5.8: Discrete element model of the triaxial undrained compression example and measurement sphere locations.

The DEM pore pressure coupling triaxial undrained test use the axial strain controlled method instead of deviatoric stress controlled method. A continuous total axial strain increment from 0% to 12% on the sample is applied by applying a velocity of a velocity of 0.01 m/s on top confining wall in steps (by following laboratory observation). An axial strain of 0.05% is first applied on the sample with the solid particle only since the water particle stiffness is calculated from the pore pressure buildup due to porosity change. The calculated water particle stiffness is then applied back to the original sample with 0% axial strain. Then both solid and water particles are activated, and both particles experienced an axial strain increment of 0.05%. The water particle stiffness in the next axial strain increment, from 0.05% to 0.1%, will be adjusted based on the pore pressure increase difference of the current load increment.

The DEM calculation algorithm is shown in Figure 5.9. The calculation stage follows the numerical order starts from stage 1, when calculation goes to stage 9, it starts the iteration back from stage 5 until the axial strain reaches the designed value.
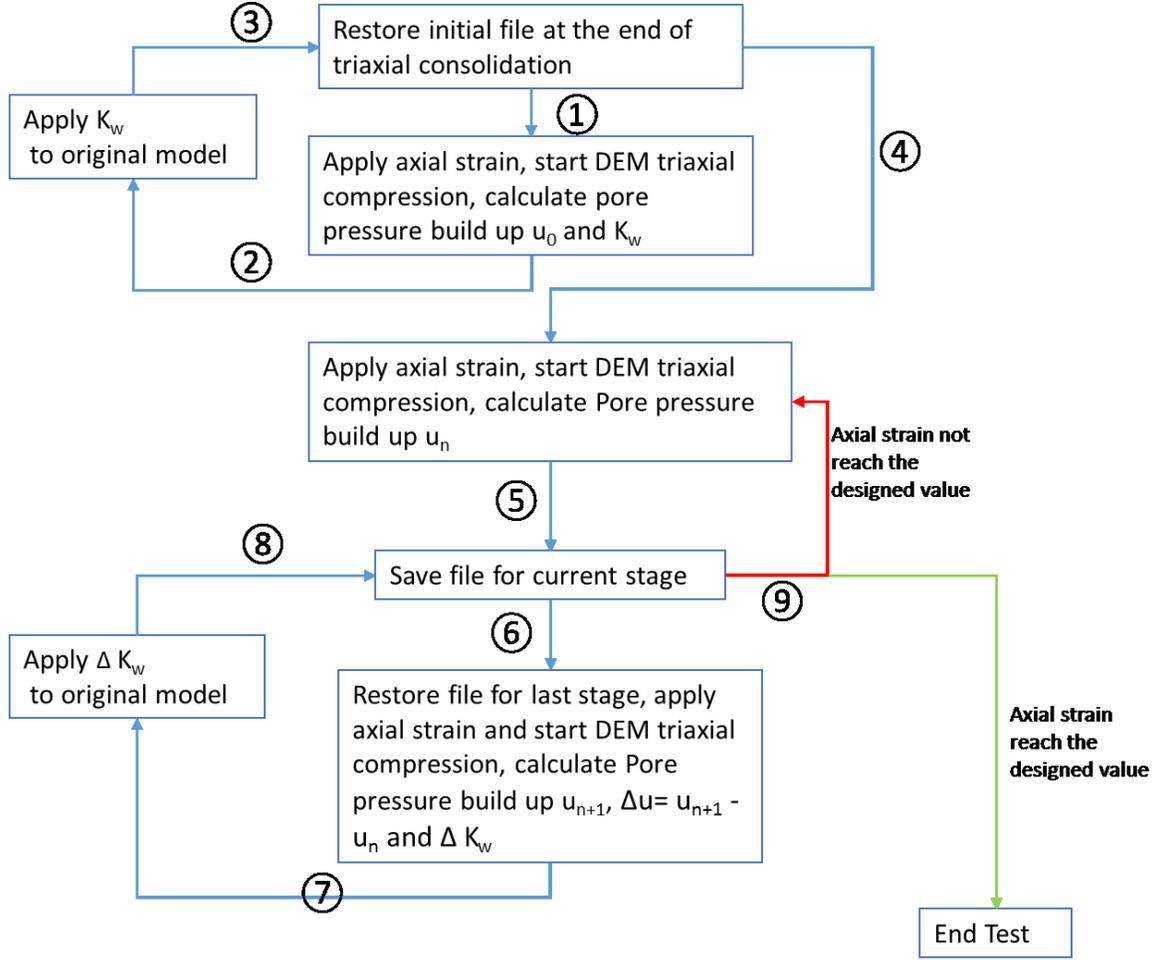
Figure 5.9: The calculation algorithm of DEM coupled with pore pressure generation in consolidated triaxial undrained test

During the iteration process, for each individual particle m, average pore pressure $\overline{u_{(m)}}$ carried by water stiffness, is calculated as:

$$\overline{u_{(m)}} = \frac{1}{3}\left(\sum_{i=1}^{i=3} u_{(m)ii}\right) \qquad [5.1]$$

$$u_{(m)ii} = \frac{1 - n_{avg}}{V_m^{(p)}}\left[\sum_{N_c}\left(x_i^{(c)} - x_i^{(p)}\right)K_{w(c)}\eta D_i^n\right] \qquad [5.2]$$

150

where $V_m^{(p)}$ is the volume of individual particle, $K_{w(c)}$ is the water stiffness at a contact between two particles, N_c is the number of contact around particle m, $x_i^{(p)}$ is the location of the centroid of particle m, $x_i^{(c)}$ is the location of the contact around that particle, index i and with range set $i \in \{1,2,3\}$ defines the calculation in x, y, and z direction, and n_{avg} is the average porosity of the whole sample. The Equation 5.1 ensure pore pressure of a particular particle m is the same in all x, y and z direction.

The effective stress, carried by solid particles, cannot be calculated directly from solid stiffness and contact intersections because the contact intersection is different in x, y, and z-direction. However, the calculation of pore pressure assumes the contact intersection is the same in x, y, and z-direction by using average method. In order to maintain system equilibrium, the effective stress in three principle direction is calculated individually from pore pressure and total stress carried combined stiffness K_T:

$$\sigma'_{(m)ii} = \frac{1 - n_{avg}}{V_m^{(p)}} \left[\sum_{N_c} (x_i^c - x_i^p) K_c \eta D_i^n \right] - \overline{u_{(m)}} \qquad [5.3]$$

$$K_T = K_{s(c)} + K_{w(c)} \qquad [5.4]$$

where $K_{s(c)}$ is the combined solid stiffness at a contact.

The average pore pressure and effective stress on three principle direction x, y, and z of the whole sample is then averaged by total number of particles:

$$\bar{u} = \frac{\sum_{N_p} \overline{u_{(m)}}}{N_p} \qquad [5.5]$$

151

$$\overline{\sigma'_u} = \frac{\sum_{N_p} \sigma'_{(m)ii}}{N_p}$$

[5.6]

The deviatoric stress recorded is then calculated from effective stress in z and r direction:

$$\sigma'_{dev} = \overline{\sigma'_z} - \overline{\sigma'_r}$$

[5.8]

$$\sigma'_r = \frac{\overline{\sigma'_x} + \overline{\sigma'_y}}{2}$$

[5.9]

where $\overline{\sigma'_x}$, $\overline{\sigma'_y}$, and $\overline{\sigma'_z}$, are effective stress of the whole sample in x, y, and z direction, calculated from Equation 5.6.

5.3.2.2. Results and Discussion

The effective of compressibility of water (in a unit of m^2/N) is first studied by a serious of sensitivity analysis. The results of sensitivity study are shown in Figure 5.10. It is observed that the sample's peak strength and modulus before peak stage are not influenced by the compressibility of water (Figure 5.10 a). However, from Figure 5.10 b, the peak generated pore pressure increase with the decrease of the compressibility of water. The pore pressure after peak stage will drop more flatten with the higher compressibility of water. The compressibility of water is then chosen as 3.0e-07 m^2/N in order to match the laboratory maximum pore pressure.

152
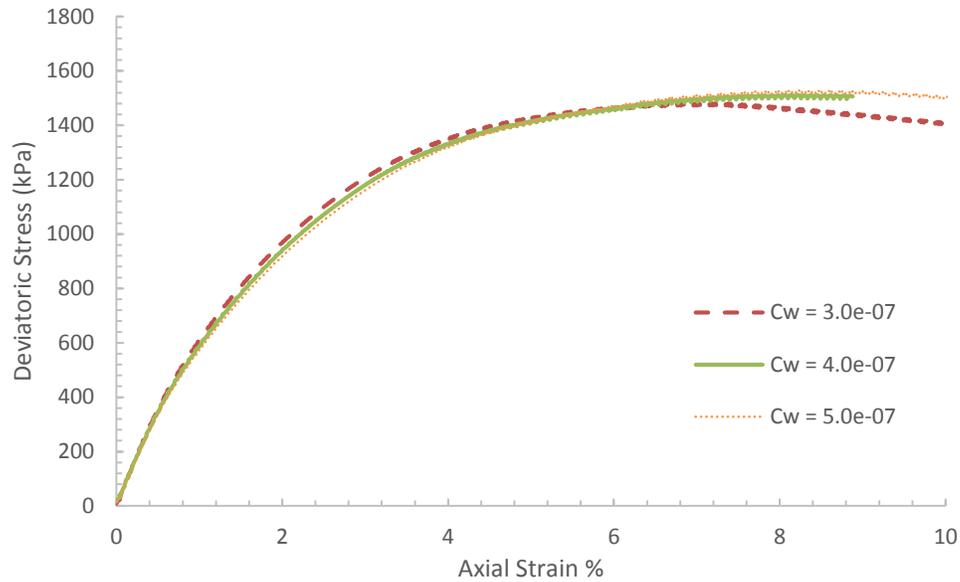
(a)
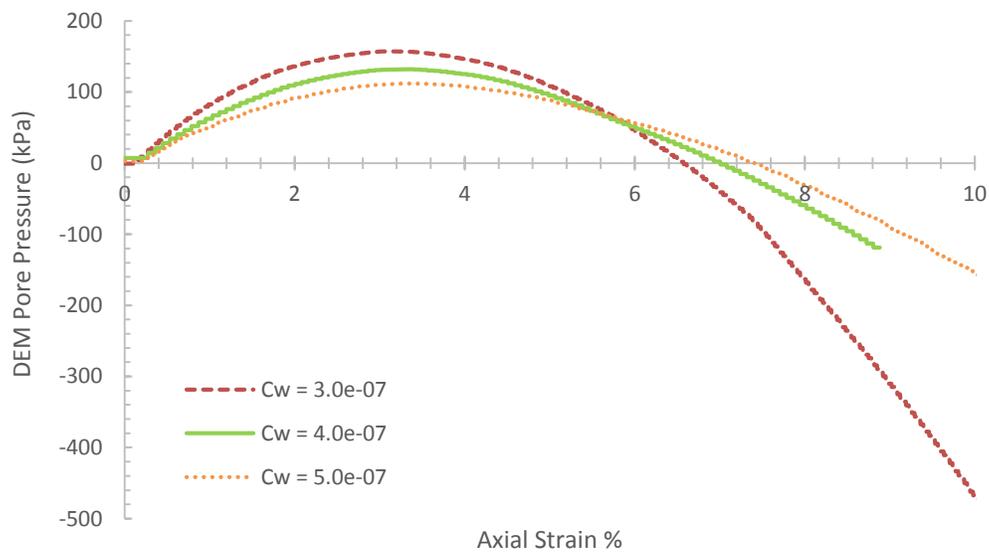
(b)

Figure 5.10: Sensitivity study of compressibility of water in (a) Deviatoric stress – axial strain response; and (b) Pore pressure – axial strain response.

The number of DEM steps during each iteration are varied to investigate the effect on the pore pressure generation behavior. Figure 5.11(a) shows the deviatoric stress to axial strain response when different DEM steps are used during each iteration. It is observed that the peak strength of

the sample is not influenced by the number of DEM steps. However, the sample with 1000 DEM steps behaves a little bit strain softening after the peak stage. From Figure **5.11**(b), pore pressure after peak will drop more rapidly with smaller DEM steps case (1000 DEM steps). The tangential line to the post peak pore pressure curve is observed less change with the increase of the number of DEM steps.

On the other hand, larger DEM steps result in a larger void ratio change, which will lead unsteady calculation of water particle stiffness. Therefore, 2000 DEM steps are chosen for each iteration in all subsequent analyses.

(a)

Deviatoric Stress (kPa) vs Axial Strain

Legend:
— DEM step = 1000
– – DEM Step = 1500
······· DEM Step = 2000
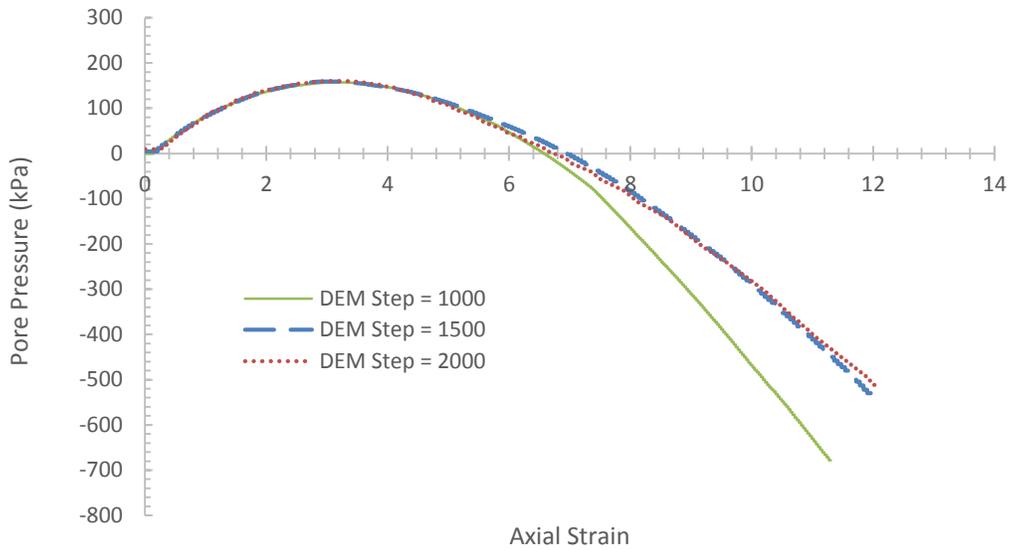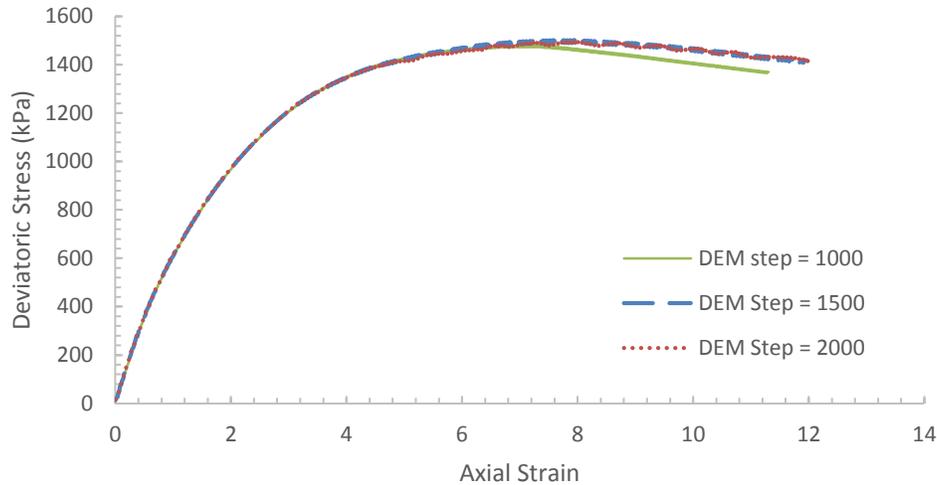
(b)

Figure 5.11: Effect of DEM steps used in each iteration on (a) Deviatoric stress – axial strain response; and (b) Pore pressure – axial strain response.

The comparison between DEM and laboratory results is shown in Figure 5.12. It is observed that DEM calculation is able to capture the peak strength and pore pressure trend. The DEM measured porosity of the whole sample shows a first decrease then increase after the PT point, which indicates the sample is changing from contractive to dilative behavior. The total volumetric strain of sample is observed a 0.1% change, which is consistent with laboratory results and numerical results from past research using constant volume method (Gong, 2008).
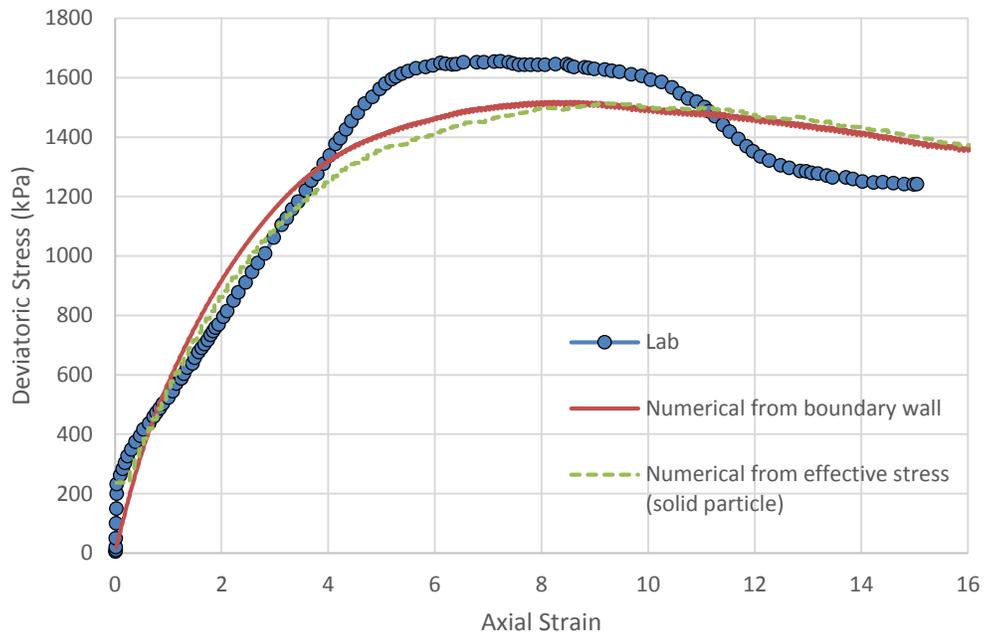
(a)
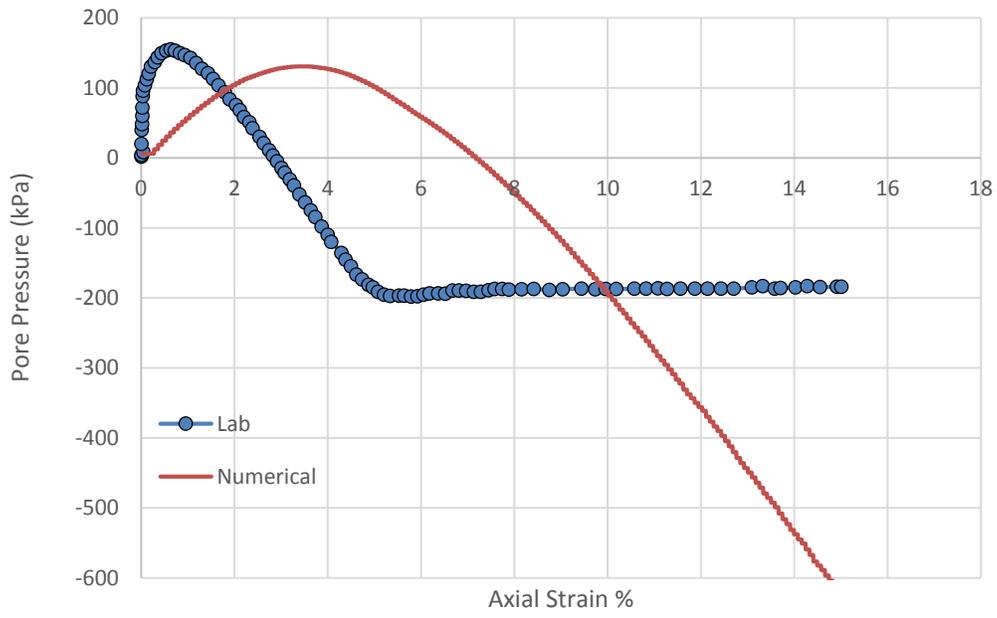
(b)
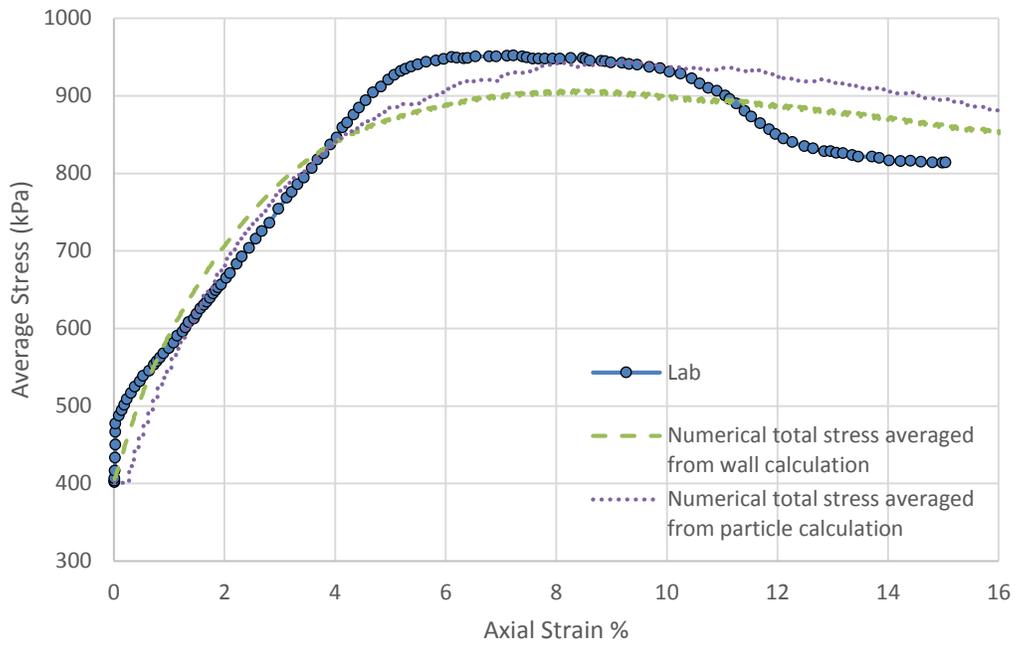
(c)
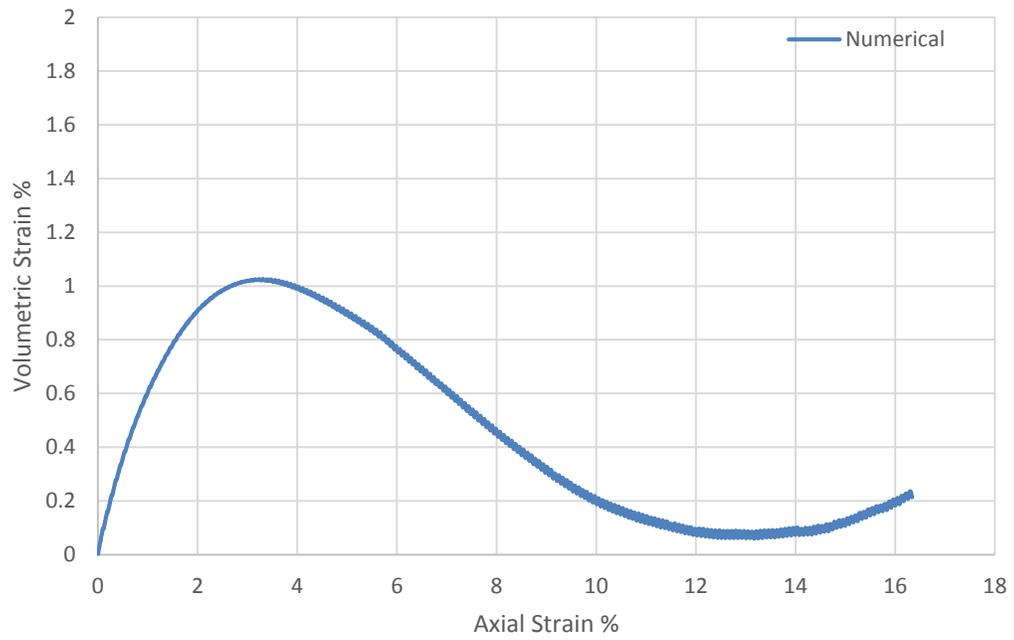
(d)
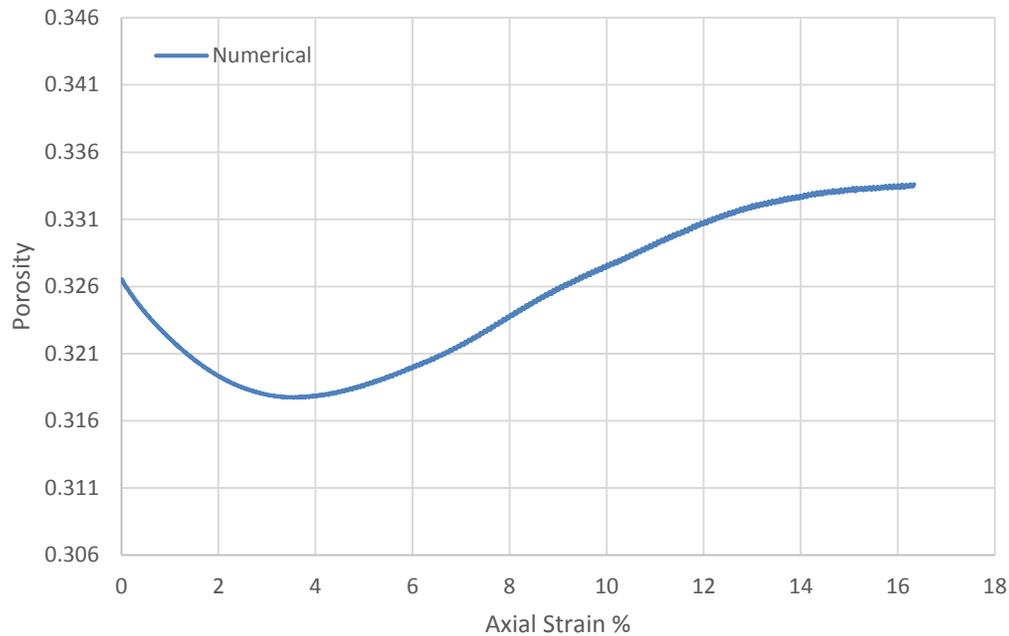
(e)

Figure 5.12: Comparison of DEM and laboratory results (a) Deviatoric stress – axial strain response; (b) Pore pressure – axial strain response; (c) Total averaged stress – axial strain response; (d) Numerical results of volumetric strain of the whole sample respected to axial strain; (e) Numerical results of porosity of the whole sample respected to axial strain.

When pore pressure goes to a negative value, it is observed that the laboratory deviatoric stress – axial strain response is a strain hardening, followed by a little bit strain softening. The corresponding pore pressure reaches the steady state and not change with the increase of axial strain. This might be due to the irregularity of particle shape. However, sphere particle is used in DEM simulation, which can not 100% capture the laboratory response.

The main disagreement between laboratory and DEM results are pore pressure to axial strain response. The DEM calculated pore pressure continue to decrease without reaching any steady state. The main reason for such response is the linear relationship between single force induced by water particle on a contact and the pore pressure of the whole sample no longer exist with the

158

sample of irregular packing particles. In this case, the water particle stiffness needs to be determined using an iterative scheme before used in pore pressure calculation.

The DEM volumetric strain, although calculated small, still exist when compared with constant volume method. Since there are no constraints on volume change in the water element formulation, further research is needed to refine water element to reach a zero volumetric strain.

5.4. Conclusion

In this Chapter, the new method has been presented to model solid-fluid interaction in DEM analysis. The pore pressure build-up due to solid deformation is captured using a DEM water element, which occupies the same position and has the same deformation as the solid element. The water element stiffness (micro) is calculated based on changes in pore space and the compressibility of water (macro). The method is then applied to the 3D DEM numerical simulation of consolidated triaxial undrained compression test on Syncrude sand sample. The micro-properties of sand particles is first calibrated against laboratory consolidated triaxial drained compression test.

Comparison between numerical and laboratory undrained results show that the DEM model is able to capture stress path, pore pressure change, and volume change in a laboratory test.

Chapter 6. Conclusions and Recommendations

This thesis has presented the development of a new numerical technique that couples DEM with continuum fluid using two coupling methods: solid permeability fluid coupling (SPF) and solid deformation pore pressure coupling (SDP). The two coupling methods are applied in sand production and consolidated triaxial undrained problems. This chapter summarizes the key point that can be concluded from this research.

6.1. Summary of the main conclusions for the whole thesis

A sand production model has been presented by SPF coupling method to couple DEM and fluid flow model. The model has been verified with analytical solutions and applied to examine sanding process in synthetic sanding tests. The model accounts for permeability and porosity changes due to solid deformation and sand production.

From the numerical results of sanding test on block sample under different far field stress, a circular breakout was found for the case of isotropic boundary stress with $\sigma_H = \sigma_h = 60$ MPa. The breakout morphology changes to V-shaped breakout with unequal boundary stresses when $\sigma_H = 60$ MPa and $\sigma_h = 30$ MPa. Larger sanding occurs with unequal boundary stresses when $\sigma_H = 60$ MPa and $\sigma_h = 30$ MPa, compared to the case with isotropic boundary stress with $\sigma_H = \sigma_h = 60$ MPa. Sand production occurs from degraded zones where most bond failures have occurred. Sand production from V-shaped breakout changes the wellbore shape from circle to ellipse.

From the results of step-rate sanding test on block sample, the boundary stress plays a major role in sand production through sandstone degradation. However, less sanding occurs at higher boundary effective stress but considerably lower boundary pressure due to the ineffective removal of the degraded materials for weaker seepage forces. For high boundary pressure, seepage force

plays a major role in the sand production as it removes degraded materials, results in stress redistribution which can then contribute to further degradation and sanding. More sand production occurs at lower far-field stress (in this case, 58 MPa) but higher boundary pressure (in this case, 20 MPa).

A new method has been presented to model solid-fluid interaction in DEM analysis by using SDP coupling. The pore pressure build-up due to solid deformation is captured using a DEM water element, which occupies the same position and has the same deformation as the solid element. The water element stiffness (micro) is calculated based on changes in pore space and the compressibility of water (macro). Two examples have been presented to demonstrate the approach and check the accuracy of the algorithm. The comparison between the numerical and analytical results shows that this continuum-discrete model can accurately capture the deformation of water saturated densely packed particles. During the dissipation process, pore pressure changes are simulated by reducing the water particle stiffness calculated from pore volume reduction. The bisection method is used to calculate the correct water particle stiffness for a specified pore pressure in each particle. Analytical solutions based on traditional soil mechanic theory for the oedometer test is used to validate the proposed algorithm. Comparison between numerical and analytical results show that the DEM model not only can replicate saturated loosely packed particles deformation but also can capture densely packed particle deformation accurately.

6.2. Applicability of model and future work

The following comments provide some recommendations for future research and the applicability of the developments presented in in this dissertation.

- The use of discontinuum mechanics in the simulation of sanding poses a serious deficiency as the application of particle method to large scale problems is currently difficult. For instance,

a 2D 1 m^2 geometry with 0.1 mm diameter disk-shaped even-sized particles will generate 100 million particles. The restrictions of DEM in the simulation of large-scale problems can be reduced by blending the continuum and DEM models. In the hybrid approach, the DEM zone will be limited to the small zone around the well where rock degradation occurs. Farther away, deformation is expected to be elastic or in the hardening mode for which a continuum model is adequate.

● The main factors which control the strength of sandstone are particle friction, particle interlocking between grains and the cement content. However, if bonding/cementation between grains is removed, particle friction and interlocking between grains are the main factors keeping the material intact. The effect of grain size on the formation of shear bands and sand production requires further studies. In this case, samples with different grain size distributions are studied by conducting hollow cylinder test. The samples with different grain size distributions need to calibrate to the same uniaxial compressive strength to avoid a possible effect of rock strength on sand production. The amount of produced sand can be calculated for the same confining stress but different particle sizes (fine and course grain).

● The mesh in SPF coupling of sanding model is fixed during the whole calculation process, which is able to capture uniform and V-shape breakout and sand production. However, fracture-like breakout and subsequent sand production could not be captured by current mesh. The mesh size along fracture-like breakout should be the same as the width of fracture. The adaptive mesh is needed in future DEM sand production simulation using SPF coupling method.

● The high pore fluid pressure exists in finer-grained slurries behind a debris flow snout, owing to their low permeability and great compressibility, and produce low pore-pressure diffusivity.

The integration of SDP and SDP coupling method could be further expanded to study the mechanical behavior of debris flow.

Bibliography

[1]   Alvarado, G. (2007). Influence of late cementation on the behavior of reservoir sands. PhD Thesis, University of London (Imperial College of Science, Technology & Medicine), UK.

[2]   ASTM Standard D2435/D2435M-11. (2011). "Standard Test Methods for One-Dimensional Consolidation Properties of Soils using incremental Loading." ASTM International, West Conshohocken, PA, DOI: 10.1520/D2435_D2435M-11, www.astm.org.

[3]   Azadbakht, S., Jafarpour, M., Rahmati, H., Nouri, A., Vaziri, H., Chan, D. (2012). A numerical model for predicting the rate of sand production in injector wells. *Proceeding of SPE Deepwater Drillings and Completions Conference*, Galveston, Texas. SPE 156394.

[4]   Been, K., Jefferies, M. G. (1985). A state parameter for sands. *Geotechnique*, 35(2), 99-112

[5]   Behrmann, L. A., Willson, S. M., de Bree, Ph., and Presles, C. (1997). Field implications from full-scale sand production experiments. *SPE Annual Technical Conference and Exhibition*, San Antonio, Texas.

[6]   Bianco, L. C. B., and Halleck, P. M. (2001). Mechanisms of arch instability and sand production in two-phase saturated poorly consolidated sandstones. *SPE European Formation Damage Conference*, Hague, Netherlands.

[7]   Bishop, A. W., and Eldin, A. K. G. (1950). Undrained triaxial tests on saturated sands and their significance in the general theory of shear strength. *Geotechnique*, 2, 13-32.

[8]   Bishop, A. W., and Eldin, A K. g. (1953). The effect of stress history on the relation between j and porosity of sand. *Proc. 3rd international conference on soil mechanics and foundation engineering*, Zurich, Switzerland, 1, 100-105.

[9]   Bonilla, R. R. O. (2004). Numerical simulations of undrained granular media. Ph.D. Thesis, University of Waterloo, Canada.

[10]   Boutt, D. F., Cook, B. K., McPherson, B., and Williams, J. R. (2007). Direct simulation of fluid-solid mechanics in porous media using the discrete element and lattice-Boltzmann methods. *Journal of Geophysical Research - Solid Earth*, 112(B10), B10209.

[11]   Boutt, D. F., Cook, B. K., and Williams, J. R. (2010). A coupled fluid-solid model for problems in geomechanics: Application to sand production. *International Journal for Numerical and Analytical Methods in Geomechanics*, 35(9), 997-1018.

[12]   Bradford, I. D. R., Cook, J. M. (1994). A semi-analytical elastoplastic model for wellbore stability with applications to sanding. *In. Proc. Eurck*. Rotterdam. 347-351.

[13]   Bratli, R. K., and Risnes, R. (1981). Stability and failure of sand arches, *SPE Journal*, 21, 236-248.

[14]   Chan, D. (1993). Numerical simulation of wet granular flow. *The International Conference on Soft Soil Engineering,* 68 -73.

[15]   Chan, D., and Tipthavonnukul, S. (2008). Numerical Simulation of Granular Particles Movement in Fluid Flow. *International Journal of Nonlinear Sciences and Numerical Simulations*, 9(3), 229-248.

[16]   Chapra, S. C. (2012). Applied Numerical Methods with MATLAB[®] for Engineers and Scientists 3rd Edition; New York, McGraw-Hill: 134-140.

[17]   Cheung, L.Y. G. (2010). Micromechanics of Sand Production in oil wells. Ph.D. Thesis. University of London, United Kingdom.

[18]   Climent, N., Arroyo, M., O'Sullivan, C., and Gens, A., (2014). Sand production simulation coupling DEM with CFD. *European Journal of Environmental and Civil Engineering.* 18(9), 983-1008.

[19]   Coates, G. R., and Denoo, S. A. (1981). Mechanical properties program using borehole analysis and Mohr's circle, *Proceedings of SPWLA 22nd Annual Logging Symposium*, Mexico.

[20]   Cook B. K. (2001). A Numerical Framework for the Direct Simulation of Solid-Fluid Systems. Sc.D. Thesis, Massachusetts Institute of Technology, USA.

[21]   Cook, B. K., Noble, D. R., and Williams, J. R. (2004) A direct simulation method for particle-fluid systems. *Engineering Computations*, 21(2/3/4), 151-168.

[22]   Craig, R. F. (2004). Craig's Soil Mechanics 7th Edition. 2 Park Square, Milton Park, Abingdon, Oxon OXI4 4RN, 91-133.

[23]   Crook, T., Wilson, S., Yu, J. G., and Owen, R. (2003). Computational modeling of the localized deformation associated with borehole breakout in quasi-brittle materials. *Journal of Petroleum Science and Engineering*, 38(3), 177-186.

[24]   Cui, X. (2012). Numerical Simulation of Internal Fluidization and Cavity Evolution due to a Leakage Pipe using the Coupled DEM-LBM Technique. Ph.D. Thesis, University of Birmingham, UK.

[25]   Cui, Y., Nouri, A., Chan, D., and Rahmati, E. (2016). A new approach to DEM simulation of sand production. *Journal of Petroleum Science and Engineering*, 147, 56-67.

[26] Cuss, R. J., Rutter, E. H., and Holloway, R. F. (2003). Experimental observations of the mechanics of borehole failure in porous sandstone. *International Journal of Rock Mechanics & Mining Sciences*, 40, 747-761.

[27] Cundall, P. A. (1971). A computer model for simulating progressive, large-scale movements in blocky rock systems. Proc. Symp. Int. Soc. Rock Mech, Nancy, 2, 132-150.

[28] Cundall, P. A. (1999). Technical Note: The incorporation of fluid coupling into PFC.

[29] Cundall, P. A., and Strack, O. D. L. (1979). A discrete numerical model for granular assemblies. *Géotechnique*, 29(1), 47-65.

[30] Dake, L. P. (1998). Fundamentals of Reservoir Engineering, seventeenth ed. Elsevier, Amsterdam.

[31] Detournay, C. (2008). Numerical modeling of the slit mode of cavity evolution associated with sand production. *SPE Annual Technical Conference*, Colorado, USA.

[32] Edwards, D. P., Sharma, Y., and Charron, A. (1983). Zones of sand production identified by log-derived mechanical properties: a case study. *Proceedings of the 8th European Formation Evaluation (SPWLA '83)*, London, UK.

[33] Evett, J. B., and Liu, C. (1987). Fundamentals of Fluid Mechanics, McGraw-Ho, Inc. New York.

[34] Feng, Y. T., Han, K., Owen, D. R. J. (2007). Coupled lattice Boltzmann method and discrete element modeling of particle transport in turbulent fluid flow: Computational issues. *International Journal for Numerical Methods in Engineering*, 72, 1111-1134.

[35] Feng, Y. Y., Han, K., Owen, D. R. J. (2010). Combined three-dimensional lattice Boltzmann method and discrete element method for modeling fluid-particle interactions with

experimental assessment. *International Journal for Numerical Methods in Engineering*. 80, 299-245.

[36] Fjær, E., Holt, R. M., Horsrud, P., Raaen, A. M., and Risnes, R. (2008) *Petroleum Related Rock Mechanics*. Elsevier, Amsterdam. pp. 344-346.

[37] Gong, G. (2008). DEM simulations of drained and undrained behavior. Ph.D. Thesis, University of Birmingham, UK.

[38] Gong, G., Thornton, C., and Chan, A. H. C. (2012). DEM Simulations of Undrained Triaxial Behavior of Granular Material. *Journal of Engineering Mechanics*, 138(6) 560-566

[39] Goodarzi, M., Kwok, C. Y., and Tham, L. G. (2019). A continuum-discrete model using Dacry's Law: formulation and verification. I*nternational Journal for Numerical and Analytical Methods in Geomechanics*. 29(3), 327-342.

[40] Grof, Z., Cook, J., Lawrence, C. J., and Stepanek, F. (2009). The interaction between small clusters of cohesive particles and laminar flow: Coupled DEM/CFD approach. *Journal of petroleum science and engineering*, 66, 24-32.

[41] Haimson, B .C., and Song, I. (1993). Laboratory study of borehole breakouts in Cordova Cream: a case of shear failure mechanism. *International Journal of Rock Mechanics and Mining Sciences & Geomechanics Abstracts*, 30(7), 1047-1056.

[42] Haimson, B. C., and Klaetsch, A. R. (2002). Porosity-dependent fracture-like breakouts in St. Peter sandstone, *In Mining and Tunneling Innovation and Opportunity, University of Toronto Press,* 1365–1372.

[43] Haimson, B., and Lee, H. (2004). Borehole breakouts and compaction bands in two high-porosity sandstones. *International Journal of Rock Mechanics & Mining Sciences*, 41, 287-301.

[44] Haimson, B. and Chang, C. (2005). Brittle fracture in two crystalline rocks under true triaxial compressive stresses. Petrophysical Properties of Crystalline Rocks. Geological Society of London Special Publication, 240, 47–59.

[45] Haimson, B. (2006). True triaxial stresses and the brittle fracture of rock. *Pure and Applied Geophysics*, 163, 1101–1130.

[46] Haimson, B. (2007). Micromechanisms of borehole instability leading to breakouts in rocks, *International Journal of Rock Mechanics & Mining Sciences*, 44, 157-164.

[47] Han, K., Feng, Y. T., and Owen, D. R. J. (2007). Coupled lattice Boltzmann and discrete element modeling of fluid-particle interaction problems. *Computers and Structures*. 85(11-14), 1080-1088.

[48] Han, Y. (2012). Construction of a LBM-DEM Coupling System and its Applications in Modeling Fluid Particle Interaction in Porous Media Flow. Ph.D. Thesis. University of Minnesota, USA.

[49] Han, Y. (2013). An investigation of pore-scale fluid-solid interaction in a perforation cavity with a coupled DEM/Lattice-Boltzmann model. *Continuum and Distinct Element Numerical Modeling in Geomechanics.* Itasca International Inc, Minneapolis.

[50] Hakuno, M., and Tarumi, Y. (1988). Sand liquefaction analysis by granular assembly simulation. *Proceedings of the Ninth World Conference on Earthquake Engineering,* Tokyo, Japan, 231-236.

[51] Hayatdavoudi, A. (1999). Formation and liquefaction: a mechanism for explaining fines migration and well sanding. *Proceedings of the SPE Mid-Continent Operations Symposium*, Oklahoma City, Oklahoma, USA.

[52] Hou, S., Sterling, J., Chen, S., and Doolen, G. D. (1996). A lattice Boltzmann subgrid model for high Reynolds number flows. Field Institute Communications, 6, 151-166.

[53] Ishihara, K., Tatsuoka, F., Yasua, S. (1975). Undrained deformation and liquefaction of sand under cyclic stresses, *Soil and Foundations*, 15(1), 29-44.

[54] Itasca Consulting Group. (2008). PFC3D version 4.0 Manual. Minneapolis.

[55] Iwan, W. D. (1966). A Distributed-element Method for Hysteresis and Its Steady-state Dynamic Response. *Journal of Applied Mechanics (ASME)*, 33(4), 893-900.

[56] Kafui, K. D., Thornton, C., and Adams, M. J. (2002). Discrete particle continuum fluid modeling of gas-solid fluidized beds. *Chemical Engineering Science*, 57(13), 2395-2410.

[57] Kishino, Y. (1990). Quasi-static simulation of liquefaction phenomena in granular materials. *Proc. of the second international symposium for science on form*, Tokyo: KTK Scientific Publishers, 157-174.

[58] Ladd, A. and Verberg, R. (2001). Lattice-Boltzmann simulations of particle-fluid suspensions. *Journal of Statistical Physics*. 104(5/6), 1191-1251

[59] Latham, J. P., Munjiza, A., Mindel, J., Xiang, J., Guises, R., Garcia, X., Pain, C., Gorman, G., Piggot, M. (2008). Modelling of massive particulates for breakwater engineering using coupled FEMDEM and CFD; *Particuology*, 6, 572-583.

[60]   Lee, M. Y., and Haimson, B. C. (1993). Laboratory study of borehole breakouts in Lac du Bonnet granite: a case of extensile failure mechanism. *International Journal of Rock Mechanics and Mining Sciences & Geomechanics Abstracts*, 30(7), 1039-1045.

[61]   Lee, M. Y., and Haimson, B. C. (1995). Estimating in situ stress conditions from borehole breakouts and core disking-experimental results in granite. *In Proceedings of 8th International Congress on Rock Mechanics*, Tokyo, Balkema Publication, 1, 341–346.

[62]   Lee, M. Y. (2005). Borehole breakouts in Arkosic sandstones and quartz-rich sandstones. Ph.D. Thesis, University of Wisconsin-Madison, USA.

[63]   Li, L., Papamichos, E., Cerasi, P. (2006). Investigation of sand production mechanisms using DEM with fluid flow. *EUROCK 2006 – Multiphysics Coupling and Long Term Behaviour in Rock Mechanics*, Taylor & Francis. 241-247.

[64]   Liu, G., Rong, G., Peng, J., and Zhou, C. (2015). Numerical simulation non undrained triaxial behavior of saturated soil by a fluid coupled-DEM model. *Engineering Geology*. 193, 26-266.

[65]   Lominé, F., Scholtès, L., Sibille, L., and Poullain, P. (2013). Modeling of fluid-solid interaction in granular media with coupled lattice Boltzmann/discrete element methods: application to piping erosion. International Journal for Numerical and Analytical Methods in Geomechanics. 37, 577-596.

[66]   Mastin, L. G. (1984). Development of borehole breakouts in sandstone. MSc Thesis, Stanford University, USA.

[67]   McNamara, G. R. and Zanetti, G. (1988). Use of the Boltzmann equation to simulate lattice-gas automata. *Physical Review Letters*. 61, 2332-2335.

[68] Mori, H., Ogawa, Y., Cao, G. (2002). Liquefaction Analysis of River Dike with Discrete Element Method. *Proceedings of the Third International Conference on Discrete Element Method*, Santa Fe, New Mexico, 23-25.

[69] Mori, H., Ogawa, Y., and Cao, G. (2002). Liquefaction Analysis of River Dike with Discrete Element Method. *Discrete Element Methods*, 172-177.

[70] Mori, H., Ogawa, Y., Cao, G. (2002). Liquefaction Analysis of River Dike with Discrete Element Method. *Proceedings of the 3rd International Conference on Discrete Element Method*, Santa Fe, New Mexico, 23-25.

[71] Nakasa, H., Takeda, T., Ishikawa, H. (1999). A liquefaction analysis aim to investigation of behavior of to the ground surrounding the nuclear power plant during or after strong earth quakes (A simulation study on Liquefaction using DEM). *7th International Conference on Nuclear Engineering*, Tokyo, Japan.

[72] Newland, P. L., and Alley, B. H. (1959). Volume change during undrained triaxial tests on saturated dilatant granular materials. *Geotechnique*, 9(4), 174-182.

[73] Ng, T. T., and Dobry, R. (1994). Numerical simulations of monotonic and cyclic loading of granular soil. *Journal of Geotechnical Engineering,* ASCE, 120(2), 388-403

[74] Noble, D., and Torczynski, J. (1998). A lattice Boltzmann method for partially saturated cells. *International Journal of Modern Physics C*. 9, 1189-1201.

[75] Nouri, A., Vaziri, H., Kuru, E., and Islam, R. (2006). A comparison of two sanding criteria in physical and numerical modeling of sand production. *Journal of petroleum science and engineering*, 50, 55-70.

[76] O'Sullivan, C. (2011). Particulate Discrete Element Modelling: A Geomechanics Perspective, Spon Press (an imprint of Taylor & Francis), London.

[77] Pain, C. C., Umpleby, A. P., Oliveria, C. R. C. de., Goddard, A. J. H. (2001). Tetrahedral mesh optimization and adaptively for steady-state and transient finite element calculation, *Computer Methods in Applied Mechanics and Engineering*, 190, 3771-3796.

[78] Pain, C. C., Piggott, M. D., Goddard, A. J. H, Fang, F., Gorman, G. J., Marshall, M. D. E., Power, P. W., Oliveria, C. R. C. de. (2005). Three-dimensional unstructured mesh ocean modelling, *Ocean Modelling*, 10, 5-33.

[79] Papamichos, E., Malmanger, E. M. (2001). A sand erosion model for volumetric sand predictions in a North Sea reservoir. *SPE Reservoir Evaluation and Engineering*, 44-50.

[80] Papamichos, E., Vardoulakis, I. (2005). Sand erosion with a porosity diffusion law. *Computers and Geotechnics*, 32, 47-58.

[81] Potyondy, D. O., Cundall, P. A. (2004). A bonded-particle model for rock. *International Journal of Rock Mechanics & Mining Sciences*, 41(8), 1329-1364.

[82] Preece, D. S., Jensen, R. P., Perkins, E. D., Williams, J. R. (1999). Sand production modeling using superquadric discrete element and coupling of fluid flow and particle motion. Rock Mechanics for Industry, Balkema, Rotterdam. 161-167.

[83] Quadros, R., Vargas, E. A., Goncalves, C. J., and Prestes, A. (2010). Analysis of sand production processes at the pore scale using the discrete element method and lattice Boltzmann procedures. *Proceedings of the 44th US Rock Mechanics Symposium and 5th U.S. – Canada Rock Mechanics Symposium*. Salt Lake City, UT. USA.

[84] Rahmati, H. 2013. Micromechanical Study of Borehole Breakout Mechanism. Ph.D. Thesis. University of Alberta, Canada.

[85] Rahamti, H., Nouri, A**.**, Chan, D., Vaziri, H., (2013a). Simulation of Drilling-Induced Compaction Bands Using Discrete Element Method, *Int. J. Numer. Anal. Met*. 38(1), 37-50.

[86] Rahmati, H., Nouri, A., Chan, D., Xiao, Y., (2013b). Systematic Calibration Procedure for DEM Parallel-bond Models, *Canadian Energy Technology & Innovation.* 1(4).

[87] Rahmati, H., Jafarpour, M., Azadbakht, S., Nouri, A., Vaziri, H., Chan, D., Xiao, Y., (2013c). Review of Sand production Prediction Models. *J. Petrol. Eng.* 2013, 1-16.

[88] Risnes, R., Bratli, R. K., and Horsrud, P. (1982). Sand stresses around a wellbore. *Society of Petroleum Engineers Journal,* 22(6), 883-898.

[89] Sakai, M. (2016). How Should the Discrete Element Method Be Applied in Industrial System? A Review. *KONA Powder and Particle Journal*, 33, 169-178.

[90] Saucier, R. J. (1974). Consideration in Gravel Pack Design, *J. Petrol. Technol.* 23(2), 205-212.

[91] Schanz T., Vermeer P.A., Bonnier P.G. (1999). The hardening soil model: formulation and verification. Beyond 2000 in computational geotechnique – 10 Years of PLAXIS. Balkema, Rotterdam.

[92] Shen, B., Stephansson, O., and Rinne, M. (2002). Simulation of borehole breakouts using FRACOD2D, *Oil & Gas Science and Technology Journal*, 57(5), 579-590.

[93] Sitharam, T. G., Dinesh, S. V., and Shimizu, N. (2002). Micromechanical modelling of monotonic drained and undrained shear behavior of granular media using three-dimensional

DEM. *International Journal for Numerical and Analytical Methods in Geomechanics*, 26(12), 1167-1189.

[94]   Sun, Y., and Vinogradov, P. (1998). Numerical simulation of jamming of solid particles transported by fluid in planer channels. *Computer Modeling & Simulation in Engineering*, 3, 27-32

[95]   Thornton, C., and Barnes, D. J. (1986). Computer simulated deformation of compact granular assemblies. *Acta Mechanica*, 64(1), 45-61.

[96]   Tipthavonnukul, S. (2002). Numerical Simulation of Granular Particle Movement in Fluid Flow. Ph.D. Thesis. University of Alberta, Canada.

[97]   Tortike, W. S. (1991). Numerical simulation of thermal multiphase fluid flow in an elastoplastic deforming oil reservoir. (PhD Thesis). University of Alberta, Canada.

[98]   Tronvoll, J., and Fjaer, E. (1994). Experimental study of sand production from perforation cavities. *International Journal of Rock Mechanics and Mining Sciences & Geomechanics Abstracts*, 31(5), 393-410.

[99]   Tronvoll, J., Papamichos, E., Skjarstein, A., and Sanfilippo, F. (1997). Sand production in ultra-weak sandstones: is sand control absolutely necessary? *Proceedings of the 5th Latin American and Caribbean SPE Conference and Exhibition*, Rio de Janeiro, Brazil.

[100]   Tsuju, Y., Kawaguchi, T, and Tanaka, T. (1993). Discrete particle simulation of two-dimensional fluidized bed. *Powder Technology, 77*, 79-87

[101]   Vaid, Y. P., Chung, E. K. F., Kuerbis, R. H. (1990). Stress path and steady state. *Canadian Geotechnical Journal*, 27, 1-7.

[102] Vaid, Y. P., Sivathayalan, S., Eliadorani, A., and Uthayakumar, M. (1996). CANLEX Laboratory testing at U.B.C. Report.

[103] Van den Hoek, P. J., Hertogh, G. M. M., Kooijman, A. P., Bree, Ph. De., Kenter, C. J., Papamichos, E., (2000). A New Concept of Sand Production Prediction: Theory and Laboratory Experiments. *SPE. Drill. Completion.* 15(4), 261-273.

[104] Vire, A., Xinag, J., Mithaler, F., Farrell, P. E., Piggott, M. D., Latham, J. P., Pavlidis, D., Pain, C. C. (2012). Modelling of fluid-solid interactions using an adaptive mesh fluid model coupled with a combined finite-discrete element model. *Ocean Dynamics*, 62(10), 1487-1501.

[105] Zhang, L. (2003). The behavior of granular material in pure shear, direct shear and simple shear. Ph.D. Thesis, Aston University, UK.

[106] Zhao, J. D., Shan, T. (2013). Coupled CFD-DEM simulation of fluid-particle interaction in geomechanics. *Powder Technology*, 239, 248-258.

[107] Zhao, T. (2014). Investigation of Landslide-Induced Debris Flows by the DEM and CFD. PhD Thesis, University of Oxford, UK.

[108] Zhu, H. P., Zhou, Z. Y., Yang, R. Y., and Yu, A. B. (2007). Discrete particle simulation of particulate systems: Theoretical developments. *Chemical Engineering Science*, 62, 3378-339.

[109] Zhu, H. P., Zhou, Z. Y., Yang, R. Y., Yu, A. B. (2008). Discrete particle simulation of particulate systems: a review of major applications and findings, *Chemical Engineering Science*, 63, 5728-5770.

Appendix A: The Finite Difference Approximation to Fluid flow Equations

The finite-difference method is implemented by superimposing a finite-difference grid over the reservoir to be modelled. The chosen grid system is then used to approximate the spatial derivatives in the continuous equations. These approximations are obtained by truncating the Taylor series expansion of the unknown variables (pressure for single-phase-flow problems) in the equations. A similar procedure is used in the time domain.

From Equation 3.10., the equation contain a second derivative of pressure with respect to space and a first derivative of pressure with respect of time. The second derivative in the flow equations generally approximated by the central-difference approximation because of the higher-order nature of the approximation. The first derivative is generally approximated by the forward-difference approximation. These choices are dictated by the stability of the final system of equations.

Combine Equation 3.7. and Equation 3.8., by considering only in radial direction, the partial-differential equation for single-phase flow through rack in r direction is expressed as follows:

$$-\frac{\partial}{\partial r}\left(-\frac{k}{\mu}\frac{\partial P}{\partial r}\rho\right) = \frac{\partial}{\partial t}(\phi\rho) = \rho\frac{\partial \phi}{\partial t} + \phi\frac{\partial \rho}{\partial t} \qquad \text{[A.1]}$$

where k is the rock permeability, μ is the fluid viscosity, ϕ is the porosity of rock, ρ is the density of fluid, and t is time. Assume ρ and μ are constants, with the combination of compressibility of fluid from Equation 3.9., Equation A.1 reduce to

$$\frac{1}{\mu}\frac{\partial}{\partial r}\left(k\frac{\partial P}{\partial r}\right) = \frac{\partial \phi}{\partial t} + \phi C_f\frac{\partial P}{\partial t} \qquad \text{[A.2]}$$

$$\frac{\partial k}{\partial r}\frac{\partial P}{\partial r} + k\frac{\partial^2 P}{\partial r^2} = \mu\frac{\partial \phi}{\partial t} + \mu\phi C_f\frac{\partial p}{\partial t}$$

where $\frac{\partial \phi}{\partial t}$ is updated by DEM calculation. The finite difference approximation of the spatial and time derivative from Equation A.2 are shown as follows:

$$\frac{\partial k}{\partial r} = \frac{k_{i+1} - k_i}{\Delta r}$$

$$\frac{\partial P}{\partial r} = \frac{P_{i+1}^{n+1} - P_i^{n+1}}{\Delta r}$$

$$\frac{\partial^2 P}{\partial r^2} = \frac{P_{i+1}^{n+1} - 2P_i^{n+1} - P_{i-1}^{n+1}}{\Delta r^2}$$

$$\frac{\partial P}{\partial t} = \frac{P_i^{n+1} - P_i^n}{\Delta t}$$

[A.3]

where i represent position of grid point, t present time step of calculation, and Δr is the distance between two grid point, and Δt present each time increment.

In finite difference equations, the term P^n presents the pressure values of the grid point at the known time level. The stepwise procedure for advancing the simulation in times begins by assigning known pressure values to the n time level in the finite difference equations. The equations can then be solved for the unknown pressure, P^{n+1}. Once determined, the values of P^{n+1} are used as the known pressure for the next time step. The specified pressure boundary condition $P = P_i$ and $P = P_o$, from **Error! Reference source not found.** are used for inner and outer boundaries along radial direction of reservoir. Substituting Equations A.3 into Equations A.2 results in

$$\left(\frac{k_{i+1}}{\Delta r^2}\right) P_{i+1}^{n+1} - \left(\frac{k_{i+1} + k_i}{\Delta r^2} + \frac{\mu \phi C_f}{\Delta t}\right) P_i^{n+1} + \left(\frac{k_i}{\Delta r^2}\right) P_{i-1}^{n+1} = \mu \frac{\partial \phi}{\partial t} - \frac{\mu \phi C_f}{\Delta t} P_i^n$$

[A.4]

$$A P_{i+1}^{n+1} + B P_i^{n+1} + C P_{i-1}^{n+1} = D P_i^n$$

From above equation we find that three unknowns in the time step of $n+1$, which will be solved by one unknown on the time step of n. Consequently, we must solve Equation A.4 written for all grid blocks and unknowns simultaneously. By applying above equation to all grid point along radial direction, the pressure in next time increment will be solved by the solution of linear matrix equations. The same method can be applied in tangential and vertical direction of the model, the no flow boundary condition is applied in top and bottom platens with $\frac{\partial P}{\partial z} = 0$.